Investigation of an Inhomogeneous Mixing Model for Conditional Moment Closure Applied to Autoignition

by

Adrian Milford

A thesis
presented to the University of Waterloo
in fulfillment of the
thesis requirement for the degree of
Master of Applied Science
in
Mechanical Engineering

Waterloo, Ontario, Canada, 2010

I hereby declare that I am the sole author of this thesis. This is a true copy of the thesis, including any required final revisions, as accepted by my examiners.

I understand that my thesis may be made electronically available to the public.

Abstract

Autoignition of high pressure methane jets at engine relveant conditions within a shock tube is investigated using Conditional Moment Closure (CMC). The impact of two commonly used approximations applied in previous work is examined, the assumption of homogeneous turbulence in the closure of the micro-mixing term and the assumption of negligible radial variation of terms within the CMC equations. In the present work two formulations of an inhomogeneous mixing model are implemented, both utilizing the β-PDF, but differing in the respective conditional velocity closure that is applied. The common linear model for conditional velocity is considered, in addition to the gradient diffusion model. The validity of cross-stream averaging the CMC equations is examined by comparing results from two-dimensional (axial and radial) solution of the CMC equations with cross-stream averaged results.

The CMC equations are presented and all terms requiring closure are discussed. Solution of the CMC equations is decoupled from the flow field solution using the frozen mixing assumption. Detailed chemical kinetics are implemented. The CMC equations are discretized using finite differences and solved using a fractional step method. To maintain consistency between the mixing model and the mixture fraction variance equation, the scalar dissipation rate from both implementations of the inhomogeneous model are scaled. The autoignition results for five air temperatures are compared with results obtained using homogeneous mixing models and experimental data.

The gradient diffusion conditional velocity model is shown to produce diverging behaviour in low probability regions. The corresponding profiles of conditional scalar dissipation rate are negatively impacted with the use of the gradient model, as unphysical behaviour at lean mixtures within the core of the fuel jet is observed. The predictions of ignition delay and location from the Inhomogeneous-Linear model are very close to the homogeneous mixing model results. The Inhomogeneous-Gradient model yields longer ignition delays and ignition locations further downstream. This is influenced by the higher scalar dissipation rates at lean mixtures resulting from the divergent behaviour of the gradient conditional velocity model. The ignition delays obtained by solving the CMC equations in two dimensions are in excellent agreement with the cross-stream averaged values, but the ignition locations are predicted closer to the injector.

Acknowledgements

I would like to thank my supervisor, Professor Cécile Devaud, for outlining my research topic and providing continual guidance and assistance. My knowledge of combustion and programming has grown immensely with her support. I would also like to thank my friends and colleagues Ahmad El Sayed, Andrew Buckrell, and Paul Ziade for their assistance and advice through the course of my research. I also extend my thanks to Professor Gordon Stubley and Professor Xianguo Li for reviewing my thesis, as well as Professor Fue-Sang Lien for his support regarding my MASc seminar.

The financial support from the National Sciences and Engineering Research Council of Canada (NSERC) is gratefully acknowledged.

Contents

List of Tables

List of Figures

Nomenclature

Roman Symbols

$\dot{q}_{rad}$	Heat transfer due to radiation
A_o	Frequency factor
c_p	Specific heat capacity at constant pressure
D_t	Turbulent diffusivity
h	Enthalpy
k	Turbulent kinetic energy
$k(T)$	Reaction rate constant
L	Turbulent length scale
p	Pressure, probability
$P(\eta)$	Probability density function
Q_α	Conditional species mass fraction of species α
Q_h	Conditional enthalpy
Q_T	Conditional temperature
r	Radial coordinate
s	Stoichiometric oxygen to fuel mass ratio

T Temperature

t Time

T_a Activation temperature

t_d Ignition delay

u Velocity

x Axial coordinate

Z Penetration length

Z_k^* Normalized ignition location

Greek Symbols

α Species within the mixture

β Beta function, temperature exponent

χ Scalar dissipation rate

Δr Radial grid spacing

Δx Axial grid spacing

δ_{ij} Kronecker's delta

$\dot{\omega}$ Chemical source term

η Mixture fraction sample space variable

Γ Gamma function

λ Thermal conductivity

μ Dynamic viscosity

ν Kinematic viscosity

ϕ Conserved scalar

ρ Density

τ_c Chemical time scale

τ_t Mixing time scale

ε Turbulent eddy dissipation

ξ Mixture fraction

ξ''^2 Mixture fraction variance

Non-dimensional Numbers

D_a Damköhler number

Sc_t Turbulent Schmidt number

Subscripts

1 Originating from fuel stream

2 Originating from oxidizer stream

air Shock tube chamber property prior to injection

ign Ignition value

ox Oxidizer

pr Products

$stoich$ Stoichiometric value

Other Notation

$\langle \psi \mid \eta \rangle$ Conditional average of ψ

$\langle \psi \rangle$ Unconditional average of ψ

$\overline{\psi}$ Reynolds average of ψ

ψ' Fluctuation about unconditional average

ψ'' Fluctuation about conditional average

$\widetilde{\psi}$ Favre (density-weighted) average of ψ

$\{\psi\}_{R+}$ Cross-stream average of ψ

Acronyms

ADI Alternating Direction Implicit

AMC Amplitude Mapping Closure

CDF Cumulative Distribution Function

CFD Computational Fluid Dynamics

CMC Conditional Moment Closure

CSE Conditional Source-term Estimation

DNS Direct Numerical Simulation

EBU Eddy Break Up

LES Large Eddy Simulation

ODE Ordinary Differential Equation

PDE Partial Differential Equation

PDF Probability Density Function

RANS Reynolds Averaged Navier Stokes

Chapter 1

Introduction

1.1 Overview

Turbulent combustion performs a vital role in many engineering applications including transportation, energy generation, and industrial processes. In 2008 the combustion of fossil fuels accounted for approximately 84% of the energy used in the United States [1]. Emissions of smog-forming pollutants, particulate matter, and greenhouse gases are of growing concern, and strict environmental regulations are being introduced to motivate the design of increasingly efficient combustion devices. The subsequent demand for low cost and low emission fuels has fostered interest in use of natural gas, as it offers the benefits of lower emissions compared to more common fuels and widespread availability.

Transportation accounts for 25% of greenhouse gas (GHG) emissions in Canada [2]. Emissions in this sector have increased 37%, including a 94% increase in GHG emissions from heavy-duty diesel engines, from 1990 to 2007 [3]. Diesel engines, which use the heat of compression rather than a spark plug to ignite the mixture of fuel and air, accounted for over 28% of the total emissions nitrogen oxides (NOx) across Canada in 2007 [3]. Unlike spark-ignition engines, ignition within compression-ignition engines occurs before the fuel and oxidizer are fully mixed [4]. Once autoignition occurs combustion proceeds as the fuel and oxidizer continue to mix. Thus, the interactions of chemistry and turbulent mixing, along with the essential process of autoignition, play an enormous role in the overall efficiency and formation of pollutants in these devices.

The development of computational models to aid in the design of increasingly efficient

combustion devices requires accurate representation of the complex interactions between chemistry and turbulence. In the operation of compression-ignition engines the process of autoignition, in which the fuel and oxidizer react in a self-heating fashion, is extremely important, and accurate prediction of this phenomenon is paramount for successful application of turbulent combustion models in these devices. Modelling of the autoignition process requires a good understanding of the turbulent mixing of fuel and oxidizer, as well as rigorous consideration of the complex non-linear chemical kinetics of the fuel. However, a suitable balance of complexity and computational expense must be achieved for successful widespread implementation of a turbulent combustion model in practical applications.

1.2 Objectives

In earlier work the autoignition behaviour of high pressure methane jets at engine relevant conditions in a shock tube was investigated using the turbulent combustion model Conditional Moment Closure (CMC). Commonly used approximations were applied in this work, such as assuming homogeneous turbulence in the closure of the micro-mixing term within the CMC equations, and solving a radially-averaged form of the CMC equations based on the assumption of negligible radial variation of CMC terms. The autoignition predictions were in reasonable agreement with experimental data, but some discrepancies at the highest and lowest air temperatures were noted. For the engine relevant conditions being examined the assumptions of homogeneous turbulence and negligible radial dependence of the CMC equations could have a significant impact on the predictions of autoignition. Thus, the objectives of this study are:

1. The derivation and implementation of a mixing model that is based upon inhomogeneous turbulence. Two formulations of this model, resulting from the use of two different closures for the conditional velocity term, are examined. In the early stages of mixing between a high pressure fuel jet and air the conditions are far from homogeneous, and the consideration of inhomogeneous turbulence is expected to improve the accuracy of the predictions. In contrast to other CMC studies in which an inhomogeneous formulation of the turbulent mixing model has been applied, this study examines autoignition processes in transient conditions.

2. The derivation and implementation of two-dimensional (axial and radial) solution of the CMC equations. Cross-stream averaging of the CMC equations was shown to be valid for self-similar shear flows. In the current study the methane fuel jet is developing, and thus self-similarity everywhere within jet would not be achieved.

3. Comparison of the predictions of ignition delay and location with experimental data and overall assessment of the effect of the assumptions of homogeneous turbulence and negligible radial variation within the CMC equations on the predictions of autoignition in CMC.

1.3 Outline

In Chapter 2 the shock tube experiments of methane autoignition, which serve as the basis for the autoignition problem examined in this thesis, are described. The relevant governing equations of the flow field and turbulence models are discussed. Concepts important to the modelling of turbulent reacting flows, along with some examples of commonly used turbulent combustion models, are presented.

The turbulent combustion modelling approach applied in this study, CMC, is discussed in Chapter 3. The transport equations of conditional species mass fractions and enthalpy are summarized, and the terms requiring closure are discussed. The relevant closures used in this study are introduced. Previous studies that have investigated autoignition behaviour using CMC methods are outlined.

The inhomogeneous turbulence-based mixing models utilized within the CMC calculations, which form the focus of this study, are outlined in Chapter 4. These models provide closure for an important term in the CMC equations. The two models used for closure of the conditional velocity term within the inhomogeneous mixing model are described, along with homogeneous turbulence-based models utilized in previous work.

Chapter 5 describes the computational method used in this study. The overall solution methodology is summarized, and details are provided on the flow field simulations and corresponding solution of the CMC equations. The assumptions and simplifications of this study are discussed.

The performance of the two formulations of the inhomogeneous mixing model are assessed in Chapter 6. Further, the behaviour of the two conditional velocity models used

within the inhomogeneous model is examined. The predictions of ignition delay and location are compared with results using homogeneous mixing models and with experimental data.

The use of cross-stream averaging in solving the CMC equations is examined in Chapter 7, as ignition delay and location obtained in a preliminary two-dimensional solution of the CMC equations are compared with previous results. The overall solution methodology is outlined. Further, a two-dimensional temperature field obtained through integration of previous cross-stream averaged temperature results is examined.

The findings of this study are summarized in Chapter 8 and conclusions are stated.

Chapter 2

Background

In this chapter background information is presented on the autoignition problem that is examined in this study. The experiments of Wu [5], which provide the basis of this study, are outlined. The relevant governing equations are presented along with a brief description of common turbulence models. Simulation of turbulent reacting flows is a very complex problem, and thus multiple modelling approaches have been suggested. Concepts that are important to non-premixed combustion are discussed, and a selection of common turbulent combustion models are summarized.

2.1 Experiments

The shock tube autoignition experiments of Wu [5] provide the physical conditions for the CMC simulations of methane autoignition in this study. The experiments were designed to simulate engine-relevant temperature and pressure conditions without the complicating effects of complex geometry, external ignition sources, multiple fuel jets and unsteady cylinder temperature and pressure. Thus, these simplifications make them suitable for comparison with numerical work to study the autoignition behaviour of methane in engine-relevant conditions.

The autoignition behaviour of pure methane and various methane fuel blends was investigated. In the present study, the measurements related to only pure methane are

considered. The shock tube has a circular cross-section with an inner diameter of 0.58 m. Its total length is 7.90 m, the driver and driven sections being 3.11 m and 4.79 m long, respectively. An electronically controlled injector was used to inject the gaseous fuel into the preheated and compressed air within the shock tube. A schematic of the experimental setup is presented in Figure 2.1. The reflected shock technique was applied to preheat and compress air into engine-relevant conditions just prior to injection of gaseous fuel. Post-reflected shock pressure and temperature conditions were achieved before combustion started. The temperature and pressure immediately behind the reflected shock were determined by perfect gas behaviour. The uncertainty in the temperature and pressure was found to be 1-2% and 3-4%, respectively. An injector with one central hole of 0.275 mm diameter was used to deliver the fuel at an injection pressure of 120 bar along the centreline of the shock tube with an injection time of 1 ms. To provide optical access to the experimental area, a stainless steel section equipped with three windows was attached to the end of the driven section. A high-speed digital camera (31,000 frames per second) was used to capture the location of the initial ignition kernel. The location of the ignition kernel was identified by the appearance of a non-contiguous flame region that is able to develop into a fully fledged jet flame. The corresponding ignition delay was defined as the time elapsed from the start of the injection of the fuel to the appearance of the ignition kernel. The experimental error was evaluated to be approximately between 0.073 ms and 0.106 ms for ignition delays and 2% for the normalized ignition location. The shock tube test section was maintained at a pressure of approximately 30 bar, while the air temperature was varied between approximately 1200 and 1400 K in increments of approximately 50 K. The number of measurements in each data set, along with the corresponding average temperatures used in the present CMC calculations, are given in Table 2.1.

Table 2.1: Experimental data groups

Number of data points	Average Air Temperature (K)
4	1385
4	1337
20	1294
4	1238
5	1186

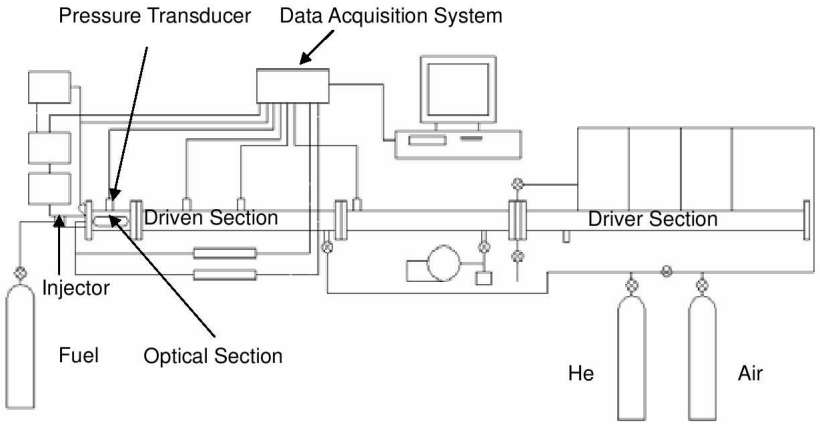

Figure 2.1: Schematic of experimental shock tube set up. Reproduced from Wu [5].

2.2 Governing Equations

2.2.1 Navier Stokes Equations

The Navier Stokes equations are the set of governing equations of fluid mechanics. This equation set includes the continuity equation, the conservation of linear momentum, and the conservation of scalar quantities. The continuity equation requires mass to be conserved, and is given by

$$\frac{\partial \rho}{\partial t} + \frac{\partial (\rho u_i)}{\partial x_i} = 0. \tag{2.1}$$

The conservation of linear momentum is given by

$$\frac{\partial (\rho u_i)}{\partial t} + \frac{\partial (\rho u_i u_j)}{\partial x_j} = -\frac{\partial p}{\partial x_i} + \frac{\partial \tau_{ij}}{\partial x_j} + B_i, \tag{2.2}$$

in which p is the static pressure, B_i represents body forces such as gravity, and τ_{ij} is the symmetric stress tensor, which is defined as

$$\tau_{ij} = \mu \left(\frac{\partial u_i}{\partial x_j} + \frac{\partial u_j}{\partial x_i} \right) - \mu \frac{2}{3} \delta_{ij} \frac{\partial u_k}{\partial x_k}, \tag{2.3}$$

where δ_{ij} is Kronecker's delta. For scalar quantities, such as species concentration, the transport equation is of the form

$$\frac{\partial(\rho\phi)}{\partial t} + \frac{\partial(\rho u_i \phi)}{\partial x_i} = \frac{\partial}{\partial x_i}\left(\rho D_\phi \frac{\partial \phi}{\partial x_i}\right) + \dot{\omega}, \tag{2.4}$$

in which D_ϕ is the diffusivity and $\dot{\omega}$ is the source term of the scalar ϕ. For scalar quantities that are conserved the source term is equal to zero. For species concentrations, Y_α, the transport equation is expressed as

$$\frac{\partial(\rho Y_\alpha)}{\partial t} + \frac{\partial(\rho u_i Y_\alpha)}{\partial x_i} = \frac{\partial}{\partial x_i}\left(\rho D_\alpha \frac{\partial \phi}{\partial x_i}\right) + \dot{\omega_\alpha} \qquad \alpha = 1, 2, \cdots, N_\alpha. \tag{2.5}$$

where N_α denotes the total number of species considered and $\dot{\omega_\alpha}$ is the source term that accounts for changes in species concentration due to chemical reactions.

2.2.2 Enthalpy

In a multicomponent flow the enthalpy is equal to the mass-weighted sum of the specific enthalpies of species α

$$h = \sum_{\alpha=1}^{N_\alpha} Y_\alpha h_\alpha. \tag{2.6}$$

For an ideal gas, the conditional enthalpy of each species can be calculated from the temperature through the expression

$$h_\alpha = h_{\alpha,ref} + \int_{T_{ref}}^{T} c_{p,\alpha}(T) dT, \tag{2.7}$$

where $c_{p,\alpha}$ is the specific heat capacity of species α at constant pressure. In Equation 2.6 $h_{\alpha,ref}$ is a reference enthalpy that accounts for chemical bond energy within compounds, while the second term on the right side represents the sensible enthalpy due to temperature. The specific heat capacity of the mixture is given by a mass-weighed sum of the specific heat capacities of the individual species.

$$c_p = \sum_{\alpha=1}^{N_\alpha} Y_\alpha c_{p,\alpha}. \tag{2.8}$$

The enthalpy transport equation, with work performed by body forces neglected, is given by

$$\frac{\partial(\rho h)}{\partial t} + \frac{\partial(\rho u_i h)}{\partial x_i} = \frac{\partial p}{\partial t} + \frac{\partial(u_i p)}{\partial x_i} + \frac{\partial(u_i \tau_{ij})}{\partial x_i} - \frac{\partial}{\partial x_i} j_q + \dot{q}_{rad}. \tag{2.9}$$

The first term on the right hand side of Equation 2.9 is the local rate of change of pressure, the second term represents the pressure work, and the third term is frictional heating. The term $\dot{q}_{rad}$ represents heat transfer due to radiation, and j_q is the diffusive heat flux, given by the expression

$$j_q = -\lambda \frac{\partial T}{\partial x_i} + \sum_{\alpha=1}^{N_\alpha} h_\alpha j_\alpha. \tag{2.10}$$

In Equation 2.10 λ is the thermal conductivity and j_α is the diffusive species flux represented as

$$j_\alpha = -\rho D_\alpha \frac{\partial Y_\alpha}{\partial x_i}. \tag{2.11}$$

2.3 Averaging Techniques

The governing equations presented in Section 2.2 involve instantaneous values for quantities of interest, such as velocity, pressure, and concentrations. In a turbulent flow there are significant fluctuations in these values, over a range of length and time scales. The instantaneous quantities can be decomposed into an average and a fluctuation, which provides a modified form of the governing equations. Reynolds averaging is commonly used in non-reacting flows, while Favre (or density-weighted) averaging is useful for turbulent reacting flows.

2.3.1 Reynolds averaging

In a turbulent flow the quantities of interest can be decomposed such as

$$\psi(x_i, t) = \overline{\psi}(x_i, t) + \psi'(x_i, t), \tag{2.12}$$

where $\overline{\psi}$ denotes an average value, and ψ' is the fluctuation about the average. Decomposing the instantaneous quantities in the Navier Stokes equations and averaging the results yields a set of equations called the Reynolds Averaged Navier Stokes (RANS) equations. The continuity and momentum equations become

$$\frac{\partial \overline{\rho}}{\partial t} + \frac{\partial(\overline{\rho u_i})}{\partial x_i} = 0. \tag{2.13}$$

$$\frac{\partial(\overline{\rho u_i})}{\partial t} + \frac{\partial(\overline{\rho u_i u_j})}{\partial x_j} = -\frac{\partial \overline{p}}{\partial x_i} + \frac{\partial \tau_{ij}}{\partial x_j} - \frac{\partial(\overline{\rho}\overline{u_i' u_j'})}{\partial x_j} + B_i \tag{2.14}$$

in which density fluctuations have been neglected. The Reynolds averaging process yields new terms involving correlations of velocity fluctuations, $\overline{u_i' u_j'}$, which are termed Reynolds stresses. Closure of the Reynolds stresses can be obtained using a number of turbulence models. The scalar transport equation is treated similarly, which results in

$$\frac{\partial(\overline{\rho}\overline{\phi})}{\partial t} + \frac{\partial(\overline{\rho u_i}\overline{\phi})}{\partial x_i} = \frac{\partial}{\partial x_i}\left(\overline{\rho} D_\phi \frac{\partial \overline{\phi}}{\partial x_i}\right) - \frac{\partial(\overline{\rho}\overline{u_i' \phi'})}{\partial x_j} + \dot{\omega}, \tag{2.15}$$

In Equation 2.15 correlations of velocity and scalar fluctuations appear ($\overline{\phi' u_j'}$). These terms are referred to as turbulent scalar fluxes.

2.3.2 Favre averaging

Density fluctuations that are present in turbulent reacting flows present an added level of complexity due to correlations that arise between fluctuations in density and fluctuations in other variables. Fluctuations in temperature due to chemical reaction lead to significant density fluctuations that cannot be neglected. The use of density-weighted, or Favre averaging accounts for the density changes while providing a form of equations similar to the RANS equations. Favre-averaged quantities are defined as

$$\tilde{\psi}(x_i, t) \equiv \frac{\overline{\rho\psi}(x_i, t)}{\overline{\rho}}. \tag{2.16}$$

The instantaneous quantities present in the governing equations can be decomposed in a similar method to that used in Reynolds averaging. The instantaneous value is written as the sum of a Favre-average and a fluctuation about the average

$$\psi(x_i, t) = \tilde{\psi}(x_i, t) + \psi''(x_i, t). \tag{2.17}$$

The Favre-averaged form of the governing equations are

$$\frac{\partial \overline{\rho}}{\partial t} + \frac{\partial (\overline{\rho}\tilde{u}_i)}{\partial x_i} = 0, \tag{2.18}$$

$$\frac{\partial (\overline{\rho}\tilde{u}_i)}{\partial t} + \frac{\partial (\overline{\rho}\tilde{u}_i\tilde{u}_j)}{\partial x_j} = -\frac{\partial \overline{p}}{\partial x_i} + \frac{\partial \tau_{ij}}{\partial x_j} - \frac{\partial (\widetilde{\overline{\rho}u_i''u_j''})}{\partial x_j} + B_i, \tag{2.19}$$

$$\frac{\partial (\overline{\rho}\tilde{\phi})}{\partial t} + \frac{\partial (\overline{\rho}\tilde{u}_i\tilde{\phi})}{\partial x_i} = \frac{\partial}{\partial x_i}\left(\overline{\rho}D_\phi \frac{\partial \tilde{\phi}}{\partial x_i}\right) - \frac{\partial (\widetilde{\overline{\rho}u_i''\phi''})}{\partial x_j} + \dot{\omega}. \tag{2.20}$$

2.4 Turbulence Models

Turbulence models in RANS simulations provide closure for the correlations of velocity fluctuations, or Reynolds stresses, that appear in the averaged forms of the Navier Stokes equations. Some of the most commonly used turbulence models, such as the k-ε model, utilize an approximation called the turbulent viscosity hypothesis to provide closure. Alternatively, transport equations for the Reynolds stresses can be solved directly, as in the Reynolds Stress models. More detailed descriptions of turbulence are provided by Large Eddy Simulation (LES) and Direct Numerical Simulation (DNS), which yield unsteady predictions that resolve turbulent flow structures at the cost of increased computational expense. LES does not used averaged equations, but instead considers filtered forms of the Navier Stokes equations based upon energy-containing length scales in the flow. In DNS all scales of motion are resolved, but computational expense rises sharply with Reynolds number which limits the types of flows in which the approach is feasible.

2.4.1 Turbulent viscosity hypothesis

In the turbulent viscosity hypothesis the Reynolds stresses are assumed to be related to the mean velocity gradients in a manner analogous to viscous stresses [6].

$$\overline{\rho u_i' u_j'} = -\mu_t \left(\frac{\partial \overline{u_i}}{\partial x_j} + \frac{\partial \overline{u_j}}{\partial x_i}\right) - \frac{2}{3}\overline{\rho}\delta_{ij}\overline{k} \tag{2.21}$$

In Equation 2.21 μ_t is referred to as the turbulent viscosity. This relation is known to be inaccurate for many flows, as experiments have shown that the Reynolds stresses are not determined by local rate of strain, but instead by the total amount of strain experienced by the turbulence [6]. However, for simple free shear flows, in which the production and dissipation of turbulent kinetic energy are approximately equal, the approximation is reasonable. In these types of flows the mean velocity gradients change slowly, following the mean flow. As a result, the local mean velocity gradients characterize the history of distortion more closely.

2.4.2 Two equation models

k-ε model

The most widely used two equation model is the k-ε model [7]. The turbulent viscosity is given by

$$\mu_t = C_\mu \overline{\rho} \frac{\tilde{k}^2}{\overline{\varepsilon}}, \tag{2.22}$$

in which C_μ is a constant equal to 0.09. In this model two transport equations are solved, one for the turbulent kinetic energy, k, and one for the dissipation of turbulent kinetic energy, ε.

$$\frac{\partial}{\partial t}(\overline{\rho}\tilde{k}) + \frac{\partial}{\partial x_i}(\overline{\rho u_i}\tilde{k}) = \frac{\partial}{\partial x_i}\left[\left(\frac{\mu_t}{\sigma_k} + \mu\right)\frac{\partial \tilde{k}}{\partial x_i}\right] + P_k + G_k - \overline{\rho} + \tilde{\varepsilon}, \tag{2.23}$$

$$\frac{\partial}{\partial t}(\overline{\rho}\tilde{\varepsilon}) + \frac{\partial}{\partial x_i}(\overline{\rho u_i}\tilde{\varepsilon}) = \frac{\partial}{\partial x_i}\left[\left(\frac{\mu_t}{\sigma_\varepsilon} + \mu\right)\frac{\partial \tilde{\varepsilon}}{\partial x_i}\right] + C_{\varepsilon 1} P_k \frac{\tilde{\varepsilon}}{\tilde{k}} - C_{\varepsilon 2}\overline{\rho}\frac{\tilde{\varepsilon}^2}{\tilde{k}}. \tag{2.24}$$

The term P_k that appears in both Equation 2.23 and 2.24 accounts for turbulence production, and has the form

$$P_k = -\widetilde{u_i'' u_j''}\frac{\partial \tilde{u}_i}{\partial x_j}. \tag{2.25}$$

The term $\widetilde{u_i'' u_j''}$ in Equation 2.25 requires closure. The rate of turbulence production is modelled by the expression

$$P_k = \left(\frac{2}{3}\delta_{ij}\left[\tilde{k} - \frac{\mu_t}{\overline{\rho}}\frac{\partial \tilde{u}_k}{\partial x_k}\right] - \left[\frac{\partial \tilde{u}_i}{\partial x_j} + \frac{\partial \tilde{u}_j}{\partial x_i}\right]\right)\frac{\partial \tilde{u}_i}{\partial x_j}. \tag{2.26}$$

The turbulence quantities k and ε form a length scale and a timescale for the flow

$$L = \frac{\tilde{k}^{3/2}}{\tilde{\varepsilon}}, \tag{2.27}$$

$$\tau_t = \frac{\tilde{k}}{\tilde{\varepsilon}}. \tag{2.28}$$

The standard model constants are attributed to Launder and Sharma [8].

$$C_{\varepsilon 1} = 1.44, \;\; C_{\varepsilon 2} = 1.92, \;\; \sigma_k = 1.0, \;\; \text{and} \;\; \sigma_\varepsilon = 1.3 \tag{2.29}$$

This model has well known deficiencies, particularly for cases involving rotating flow, stream-wise pressure gradients, and curved boundary layers [7]. Most relevant to this study, the k-ε model is known to over-predict the spreading of axisymmetric jets in stagnant surroundings. This will be discussed further in Chapter 5.

k-ω model

The k-ω of Wilcox [9] is a two-equation model in which transport equations are solved for the turbulent kinetic energy, k, and the turbulence frequency, ω. The transport equation for the turbulent kinetic energy is similar to equation 2.23.

$$\frac{\partial}{\partial t}(\overline{\rho}\tilde{k}) + \frac{\partial}{\partial x_i}(\overline{\rho u_i}\tilde{k}) = \frac{\partial}{\partial x_i}\left[\left(\frac{\mu_t}{\sigma_{k1}} + \mu\right)\frac{\partial \tilde{k}}{\partial x_i}\right] + \mu_t\left(\frac{\partial \overline{u}_i}{\partial x_j} + \frac{\partial \overline{u}_j}{\partial x_i}\right)\frac{\partial \overline{u}_i}{\partial x_j} - \beta' k\overline{\rho}\omega, \tag{2.30}$$

in which $\beta' = 0.09$, and $\sigma_{k1} = 2$. The transport equation for the turbulence eddy frequency, ω, is given by

$$\begin{aligned}\frac{\partial}{\partial t}(\overline{\rho}\tilde{\omega}) + \frac{\partial}{\partial x_i}(\overline{\rho u_i}\tilde{\omega}) = \frac{\partial}{\partial x_i}\left[\left(\frac{\mu_t}{\sigma_\omega} + \mu\right)\frac{\partial \tilde{\omega}}{\partial x_i}\right] \\ +\alpha\frac{\tilde{\omega}}{\tilde{k}}\left[\mu_t\left(\frac{\partial \overline{u}_i}{\partial x_j} + \frac{\partial \overline{u}_j}{\partial x_i}\right)\frac{\partial \overline{u}_i}{\partial x_j}\right] - \beta\overline{\rho}\omega^2\end{aligned} \tag{2.31}$$

In Equation 2.31, β, α, and σ_ω are model constants equal to 0.075, 5/9, and 2 respectively. The eddy frequency is related to the dissipation by

$$\tilde{\omega} = \frac{\tilde{\varepsilon}}{\beta' k}, \tag{2.32}$$

from which the turbulent viscosity is calculated directly from the expression

$$\mu_t = \overline{\rho}\frac{\tilde{k}}{\tilde{\omega}}. \tag{2.33}$$

The k-ω is known to exhibit a high degree of sensitivity to turbulence characteristics set at boundary conditions [7]. For boundary-layer flows this model yields superior results to the k-ε model due to its treatment of the viscous near-wall region and streamwise pressure gradients. However, non-turbulent boundaries at the free-stream prove problematic, as non-zero values are ω are required, and the calculated results are known to be sensitive to the value of ω that is used [6].

2.4.3 Reynolds stress models

The Reynolds stress model does not use an eddy viscosity approximation to define expressions for the Reynolds stresses, instead using six additional transport equations to solve for the components of the Reynolds stress tensor. For high Reynolds number flows the transport equations take the form

$$\frac{\partial}{\partial t}(\overline{\rho}\overline{u_i' u_j'}) + \frac{\partial}{\partial x_i}(\overline{\rho u_i}\overline{u_i' u_j'}) = \frac{\partial}{\partial x_k}\left[\left(\nu + \frac{2}{3}C_s\frac{\tilde{k}^2}{\tilde{\varepsilon}}\right)\frac{\partial \overline{u_i' u_j'}}{\partial x_k}\right] + P_{ij} + \phi_{ij} - \frac{2}{3}\delta_{ij}\tilde{\varepsilon}. \tag{2.34}$$

In Equation 2.34, P_{ij} is the exact production term, ϕ_{ij} is the pressure-strain correlation, and C_s is a model constant. A full description of the terms in this model can be found in references [6, 7]. Since the turbulence dissipation, ε, appears in the above equation, a transport equation for ε is still required.

The increased number of equations leads to increased computational cost, and decreased numerical robustness [10]. Since a transport equation for ε is used, the Reynolds stress model is known to perform just as poorly as the $k-\varepsilon$ model in many cases due to identical issues with the ε equation [7]. While the transport equations for the Reynolds stress components provides a model that should provide a more precise description of turbulent flows,

it has been noted in many case to yield results no better than those from two-equation models [10]. There are multiple varieties of the Reynolds Stress models, which have different model constants and treatment of the pressure-strain correlation.

2.4.4 Large Eddy Simulation

Large Eddy Simulation (LES) uses a filtered form of the Navier Stokes equations, in which three-dimensional large scale flow structures which contain the majority of the energy are calculated and a sub-grid scale is utilized to account for the effect of the smaller dissipative scales. Quantities of interest, such as velocity, are decomposed into a filtered component, which is calculated, and a residual component, which is modelled. Since unsteady turbulent motion are considered explicitly, LES is attractive for flows in which unsteady large scale flow structures are significant as it should provide more accurate and detailed predictions when compared to RANS approaches [6]. In contrast to RANS simulations, LES does not provided averaged flow predictions but instead yields instantaneous quantities. The computational expense is considerably higher than those of RANS simulations, as the required grid spacing is proportional to the filter width, which ideally should be smaller than the size of the smallest energy containing motions in the flow [6]. For free shear flows the grid requirements are not as stringent as for wall-bounded flows, but the requirement for three-dimensional time dependent grids in LES adds considerable computational cost to axisymmetric flows that can be modelled utilizing symmetry in RANS approaches. In regard to turbulent reacting flows, LES accounts for large scale instabilities that are of interest in combustion applications, while RANS simulations tend to suppress instabilities [11]. Processes that are important in reacting flows, such as molecular mixing and chemical reaction, mostly occur on the subgrid scales which require modelling. Modelling approaches based upon LES have been used for high-speed compressible flows and reacting flows [6].

2.4.5 Direct Numerical Simulation

In Direct Numerical Simulation (DNS) all scales of motion are resolved in the solution of the Navier Stokes equations, providing more accuracy and a higher level of description for flows in which it can be implemented. The computational expense, higher than that of LES, increases rapidly with Reynolds number which limits the flows to which it is feasible. The grid spacing must be small enough to resolve the small dissipative scales of the flow, while the timestep is limited by considerations of numerical accuracy [6]. The majority of the enormous computational expense is associated with resolving the dissipative range of the flow. DNS studies have been implemented to determine flow statistics that are extremely difficult to determine experimentally [6]. Statistics from DNS provide valuable benchmarking data that is frequently used for evaluating performance of simpler models.

2.5 Probability Density Functions

In turbulent reacting flows velocity components and scalar quantities such as species concentrations, temperature, and pressure are stochastic variables. The fluctuations in these stochastic variables are at odds with the deterministic nature of the governing Navier-Stokes equations. However, these variables can be characterized by their probability density function (PDF) [6]. For a given stochastic variable, Φ, a corresponding independent sample space variable, ϕ, represents the potential values that Φ may take on. The probability, p, that variable Φ will be less than a given value of the sample space variable ϕ_a can be represented as

$$p_a = p(\Phi < \phi_a), \tag{2.35}$$

where $0 \leq p \leq 1$, in which 0 represents an impossible event and 1 represents a certain event. The Cumulative Distribution Function (CDF) can be used to determine the probability of any event for a given variable. The CDF is defined as

$$F(\phi) = p(\Phi < \phi). \tag{2.36}$$

The CDF is a non-decreasing function bounded by 0 and 1. Two important basic properties of the CDF are

$$F(-\infty) = 0, \tag{2.37}$$

$$F(\infty) = 1. \tag{2.38}$$

The probability that the variable Φ will lie between two values of the sample space variable ϕ is given by

$$p(\phi_a \leq \Phi < \phi_b) = F(\phi_b) - F(\phi_a) \qquad \phi_b > \phi_a. \tag{2.39}$$

The probability density function, PDF, is the derivative of the CDF with respect to the sample space variable.

$$P(\phi) \equiv \frac{dF(\phi)}{d\phi}. \tag{2.40}$$

The PDF is non-negative due to the fact that the CDF is a non-decreasing function. A few important properties of the PDF are

$$\int_{-\infty}^{\infty} P(\phi) d\phi = 1, \tag{2.41}$$

$$P(-\infty) = 0, \tag{2.42}$$

$$P(\infty) = 0. \tag{2.43}$$

The probability of the variable Φ having a value within a given interval in the sample space is determined by integrating the PDF over the interval of interest.

$$p(\phi_a \leq \Phi < \phi_b) = \int_{\phi_a}^{\phi_b} P(\phi) d\phi. \tag{2.44}$$

The expectation, or mean value, of Φ is the probability-weighted average of all potential values of Φ. This is defined as

$$\langle \Phi \rangle \equiv \int_{-\infty}^{\infty} \phi P(\phi) d\phi. \tag{2.45}$$

This expectation can be extended to any function, G, of the variable Φ

$$\langle G(\Phi) \rangle \equiv \int_{-\infty}^{\infty} G(\phi) P(\phi) d\phi. \tag{2.46}$$

According to Bayes theorem, the joint probability of two events occurring, $P(\phi_a, \phi_b)$ can be written as

$$P(\phi_a, \phi_b) = P(\phi_a|\Phi_b = \phi_b)P(\phi_b), \tag{2.47}$$

in which $P(\phi_a|\Phi_b = \phi_b)$ is the probability density for Φ_a having the value of ϕ_a for all realizations of the flow in which the condition $\Phi_b = \phi_b$ is satisfied [12]. The conditional expectation can therefore be determined by

$$\langle \Phi_a|\Phi_b = \phi_b \rangle = \frac{\int_{-\infty}^{\infty} \phi_a P(\phi_a|\Phi_b = \phi_b)P(\phi_b)d\phi_a}{P(\phi_b)}. \tag{2.48}$$

For any function, $G(\Phi_a)$, the conditional expectation can be obtained in a similar manner

$$\langle G(\Phi_a)|\Phi_b = \phi_b \rangle = \frac{\int_{-\infty}^{\infty} G(\phi_a) P(\phi_a|\Phi_b = \phi_b)P(\phi_b)d\phi_a}{P(\phi_b)}. \tag{2.49}$$

If the variables ϕ_a and ϕ_b are statistically independent the value of ϕ_a does not depend on ϕ_b and thus the unconditional expectation $\langle \Phi_a \rangle$ is equal to the conditional expectation $\langle \Phi_a|\Phi_b = \phi_b \rangle$. For cases in which ϕ_a and ϕ_b are statistically independent this can be extended to functions, $\langle G(\Phi_a) \rangle = \langle G(\Phi_a|\Phi_b = \phi_b) \rangle$.

2.6 Turbulent Reacting Flows

The accurate representation of the complex interactions between chemistry and turbulence is essential in modelling of turbulent reacting flows. For combustion to occur fuel and oxidizer must mix at the molecular level, which occurs at different time and length scales than many of the turbulent flow structures. The ratio of the turbulent time scale (τ_t) to the chemical time scale (τ_c) is used to characterize reacting flows, and is referred to as the Damköhler number.

$$D_a = \frac{\tau_t}{\tau_c}. \tag{2.50}$$

For flows in which D_a is greater than 1 reactions occur faster relative to turbulent mixing. For Damköhler numbers significantly larger than unity the reactions are considered to be

infinitely fast, and combustion may occur in thin reaction zones between the mixing fuel and oxidizer [13]. In these types of flows the overall rate of combustion is controlled by the rate of turbulent mixing. When D_a is less than 1 the chemical processes occur at a slower rate than mixing. If $D_a \ll 1$ turbulent mixing occurs far faster than chemical reaction, resulting in a 'well-stirred reactor' [13].

Relevant to this study, autoignition in engines deals with non-premixed combustion, in which the fuel and oxidizer are initially separate. Air is heated and compressed within the combustion chamber, and fuel is injected. The fuel and oxidizer mix and react during continuous interdiffusion which leads to autoignition[11]. In non-premixed combustion the mixing timescales are typically much larger than the chemical time scales (large Damköhler number), and thus an assumption of infinitely fast chemistry is often employed [11]. However, in cases when the mixing time scale is locally of the same order of magnitude as the chemical time scale finite-rate chemistry must be considered.

2.6.1 Mixture fraction

The mixture fraction, ξ, is a normalized scalar variable that is important in non-premixed reacting flows. It is defined at any location in the system, and represents the local ratio of the mass originating from the fuel stream to the total mass of the mixture.

$$\xi = \frac{mass\ originating\ from\ fuel\ stream}{total\ mass\ of\ mixture} \tag{2.51}$$

In a two-feed system, in which fuel and oxidizer are supplied separately, the mixture fraction is given by

$$\xi = \frac{\dot{m}_1}{\dot{m}_1 + \dot{m}_2} \tag{2.52}$$

where $\dot{m}_1$ represents the mass flow of fuel stream and $\dot{m}_2$ represents the mass flow of oxidizer [11]. Assuming equal species diffusivities, the mixture fraction is a conserved scalar and is governed by the transport equation

$$\frac{\partial(\rho\xi)}{\partial t} + \frac{\partial}{\partial x_i}(\rho u_i \xi) = \frac{\partial}{\partial x_i}\left(\rho D \frac{\partial \xi}{\partial x_i}\right). \tag{2.53}$$

Favre-averaging of Equation 2.53 yields

$$\frac{\partial(\bar{\rho}\tilde{\xi})}{\partial t} + \frac{\partial}{\partial x_i}\left(\bar{\rho}\tilde{u}_i\tilde{\xi}\right) = \frac{\partial}{\partial x_i}\left(\overline{\rho D}\frac{\partial\tilde{\xi}}{\partial x_i} - \bar{\rho}\widetilde{u_i''\xi''}\right). \tag{2.54}$$

in which transport due to molecular diffusion can been neglected assuming a high Reynolds number. The turbulent flux term, $\widetilde{u_i''\xi''}$ is modelled using the gradient diffusion hypothesis

$$\widetilde{u_i''\xi''} = -D_t\frac{\partial\tilde{\xi}}{\partial x_i}, \tag{2.55}$$

which is outlined further in Section 3.4.2.
The transport equation for the mean mixture fraction variance, $\widetilde{\xi''^2}$, is given by

$$\frac{\partial(\bar{\rho}\widetilde{\xi''^2})}{\partial t} + \frac{\partial}{\partial x_i}\left(\bar{\rho}\tilde{u}_i\widetilde{\xi''^2}\right) = -\frac{\partial}{\partial x_i}\left(\bar{\rho}\widetilde{u_i''\xi''^2}\right) + 2\bar{\rho}D_t\left(\frac{\partial\tilde{\xi}}{\partial x_i}\right)^2 - \bar{\rho}\tilde{\chi}. \tag{2.56}$$

The turbulent flux term, $\widetilde{v''\xi''^2}$ in Equation 2.56 is also modelled using the gradient diffusion hypothesis.

$$\widetilde{u_i''\xi''^2} = -D_t\frac{\partial\widetilde{\xi''^2}}{\partial x_i}, \tag{2.57}$$

Another term requiring consideration is the mean scalar dissipation rate, $\tilde{\chi}$. A common closure based upon assuming proportional scalar and flow time scales [11] is given by

$$\tilde{\chi} = 2\frac{\tilde{\varepsilon}}{\tilde{k}}\widetilde{\xi''^2}. \tag{2.58}$$

Further information about this closure for the mean scalar dissipation rate is given in Chapter 4.

2.7 Combustion Models

An array of modelling approaches are available for simulating turbulent reacting flows, varying in computational expense and complexity. Simple models utilize single step reactions or consider only limited combustion chemistry to approximate total energy release from combustion [7]. The Eddy Break Up model is a commonly used example of a simple combustion model. The laminar flamelet model accounts for detailed chemistry while

maintaining simplicity, allowing for intermediate and minor species to be considered. The PDF transport model does not require modelling of the chemical source term and can provide predictions considering finite-rate chemistry, but introduces additional terms that require closure. In this study Conditional Moment Closure is employed, and this model is discussed in detail in Chapter 3.

2.7.1 Eddy Break Up model

The Eddy Break Up (EBU) model was proposed by Spalding [14] as a closure for the chemical source term. The model is based upon the assumption that, for mixing-controlled reacting flows, the rate of chemical reaction is controlled by the same cascade process, from integral to dissipative length and time scales, that describes turbulent mixing [11]. The chemical time scale is expressed in terms of the turbulent mixing time scale, given by k/ε. This model was formulated primarily for premixed combustion, and for use with non-premixed combustion knowledge of the mixture fraction PDF within the solution domain is required [11]. Inherent is the assumption of a high Damköhler number, and hence fast chemistry. Since the local rate of reaction is considered to be mixing controlled it is specified as function of flow properties. The turbulent dissipation rates for fuel, oxidizer, and products are considered to be

$$\tilde{\dot{\omega}}_{fuel} = -C_R \overline{\rho} \tilde{Y}_{fuel} \frac{\varepsilon}{k}, \tag{2.59}$$

$$\tilde{\dot{\omega}}_{ox} = -C_R \overline{\rho} \frac{\tilde{Y}_{ox}}{s} \frac{\varepsilon}{k}, \tag{2.60}$$

$$\tilde{\dot{\omega}}_{pr} = -C'_R \overline{\rho} \frac{\tilde{Y}_{pr}}{1+s} \frac{\varepsilon}{k}, \tag{2.61}$$

where s is the stoichiometric oxygen to fuel mass ratio, and C_R and C'_R are model constants. A transport equation for the fuel mass fraction is solved, allowing for the three local turbulent dissipation rates to be determined [7]. The actual reaction rate of the fuel is taken to be the slowest of the three dissipation rates. The model constants need to be adjusted for a particular problem when applied in a CFD application [11]. The dependence

of the reaction rate on turbulence quantities k and ε makes the resulting predictions utterly dependent on the performance of the turbulence model. Kinetically controlled reactions can be considered by calculating the local Arrhenius kinetic reaction rate as an additional dissipation rate, and taking the actual rate of reaction to be the slowest of the fuel, oxidizer, products, or kinetic rates [7]. Intermediate and minor species are not considered.

2.7.2 Laminar flamelet model

The laminar flamelet model is a simple combustion model that allows for some detailed chemistry to be included. In the laminar flamelet model a high Damköhler number is inherently assumed, and correspondingly combustion occurs in thin sheets where chemical activity is the highest within the flow. Turbulent flames are considered to be wrinkled laminar sheets of combustion, called flamelets, that are convected by the flow. For non-premixed combustion the location of the flamelet is described by an iso-surface of the stoichiometric mixture fraction, a non-reacting quantity [11]. Thus, the transport equation for mixture fraction must be solved. Laminar flamelet equations are solved normal to the flamelet surface to determine profiles of the reactive scalars. From the solution of the equations, flamelet libraries are generated to describe the relationship between the mixture fraction and the scalar flow properties, such as temperature, species mass fractions, and density. The scalar dissipation rate, a measure of mixing at the molecular level, is incorporated in the flamelet libraries to account for the stretching of the laminar flamelets in the turbulent flow [7].

Detailed chemistry can be included in the laminar flamelet model without significant computational expense due to the use of the flamelet libraries, allowing for pollutant formation and intermediate species to be considered. In addition to relations for temperature and density, information relating to major and minor species are included in the library. The laminar flamelet structure is reasonable if the laminar flamelet thickness is thin compared to the smallest eddies in the flow [11].

2.7.3 PDF transport model

The joint PDF transport model of Pope [15] can be used for both premixed and non-premixed combustion, and does not require modelling for the chemical source term. The

transport equation for the joint PDF of the velocity and the composition variables is solved, which introduces complex terms that are conditionally averaged upon both velocity and composition and require closure. Further information regarding the derivation and form of the joint PDF transport equation can be found in references [6, 11]. This equation does not contain scalar gradients, and thus closure of viscous transport and molecular mixing terms are still required. Closure of the mixing term is a important problem in PDF methods. Including gradients in the sample space variables considered in the joint PDF transport equation would remove the need for modelling these two terms, but would add dimensionality to the problem. Due to the high dimensionality of the PDF transport equation, stemming from conditional averages based upon multiple sample space variables, finite-volume and finite-difference techniques are typically not employed [11]. In contrast, the memory requirements of Monte Carlo methods for problems with high dimensionality are considerably less, and provide more efficient solution for the PDF transport methods utilizing Lagrangian methods [16]. The performance of the PDF transport model for reacting flows is dependent upon the quality of the models that are implemented for the unclosed terms. Discussion of closures relevant to the PDF transport model is beyond the scope of this study.

2.8 Summary

This chapter presented important background information for this study, including description of the relevant experimental work. The governing equations of turbulent reacting flows were outlined, and common modelling approaches for turbulence and combustion were discussed. Favre-averaging, a concept important to turbulent reacting flows, and PDFs were defined. Non-premixed combustion and important concepts such as mixture fraction were summarized. In the following chapter a general overview of the first order Conditional Moment Closure model is provided, terms requiring closure are discussed, and relevant models are presented.

Chapter 3

Conditional Moment Closure

In this chapter Conditional Moment Closure (CMC) methods are examined. The derivation of the conditional species and enthalpy transport equations are presented, and the terms within the equations that require closure are outlined. Further, the shear flow approximation, which allows computational expense to be reduced through solving the cross-stream averaged form of the CMC equations, is discussed. Previous autoignition studies utilizing CMC are presented.

3.1 Overview

CMC is a combustion modelling approach applicable to non-premixed combustion that was developed independently by Klimenko [17] and Bilger [18], and presented in a joint paper [12]. One difficulty in predicting the flow and mixing of reacting scalars is that the rates of reaction are highly non-linear functions of species concentration and temperature. In turbulent mixing significant spatial and temporal fluctuations in these scalar quantities are present, and the non-linearity of the reaction rates leads to terms containing correlations of the scalar fluctuations. These fluctuations are very difficult to deal with and add further complexity to the already difficult problem of predicting scalar mixing. In CMC the average scalar quantities of interest, such as species concentrations and enthalpy, are conditioned on a given value of mixture fraction, ξ. The advantage of this approach is that the

fluctuations about the conditional averages are much smaller than the fluctuations about the unconditional averages. In first-order CMC these fluctuations are neglected, reducing the complexity of the conditional transport equations to be solved.

Klimenko and Bilger derived the same CMC equations from different starting points. The derivation of Klimenko [17] started from the PDF transport equation and is referred to as the joint-PDF method. Bilger [18] used a decomposition approach similar to that used in Reynolds averaging methods. In the following sections the decomposition approach of Bilger [18] is followed and the conditional species and enthalpy transport equations are presented.

3.2 Conditional Species Transport Equation

For a given species α, the conditional average of the mass fraction Y_α is defined as:

$$Q_\alpha(\eta, \mathbf{x}, t) = \frac{\langle \rho Y_\alpha(\mathbf{x}, t) | \xi(\mathbf{x}, t) = \eta \rangle}{\langle \rho | \eta \rangle}, \tag{3.1}$$

where ξ is the mixture fraction and η is a sample variable in mixture fraction space. The angular brackets denote a conditional average over an ensemble of realizations of the flow, subject to the condition to the right of the vertical bar. Only the specific instances of the overall ensemble in which the condition is met are included in the average. The mass fraction of species α, Y_α, can be decomposed into

$$Y_\alpha(\mathbf{x}, t) = Q_\alpha(\xi(\mathbf{x}, t), \mathbf{x}, t) + y''_\alpha(\mathbf{x}, t), \tag{3.2}$$

in which $y''_\alpha(\mathbf{x}, t)$ is the fluctuation about the conditional average. By definition,

$$\langle y''_\alpha(\mathbf{x}, t) | \eta \rangle = 0. \tag{3.3}$$

The conditional species equation is derived from the transport equation for Y_α

$$\frac{\partial(\rho Y_\alpha)}{\partial t} + \frac{\partial(\rho u_i Y_\alpha)}{\partial x_i} = \frac{\partial}{\partial x_i}\left(\rho D_\alpha \frac{\partial Y_\alpha}{\partial x_i}\right) + \dot{\omega} \tag{3.4}$$

It is assumed that the individual species diffusivities are equal, such that $D_\alpha = D$. Substitution of Equation 3.2, followed by conditional averaging over η yields

$$\langle \rho | \eta \rangle \frac{\partial(Q_\alpha)}{\partial t} + \langle \rho | \eta \rangle \langle u_i | \eta \rangle \frac{\partial(Q_\alpha)}{\partial x_i} = \langle \rho | \eta \rangle \frac{\langle \chi | \eta \rangle}{2} \frac{\partial^2 Q_\alpha}{\partial \eta^2} + e_Q + e_y + \langle \dot{\omega} | \eta \rangle, \tag{3.5}$$

in which

$$\langle \chi | \eta \rangle = 2D \frac{\partial^2 Q_\alpha}{\partial \eta^2} \tag{3.6}$$

is the conditional scalar dissipation rate. The terms e_Q and e_y are unclosed, and providing closure for them is referred to as the primary closure hypothesis [12]. These terms are given by the expressions

$$e_Q = \left\langle \left[\frac{\partial}{\partial x_i} \left(\rho D \frac{\partial Q_\alpha}{\partial x_i} \right) + \rho D \nabla \xi \cdot \nabla \frac{\partial Q_\alpha}{\partial \eta} \right] | \eta \right\rangle, \tag{3.7}$$

$$e_y = - \left\langle \left[\rho \frac{\partial y''_\alpha}{\partial t} + \rho u_i \frac{\partial y''_\alpha}{\partial x_i} - \frac{\partial}{\partial x_i} \left(\rho D \frac{\partial y''_\alpha}{\partial x_i} \right) \right] | \eta \right\rangle. \tag{3.8}$$

When the Reynolds number is large, e_Q becomes small and can be neglected [12],

$$e_Q \simeq 0. \tag{3.9}$$

Following Bilger [18], the basic closure hypothesis used in the decomposition approach is

$$e_y = - \frac{1}{P(\eta)} \frac{\partial}{\partial x_i} \left(\langle \rho | \eta \rangle \langle u''_i y'' | \eta \rangle P(\eta) \right). \tag{3.10}$$

Using the definition of the Favre averaged PDF

$$\widetilde{P}(\eta) = \frac{\langle \rho | \eta \rangle P(\eta)}{\langle \rho \rangle} \tag{3.11}$$

in which $\langle \rho \rangle$ is the unconditional density, Equation 3.5 becomes

$$\begin{aligned} \frac{\partial (Q_\alpha)}{\partial t} + \langle u_i | \eta \rangle \frac{\partial (Q_\alpha)}{\partial x_i} = \frac{1}{\langle \rho \rangle \widetilde{P}(\eta)} \frac{\partial}{\partial x_i} \left(\langle \rho \rangle \langle u''_i y''_\alpha | \eta \rangle \widetilde{P}(\eta) \right) \\ + \frac{1}{2} \langle \chi | \eta \rangle \frac{\partial^2 Q_\alpha}{\partial \eta^2} + \frac{\langle \dot{\omega} | \eta \rangle}{\langle \rho | \eta \rangle}, \end{aligned} \tag{3.12}$$

On the left hand side of Equation 3.12, the first term represents the local rate of change of the conditional species mass fraction while the second term is the conditional transport by convection. On the right hand side the first term accounts for transport by the turbulent flux, the second term represents mixing at the molecular level, and the third term is the chemical source representing the change in conditional species mass fraction due to chemical reaction.

3.3 Conditional Enthalpy Equation

The transport equation for the conditional average enthalpy, $Q_h = \langle h|\eta\rangle$, is derived from the unconditional enthalpy transport equation

$$\frac{\partial(\rho h)}{\partial t} + \frac{\partial(\rho u_i h)}{\partial x_i} = \frac{\partial}{\partial x_i}\left(\rho D_\alpha \frac{\partial h}{\partial x_i}\right) + \frac{\partial p}{\partial x_i} + \dot{q}_{rad}. \tag{3.13}$$

Following the procedure used for the species concentrations, the conditional enthalpy is defined as

$$Q_h(\eta, \mathbf{x}, t) = \langle h(\mathbf{x}, t)|\xi(\mathbf{x}, t) = \eta\rangle, \tag{3.14}$$

which allows for the enthalpy to be decomposed as

$$h(\mathbf{x}, t) = Q_h(\xi(\mathbf{x}, t), \mathbf{x}, t) + h''(\mathbf{x}, t). \tag{3.15}$$

Substitution of Equation 3.15 into the enthalpy transport equation, followed by conditional averaging with respect to η yields

$$\begin{aligned}\frac{\partial Q_h}{\partial t} + \langle u_i|\eta\rangle \frac{\partial Q_h}{\partial x_i} = &-\frac{1}{\langle\rho\rangle\tilde{P}(\eta)}\frac{\partial}{\partial x_i}(\langle\rho\rangle \langle u_i'' h''|\eta\rangle \tilde{P}(\eta)) + \frac{1}{2}\langle\chi|\eta\rangle \frac{\partial^2 Q_h}{\partial \eta^2} \\ &+\frac{1}{\langle\rho|\eta\rangle}\left\langle\frac{\partial p}{\partial t}|\eta\right\rangle - \frac{\langle\dot{q}_{rad}|\eta\rangle}{\langle\rho|\eta\rangle}.\end{aligned} \tag{3.16}$$

On the left hand side of Equation 3.16 the first term is the local rate of change of the conditional enthalpy, and the second term accounts for conditional convective transport. On the right hand side the first term represents enthalpy transport by the turbulent flux, while the second term is enthalpy dissipation. The third term is the pressure work term, and the fourth term accounts for radiation.

3.4 Terms Requiring Closure

In the conditional species and conditional enthalpy transport equations there are multiple terms that require closure. The closures used for these terms are discussed in this section.

3.4.1 Conditional Chemical Source Term

The conditional chemical source term represents the production of species by chemical reaction. In a simple, one-step irreversible reaction

$$A + B \rightarrow Products \tag{3.17}$$

the chemical source term, representing the rate of formation of products, is given by the expression

$$\dot{\omega} = \rho k(T) Y_A Y_B, \tag{3.18}$$

in which $k(T)$ the reaction rate constant and Y_A and Y_B are the species mass fractions of species A and B respectively. The rate constant is calculated using the equation

$$k(T) = A_0 T^{\beta} exp\left(\frac{-T_a}{T}\right). \tag{3.19}$$

In Equation 3.19 A_0 is the frequency factor, β is the temperature exponent, and T_a is the activation temperature.

The unconditional chemical source term, $\dot{\omega}$, is a non-linear function of the species mass fractions and enthalpy. Thus, the unconditional averages of the $\dot{\omega}$ are not functions of the unconditional averages of species mass fractions and enthalpy, due to the fluctuations present in Y and h.

$$\langle \dot{\omega_\alpha}(Y,T) \rangle \neq \dot{\omega_\alpha}(\langle Y \rangle, \langle T \rangle) \tag{3.20}$$

The unconditional average of the chemical source term requires the fluctuations to be taken into account.

$$\langle \dot{\omega_\alpha}(Y,T) \rangle = \langle \dot{\omega_\alpha}(\langle Y \rangle + y', \langle T \rangle + T') \rangle \tag{3.21}$$

However, the conditional fluctuations in Y and T are known to be considerably smaller than the unconditional fluctuations in many cases

$$\begin{aligned} y'' &\ll y', \\ T'' &\ll T'. \end{aligned} \tag{3.22}$$

Therefore, taking the average of the chemical source term, conditioned on a specific value of mixture fraction,

$$\langle \dot{\omega_\alpha}(Y,T)|\eta\rangle = \langle \dot{\omega_\alpha}(\langle Y|\eta\rangle + y'', \langle T|\eta\rangle + T'')|\eta\rangle \tag{3.23}$$

will allow the conditional fluctuations to be neglected in a first-order closure of the chemical source term.

$$\begin{aligned}\langle \dot{\omega_\alpha}(Y,T)|\eta\rangle &\simeq \langle \dot{\omega_\alpha}(\langle Y|\eta\rangle, \langle T|\eta\rangle)|\eta\rangle \\ &= \dot{\omega_\alpha}(\langle Y|\eta\rangle, \langle T|\eta\rangle).\end{aligned} \tag{3.24}$$

The accuracy of the first order closure depends on how large the neglected conditional fluctuations are. For many cases they are small, but their size depends on the configuration of the flow and the nature of the chemical reactions [12]. Applying the same notation used in Section 3.2 for the conditional species mass fractions and temperature,

$$Q_A = \langle Y_A|\eta\rangle, \qquad Q_B = \langle Y_B|\eta\rangle, \qquad Q_T = \langle T|\eta\rangle, \tag{3.25}$$

Klimenko and Bilger [12] expanded Equation 3.24 using a Taylor series expansion and conditionally averaged the resulting expression, yielding

$$\begin{aligned}\langle \dot{\omega}|\eta\rangle \simeq \langle \rho|\eta\rangle k(Q_T) Q_A Q_B \Bigg[1 + \frac{\langle y_A'' y_B''|\eta\rangle}{Q_A Q_B} + \left(\beta + \frac{T_a}{Q_T}\right)\left(\frac{\langle y_A'' T''|\eta\rangle}{Q_A Q_T} + \frac{\langle y_B'' T''|\eta\rangle}{Q_B Q_T}\right) \\ + \frac{1}{2}\left(\beta(\beta-1) + \frac{2(\beta-1)T_A}{Q_T} + \frac{T_a^2}{Q_T^2}\right)\frac{\langle (T'')^2|\eta\rangle}{Q_T^2}\Bigg].\end{aligned} \tag{3.26}$$

For small fluctuations about the conditional averages of species mass fraction and temperature all terms on the right hand side of Equation 3.26, with the exception of the first term, can be neglected, giving

$$\langle \dot{\omega}|\eta\rangle \simeq \langle \rho|\eta\rangle k(Q_T) Q_A Q_B. \tag{3.27}$$

Equation 3.27 represents the first order closure of the conditional chemical source term. The error invoked in this closure will be small if the variances of conditional species mass fractions and temperature are small relative to the square of their conditional means [12].

3.4.2 Turbulent Flux

Another unclosed term that requires treatment is the conditional turbulent transport flux, $\langle u_i'' \phi'' | \eta \rangle$. This term appears in both the conditional species transport equation (as $\langle u_i'' y_\alpha'' | \eta \rangle$) and in the conditional temperature equation (as $\langle u_i'' T'' | \eta \rangle$). These terms are modelled using the gradient diffusion hypothesis, which states that the turbulent transport of a conserved scalar, ϕ, is down the mean scalar gradient [6]. The transport is treated in a way analogous to molecular diffusion, such that

$$\langle u_i'' \phi'' \rangle = -D_T \frac{\partial \phi}{\partial x_i}, \tag{3.28}$$

where D_T is the turbulent diffusivity. The turbulent diffusivity is a positive scalar that is related to the turbulent viscosity, ν_T, through the expression

$$D_T = \frac{\nu_T}{Sc_T}, \tag{3.29}$$

in which Sc_T is the turbulent Schmidt number, which is taken to have a value of 0.9. The turbulent viscosity is calculated using

$$\nu_T = C_\mu \frac{k^2}{\varepsilon}, \tag{3.30}$$

where the constant C_μ is equal to 0.09. Substitution of this relation into Equation 3.29 gives a simple expression for the turbulent diffusivity

$$D_T = \frac{C_\mu}{Sc_T} \frac{k^2}{\varepsilon}. \tag{3.31}$$

The conditional turbulent flux is found by taking the conditional mean of Equation 3.28. This yields closure for the flux terms appearing in the conditional species transport and temperature equations.

$$\langle u_i'' y_\alpha'' | \eta \rangle = -D_T \frac{\partial \langle y_\alpha | \eta \rangle}{\partial x_i}, \tag{3.32}$$

$$\langle u_i'' T'' | \eta \rangle = -D_T \frac{\partial \langle T | \eta \rangle}{\partial x_i}. \tag{3.33}$$

3.4.3 Conditional velocity

The conditional velocity is an unclosed term that appears directly in the CMC equations. Two models for the conditional velocity are used in this study: the linear model [19] and the gradient diffusion model of Pope [20].

Linear model

The linear model [19] is commonly used for the conditional velocity in CMC implementations [12]. It assumes the conditional velocity has a radial dependence on η, as described by

$$\langle u_i|\eta\rangle = \tilde{u}_i + \frac{\widetilde{u_i''\xi''}}{\widetilde{\xi''^2}}\left(\eta - \tilde{\xi}\right), \tag{3.34}$$

where $\tilde{u}_i$ is the Favre-averaged velocity, $\tilde{\xi}$ the Favre-averaged mixture fraction, $\widetilde{\xi''^2}$ the Favre-averaged mixture fraction variance and $\widetilde{u_i''\xi''}$ the turbulent scalar flux. This expression is exact for jointly Gaussian turbulence and is considered to be a good approximation for flows in which values of η are within two standard deviations of $\tilde{\xi}$ [21]. Although experimental data [19] and DNS [22] support the linear relationship around the local mean mixture fraction, for large values of $|\eta - \tilde{\xi}|$ the deviations of the conditional velocity from linear behaviour can be significant, even in simple mixing layers [23]. This model has the advantage of being simple to implement and is numerically well-behaved for all values of η.

Gradient model

The gradient diffusion model of Pope [20] is analogous to turbulent transport modelling using the gradient diffusion hypothesis

$$\langle u_i|\eta\rangle = \tilde{u}_i - \frac{D_t}{\widetilde{P}(\eta)}\frac{\partial \widetilde{P}(\eta)}{\partial x_i}, \tag{3.35}$$

in which D_t is the turbulent diffusivity. Unlike the linear model, the gradient model is the only model that, when used with presumed PDF methods, is completely consistent

with the moments of conserved scalars [24]. However, the accuracy of the model depends upon how well the presumed PDF models the true PDF. For the β-PDF, de Bruyn Kops and Mortensen [23] observed that the conditional velocity diverges to $\pm\infty$ when values of $\tilde{P}(\eta)$ approach zero, but matched DNS data well in regions where the β-PDF was in good agreement with the DNS PDF. However, since the departures from expected behaviour occur at low probability densities, the effect on overall mixing could be small [23]. The numerical difficulties arising from dividing by the PDF will be examined further.

3.4.4 Probability Density Function

The PDF is a very important unclosed term in CMC. It appears not only in the conditional species and temperature equations but, as outlined in Chapter 4, can also impact the conditional scalar dissipation rate models. Two commonly used closures for the PDF are the β-PDF and the clipped Gaussian PDF. Other methods of determining the PDF have been used, such as the presumed mapping function approach [25], but are beyond the scope of this study. In this work the β-PDF is implemented.

β-PDF

The β-PDF is commonly used in CMC. It has been implemented for CMC studies of ignition for methane jets [26, 27], fuel spray [28, 29], n-heptane plume [30], and in many other applications [31, 32, 33, 34]. The β-PDF is given by the expression

$$P(\eta) = \frac{\eta^{\alpha-1}(1-\eta)^{\beta-1}}{I_b} \quad \text{with} \quad I_b = \int_0^1 \eta^{\alpha-1}(1-\eta)^{\beta-1} d\eta. \tag{3.36}$$

The two parameters that characterize the PDF, α and β, are calculated from the flow field solution using the Favre-averaged mixture fraction, $\tilde{\xi}$, and its variance $\widetilde{\xi''^2}$, using

$$\alpha = \tilde{\xi}\left(\frac{\tilde{\xi}\left(1-\tilde{\xi}\right)}{\widetilde{\xi''^2}} - 1\right) \quad \text{and} \quad \beta = \left(1-\tilde{\xi}\right)\left(\frac{\tilde{\xi}\left(1-\tilde{\xi}\right)}{\widetilde{\xi''^2}} - 1\right). \tag{3.37}$$

Equation 3.36 yields a smooth PDF that asymptotes to infinity when the mixture approaches the bounds of mixture fraction space, $\eta = 0$ and $\eta = 1$ [12]. The β-PDF has

been shown to characterize flow with homogeneous turbulence very well by Girimaji [35], which is supported by the DNS results of Swaminathan et al. [36]. Similarly, Mortensen et al. [37] compared β-PDF profiles with DNS data for a scalar mixing layer and found good agreement. However, there is no physical explanation for this good agreement and its applicability for inhomogeneous flows may be questionable [38, 39].

Clipped Gaussian PDF

The clipped Gaussian PDF differs most significantly from the β-PDF at the upper and lower bounds of mixture fraction space, $\eta = 0$ and $\eta = 1$. Unlike the β-PDF, the clipped Gaussian form assumes delta function components at the unmixed limits of η. These delta functions represent an assumption that the statistics in scalar space are intermittent in nature at the upper and lower bound, and as a result do not asymptote to infinity at these limits [12]. The expression for the clipped Gaussian PDF is

$$P(\eta) = \gamma_1 \delta(\eta) + (1 - \gamma_1 - \gamma_2) P_t(\eta) + \gamma_2 \delta(1 - \eta), \tag{3.38}$$

where $P_t(\eta)$ represents the Gaussian PDF form for the mixed fluid, given by

$$P_t(\eta) = \frac{G(\eta)}{\int_0^1 G(\eta) d\eta}, \tag{3.39}$$

in which

$$G(\eta) = \frac{1}{\sigma_g \sqrt{(2\pi)}} exp\left(-\frac{(\eta - \xi_g)^2}{2\sigma_g^2}\right). \tag{3.40}$$

In Equation 3.38 γ_1 and γ_2 represent the strength of the delta functions in unmixed fluid states corresponding to $\eta = 0$ and $\eta = 1$, and $\delta(x)$ is the Dirac delta function. The parameters ξ_g and σ_g in Equation 3.38 are the mean and variance of the unclipped Gaussian form, which can be related to the mean and variance of the mixture fraction [12].

3.4.5 Conditional scalar dissipation rate

The closure of the conditional scalar dissipation rate, $\langle \chi | \eta \rangle$, forms the main focus of this study. Characterizing $\langle \chi | \eta \rangle$ is not straightforward, and many models have been proposed.

Four models are examined, two of which (AMC [40] and the presumed β-PDF model of Girimaji [39]) invoke assumptions of homogeneous turbulence. The other two mixing models are different forms of an inhomogeneous model proposed by Devaud et al. [21], differing only by the conditional velocity model that is used in their respective formulations. Further details about these models are provided in Chapter 4.

3.5 Shear Flow Approximation

In self-similar regions of free shear flows, such as the turbulent round jet, the radial dependence of the conditional average of the species concentrations is very small [12]. This fact is not at all intuitive, as the unconditional means of species concentrations have a strong radial dependence, but it is supported by asymptotic analysis [41]. However, Klimenko [17] suggests that the radial dependence of the PDF should be assumed to be greater than that of the conditional mean concentrations. To account for this dependence, the PDF-weighted axial component of the CMC equations is integrated in the radial direction. This procedure allows for the CMC equations to be greatly simplified, reducing the calculations required from three dimensions to one dimension. This simplification is referred to as the shear flow approximation. This approximation has been successfully applied in CMC by De Paola et al. [31] and Markides et al. [30] for n-heptane plumes, and by Woolley et al. [42] for soot formation in non-premixed flames. In their three-dimensional simulations of combustion within a diesel engine, De Paola et al. [32] examined the effect of cross-stream averaging and found that the results compared well with experimental data. In the current study the methane fuel jet is developing, and thus the assumption of self-similarity may not be accurate in all regions of the jet. This simplification will be discussed further in Chapter 5.

3.6 Previous Autoignition Studies Using CMC Methods

The previous CMC autoignition work of El Sayed [43] and El Sayed et al. [26, 44] examined autoignition of high pressure methane jets in a shock tube, based upon experimental results of Wu [5]. Two homogeneous scalar dissipation rate models, Amplitude Mapping Closure (AMC) and Girimaji's presumed β-PDF model, were applied to cross-stream averaged CMC simulations for methane and methane based fuel blends [44] utilizing the same flow conditions examined in this study. Both models gave similar results. The trend of predicted ignition delays were in reasonable agreement with experimental data, but an over-prediction at low air temperatures and an under-prediction at high air temperatures were noted. Detailed and optimized chemical kinetics were included and were unlikely to be the source of the discrepancies. The scalar dissipation rate was found to be a dominant term in the CMC equations, and hence improvement on the turbulent mixing model could bring more accurate autoignition predictions. Additionally, the autoignition behaviour of high pressure methane jets from a larger diameter injector was examined [26, 43].

First order CMC has also been successfully applied in autoignition studies of methane and methane-based blends [27], heptane [30], and spray [28, 29]. Doubly-conditioning methods have been investigated for simplified cases of ignition [45]. De Paola et al.[31] applied a complete second order closure model to model autoignition and concluded that first order closure was sufficient when there was a rapid decay of the conditional scalar dissipation rate below its critical value. Three-dimensional CMC calculations of diesel engine simulations using Reynolds Averaged Navier Stokes equations (RANS) [32] have been recently reported.

Bushe and Steiner [46] proposed a modelling approach based upon CMC, called Conditional Source-term Estimation (CSE). In contrast to CMC, CSE does not increase the dimensionality of the equations. Variations of this approach have been implemented by Huang and Bushe [47] and Grout et al.[48] to examine autoignition of high pressure methane jets in a shock tube. Both implementations showed good agreement with experimental data, although an underprediction of ignition delay at high air temperatures was observed in the results of Huang and Bushe [47] when utilizing a temperature-based ignition criterion.

3.7 Summary

This chapter gave an overview of first order CMC. The conditional species and temperature equations were derived, and terms requiring closure were outlined. Treatment of the chemical source term with the first order closure was discussed, along with closures for the turbulent flux and conditional velocity. The presumed form of the β-PDF was explained, and the required closure of the conditional scalar dissipation rate, which forms the focus of the next chapter, was introduced. Simplification of the CMC equations through the use of cross-stream averaging was advocated through the use of the shear flow approximation. Previous studies using CMC to examine autoignition behaviour were presented. In the present study two forms of a turbulent mixing model presented by Devaud et al. [21], based upon inhomogeneous turbulence, are implemented to assess their impact on the predictions of autoignition. In the following chapter the closure of the conditional scalar dissipation rate using these turbulent mixing models is discussed.

Chapter 4

Turbulent Mixing Models

Turbulent mixing models, which provide closure for the conditional scalar dissipation rate, are the subject of this chapter. The significance of scalar dissipation rate in turbulent reacting flows is reviewed. Two commonly used models based upon the assumption of homogeneous turbulence are presented, along with the two formulations of an inhomogeneous model which serve as the basis for this study. The validity of all four models is discussed.

4.1 Mean Scalar Dissipation Rate

The scalar dissipation rate, $\tilde{\chi}$, is an important quantity in turbulent reacting flows as it describes the rate of mixing at the molecular level. The mean value of $\tilde{\chi}$ represents the average rate at which half the scalar variance declines in homogeneous turbulent mixing [49], thus it is an important term in the mixture fraction variance transport equation (Equation 2.56). This term has units of s^{-1} and is defined as the product of the mean square gradient of the scalar and the molecular diffusivity of the scalar, given by $\tilde{\chi} \equiv 2\mathrm{D}\left(\frac{\partial\tilde{\xi}}{\partial x_i}\frac{\partial\tilde{\xi}}{\partial x_i}\right)$. Higher values of scalar dissipation rate indicate higher levels of molecular mixing. Above a critical value of $\tilde{\chi}$ within a reacting flow, local heat losses exceed chemical heat release, and extinction can occur [7]. For non-premixed flows with fast chemistry the rate of chemical reaction is strongly related to the local scalar dissipation [49].

4.1.1 Closure of mean scalar dissipation rate

Following Peters [11], an expression for the mean value of $\tilde{\chi}$ can be obtained assuming proportionality of timescales. An integral scalar time scale for the mixing field can be defined as

$$\tau_i = \frac{\tilde{\xi}''^2}{\tilde{\chi}}, \tag{4.1}$$

and an integral time scale for the flow is

$$\tau = \frac{\tilde{k}}{\tilde{\varepsilon}}. \tag{4.2}$$

The two time scales are commonly set to be proportional to each other, with the constant of proportionality, C_χ, of the order of unity [11].

$$\tau = C_\chi \tau_i. \tag{4.3}$$

Substitution of Equations 4.1 and 4.2 into Equation 4.3 yields

$$\tilde{\chi} = C_\chi \frac{\tilde{\varepsilon}}{\tilde{k}} \tilde{\xi}''^2. \tag{4.4}$$

Janicka and Peters [50] found that a value of $C_\chi = 2.0$ worked well for an inert jet of methane. Substitution of this value provides a commonly used expression for calculation of the mean value of the scalar dissipation rate

$$\tilde{\chi} = 2 \frac{\tilde{\varepsilon}}{\tilde{k}} \widetilde{\xi''^2}. \tag{4.5}$$

In this study Equation 4.5 is implemented as closure for $\tilde{\chi}$ in the transport equation for the mean mixture fraction variance, Equation 2.56. Other closures are available for the mean value of χ. Pope [51] along with Jones and Musonge [52] suggested using a transport equation to solve for $\tilde{\chi}$. This approach allows for the scalar dissipation rate to be more dependent on the characteristics of turbulent flow field [11]. However, additional terms involving the turbulent fluxes in the transport equations require closure.

4.2 Conditional Scalar Dissipation Rate

In the context of CMC, the conditional average of the scalar dissipation rate at a given value η, of the mixture fraction, ξ, is of great importance. This term appears as a key term in the CMC equations. In previous work on autoignition, El Sayed and Devaud [26] showed that $\langle\chi|\eta\rangle$ is very significant in the transient mixing prior to ignition, and therefore the scalar dissipation rate model could have a substantial impact on the predictions of autoignition. Evaluation of $\langle\chi|\eta\rangle$ is not straightforward, and a range of different turbulent mixing models have been proposed to provide closure for this term. Two of the most commonly used models, the AMC model and Girimaji's presumed β-PDF model, incorporate an assumption of homogeneous turbulence. More recently Devaud et al.[21] proposed a turbulent mixing model without assuming homogeneous turbulence, through the integration of the PDF transport equation. In the context of CMC, previous studies have implemented mixing models based only upon homogeneous turbulence [26, 27, 28, 29, 30, 31, 32, 33, 44]. In contrast, only a few studies have used conditional scalar dissipation rate models based upon inhomogeneous turbulence within CMC. The inhomogeneous model of Devaud et al.[21] was applied by Cleary and Kent [53] in CMC simulations of hood fires, and by Rogerson et al.[34] for a bagasse-fired boiler. Both studies used the gradient diffusion model for conditional velocity within the inhomogeneous mixing model. Sreedhara et al. [54] applied a similar inhomogeneous mixing model formulation, that was obtained by integrating the cross-stream averaged PDF transport equation, to piloted jet and bluff-body flames. In [54] the cross-stream averaged PDF transport equation was used to avoid numerical difficulty in low probability regions. In [53] the inhomogeneous mixing model was found to have only a small impact on the conditional species concentrations and temperature. Sreedhara et al. [54] noted that in their cross-stream averaged mixing model formulation the difference between using the linear and gradient diffusion conditional velocity models was negligible. Compared to AMC and Girimaji's model, their inhomogeneous profiles of the scalar dissipation rate yielded similar values, but showed asymmetric behaviour that differed from the symmetric homogeneous models.

While these previous CMC studies have found little improvement in predictions when using inhomogeneous mixing models, the transient fuel jet development considered in the present study is significantly different in nature. In the early stages of mixing within a developing mixing layer the turbulent flowfield is far from homogeneous, and thus mix-

ing models considering inhomogeneous turbulence are expected to have a larger impact. In contrast to the previous three studies ([34, 53, 54]), the conditional scalar dissipation rate model will be solved for transient conditions. To the author's best knowledge the inhomogeneous model has never been implemented for transient conditions or for autoignition problems. Two versions of the inhomogeneous model of Devaud et al. [21] will be implemented in this study, and compared with previous results obtained using AMC and Girimaji's model [44] in addition to the experimental results of Wu [5]. The first version of the inhomogeneous model utilizes the linear model for conditional velocity, while the second uses the gradient diffusion model.

4.3 Mixing Models Based on Homogeneous Turbulence

Two commonly used homogeneous turbulent mixing models, AMC [40] and Girimaji's presumed β-PDF model [39], are briefly described. Both models are derived from the homogeneous PDF transport equation with a double-delta initial distribution, representing initially unmixed scalars.

4.3.1 Girimaji's model

The formulation of Girimaji's model [39] is based upon the observation that the β-PDF accurately describes the evolution of the scalar PDF in statistically stationary, isotropic turbulence over all stages of two-scalar, constant density mixing [35]. An expression for the conditional scalar dissipation rate is obtained by integrating the homogeneous PDF transport equation over mixture fraction space, yielding

$$\langle \chi | \eta \rangle = -2\tilde{\chi} \frac{\tilde{\xi}(1-\tilde{\xi})}{\widetilde{\xi''^2}} \frac{J(\eta)}{\tilde{P}(\eta)}, \tag{4.6}$$

where $\tilde{\chi}$ is the Favre-averaged, unconditional scalar dissipation rate given by Equation 4.5. $J(\eta)$ is an integral expression defined as

$$J(\eta) = \int_0^\eta \left\{ \tilde{\xi}(\ln \eta' - J_1) + (1-\tilde{\xi}) \left[\ln(1-\eta') - J_2 \right] \right\} \tilde{P}(\eta')(\eta - \eta')\, d\eta', \tag{4.7}$$

where

$$J_1 = \int_0^1 \ln \eta \, d\eta, \quad \text{and} \quad J_2 = \int_0^1 \ln(1-\eta) \, d\eta. \tag{4.8}$$

Girimaji's model is derived based upon statistically stationary, isotropic turbulence. In its formulation it is restricted to homogeneous flow conditions, and may not be valid in shear layers.

4.3.2 Amplitude Mapping Closure

The AMC model utilizes the mapping closure solution of Gao [55] for the PDF in the homogeneous PDF transport equation. It assumes the PDF initially has a double-delta distribution and relaxes to a Gaussian distribution. The conditional mean scalar dissipation rate is described by the expression

$$\langle \chi | \, \eta \rangle = \chi_0 G(\eta). \tag{4.9}$$

The function $G(\eta)$ is determined by

$$G(\eta) = \exp\left\{-2\left[\text{erf}^{-1}(2\eta - 1)\right]^2\right\}, \tag{4.10}$$

in which erf^{-1} is the inverse error function. In Equation 4.9 the term χ_0 represents the expression

$$\chi_0 = \frac{\tilde{\chi}}{\int_0^1 G(\eta)\tilde{P}(\eta)d\eta}, \tag{4.11}$$

where $\tilde{\chi}$ is the mean value given in Equation(4.5). $G(\eta)$ is independent of flow field properties, such as $\tilde{\xi}$ and $\tilde{\xi}''^2$, and yields a maximum value at $\eta = 0.5$. The scalar dissipation rate profile from AMC is symmetrical about $\eta = 0.5$. AMC requires some unmixed fluid to always be present, which can be problematic at later stages of mixing.

4.4 Mixing Models Based on Inhomogeneous Turbulence

The turbulent mixing model proposed by Devaud et al. [21] does not invoke the assumption of homogeneous turbulence. Thus, this new method is applicable to a much wider range of flows compared to previous homogeneous turbulence based expressions. The model was presented in two formulations. The first formulation was the result of direct integration of the PDF transport equation in mixture fraction space, yielding an equation that was suitable for finite volume discretization with no prior assumption regarding the form of the PDF required. The second formulation took a two-parameter presumed form of the PDF, in which the parameters were functions of mixture fraction and the variance. In the present study, it is found that the first formulation of $\langle\chi|\eta\rangle$ is better suited to implementation in the commercial finite-volume CFD code, CFX [10], due to a smaller number of intermediate calculations. The derivation is briefly summarized below.

The derivation of the inhomogeneous scalar dissipation rate model is based upon the PDF transport equation, which is given by

$$\frac{\partial\langle\rho\rangle\tilde{P}(\eta)}{\partial t}+\frac{\partial}{\partial x_i}\left(\langle\rho\rangle\langle u_i|\eta\rangle\tilde{P}(\eta)\right)=-\frac{\partial^2}{\partial\eta^2}\left(\frac{1}{2}\langle\rho\rangle\tilde{P}(\eta)\langle\chi|\eta\rangle\right), \tag{4.12}$$

where $\langle u_i|\eta\rangle$ is the conditional velocity and $\tilde{P}(\eta)$ is the Favre-averaged PDF. In Equation 4.12, macrotransport by molecular diffusion is neglected assuming a large Reynolds number. The conditional scalar dissipation rate, $\langle\chi|\eta\rangle$, can be determined by doubly integrating Equation 4.12. However, in order to complete this process, the conditional velocity, $\langle u_i|\eta\rangle$, requires closure.

4.4.1 Linear conditional velocity model

For simplicity, the linear model [19] is commonly used in CMC in order to determine the conditional velocity and is given by

$$\langle u_i|\eta\rangle=\tilde{u}_i+\frac{\widetilde{u_i''\xi''}}{\widetilde{\xi''^2}}\left(\eta-\tilde{\xi}\right), \tag{4.13}$$

where $\tilde{u}_i$ is the Favre-averaged velocity, $\tilde{\xi}$ the Favre-averaged mixture fraction, $\widetilde{\xi''^2}$ the Favre-averaged mixture fraction variance and $\widetilde{u_i''\xi''}$ the turbulent scalar flux. Further information regarding the model is provided in Chapter 3. Substitution of Equation 4.13 into the PDF transport equation (Equation 4.12) yields

$$\frac{\partial\langle\rho\rangle\tilde{P}(\eta)}{\partial t}+\frac{\partial}{\partial x_i}\left(\langle\rho\rangle\tilde{u}_i\tilde{P}(\eta)\right)+\frac{\partial}{\partial x_i}\left[\langle\rho\rangle\tilde{P}(\eta)\frac{\widetilde{u_i''\xi''}}{\widetilde{\xi''^2}}\left(\eta-\tilde{\xi}\right)\right]= -\frac{\partial^2}{\partial\eta^2}\left(\frac{1}{2}\langle\rho\rangle\tilde{P}(\eta)\langle\chi|\eta\rangle\right). \tag{4.14}$$

The double integration of Equation 4.14 in mixture fraction space gives an expression for $\langle\chi|\eta\rangle$:

$$\frac{1}{2}\tilde{P}(\eta)\langle\chi|\eta\rangle=-\frac{1}{\langle\rho\rangle}\left[\frac{\partial\langle\rho\rangle\widetilde{I}_1(\eta)}{\partial t}+\frac{\partial}{\partial x_i}\left(\langle\rho\rangle\tilde{u}_i\widetilde{I}_1(\eta)+\langle\rho\rangle\frac{\widetilde{u_i''\xi''}}{\widetilde{\xi''^2}}\widetilde{I}_2(\eta)\right)\right], \tag{4.15}$$

where the terms I_1 and I_2 are given by the following expression

$$\tilde{I}_n=\int_\eta^1(\eta^0-\eta)(\eta^0-\tilde{\xi})^{n-1}\tilde{P}(\eta^0)d\eta^0,\quad n=1,2. \tag{4.16}$$

Rearranging Equation 4.15, while making use of the equations of continuity and transport of $\tilde{\xi}$, results in

$$\frac{1}{2}\tilde{P}(\eta)\langle\chi|\eta\rangle=\underbrace{-\frac{\partial}{\partial t}\widetilde{I}_1(\eta)}_{\text{Term I}}+\underbrace{\left[-\tilde{u}_i\frac{\partial\widetilde{I}_1(\eta)}{\partial x_i}\right]}_{\text{Term II}}+\underbrace{\left[-\widetilde{u_i''\xi''}\frac{\partial}{\partial x_i}\left(\frac{\widetilde{I}_2(\eta)}{\widetilde{\xi''^2}}\right)\right]}_{\text{Term III}}+ \underbrace{\left(\frac{\widetilde{I}_2(\eta)}{\widetilde{\xi''^2}}\right)\left[\frac{\partial\tilde{\xi}}{\partial t}+\tilde{u}_i\frac{\partial\tilde{\xi}}{\partial x_i}\right]}_{\text{Term IV}}, \tag{4.17}$$

Equation 4.17 is in a form that can be implemented into a flow field solver. This version of the inhomogeneous model for $\langle\chi|\eta\rangle$ will be referred to as Inhomogeneous-Linear in the subsequent sections.

4.4.2 Gradient diffusion conditional velocity model

The validity of the linear model can be questioned for more complex flows where significant deviations of mixture fraction from its mean are present. In the CMC governing equations

spatial transport, including the conditional velocity, is usually very small compared to the other terms, such as micro-mixing and chemical source term. This explains why previous studies [53, 54] did not observe any significant impact of the conditional velocity model on their results. However, in the present situation, the model for the conditional velocity is present in the equation for the conditional scalar dissipation rate, term of prime importance in CMC at the early stages of mixing. It has been shown that the use of the linear conditional velocity model is not consistent with the second moment of conserved scalars with presumed PDF methods [21]. Mortensen [38] proposes to use the gradient diffusion model of Pope [20], as it is the only known conditional velocity model that is consistent with the moments of the conserved scalars. Following Mortensen's work, it is decided to use the gradient diffusion model for the conditional velocity in the present inhomogeneous model for $\langle\chi|\eta\rangle$. The gradient diffusion model gives

$$\langle u_i|\eta\rangle = \tilde{u}_i - \frac{D_t}{\widetilde{P}(\eta)}\frac{\partial \widetilde{P}(\eta)}{\partial x_i}, \tag{4.18}$$

D_t being the turbulent diffusivity. Substitution of Equation 4.18 into Equation 4.12 gives:

$$\frac{\partial\langle\rho\rangle\tilde{P}(\eta)}{\partial t} + \frac{\partial}{\partial x_i}\left(\langle\rho\rangle\tilde{u}_i\tilde{P}(\eta)\right) - \frac{\partial}{\partial x_i}\left(\langle\rho\rangle D_t\frac{\partial\widetilde{P}(\eta)}{\partial x_i}\right) = -\frac{\partial^2}{\partial\eta^2}\left(\frac{1}{2}\langle\rho\rangle\tilde{P}(\eta)\langle\chi|\eta\rangle\right). \tag{4.19}$$

Following the same methodology as in Section 4.4.1, the conditional scalar dissipation rate can be found by integrating Equation 4.19 twice in mixture fraction space. The integration yields

$$\frac{\partial\langle\rho\rangle\widetilde{I}_1(\eta)}{\partial t} + \frac{\partial}{\partial x_i}\left(\langle\rho\rangle\tilde{u}_i\widetilde{I}_1(\eta)\right) - \frac{\partial}{\partial x_i}\left(\langle\rho\rangle D_t\frac{\partial\widetilde{I}_1(\eta)}{\partial x_i}\right) = -\frac{1}{2}\langle\rho\rangle\tilde{P}(\eta)\langle\chi|\eta\rangle. \tag{4.20}$$

Rearrangement of Equation 4.20. making use of the continuity equation, gives a simplified form

$$\frac{1}{2}\tilde{P}(\eta)\langle\chi|\eta\rangle = \underbrace{-\frac{\partial}{\partial t}\widetilde{I}_1(\eta)}_{\text{Term I}} + \underbrace{\left[-\tilde{u}_i\cdot\frac{\partial\widetilde{I}_1(\eta)}{\partial x_i}\right]}_{\text{Term II}} + \underbrace{\frac{1}{\langle\rho\rangle}\frac{\partial}{\partial x_i}\left(\langle\rho\rangle D_t\frac{\partial\widetilde{I}_1(\eta)}{\partial x_i}\right)}_{\text{Term 3}}. \tag{4.21}$$

The first two terms on the right hand side of Equation 4.21 are the same as those in Equation 4.21, and retain the labels of 'term I' and 'term II' used in the Inhomogeneous-Linear expression. The third term, labelled 'term 3', is where the Inhomogeneous-Gradient model

differs from the Inhomogeneous-Linear model. As for Equation 4.17 using the linear model, Equation 4.21 is implemented directly into the flow field solution within CFX. This version of the inhomogeneous model using the gradient model for the conditional velocity will be noted Inhomogeneous-Gradient in the following sections. Further details on the implementation are given in Section 5.6.

The accuracy of the inhomogeneous turbulent mixing model depends on how well the presumed form of the PDF and modelled conditional velocity characterize the actual PDF and conditional velocity of the flow respectively. Even though the β-PDF is known to characterize the scalar PDF well for homogeneous turbulence, there is no theoretical explanation for this good agreement and its applicability for inhomogeneous flows may be questionable [38, 39]. Girimaji [35, 39] examined the accuracy of the β-PDF for a range of simple turbulent flows and concluded that it appears to be a good approximation, particularly after the early stages of mixing. Devaud et al. [21] compared the results from the inhomogeneous model (using the linear conditional velocity model) with those of DNS for turbulent mixing in a channel flow and showed very good agreement. Girimaji's β-PDF model was also examined. The inhomogeneous model yielded scalar dissipation rate profiles much closer to the DNS data than Girimaji's model. Girimaji's model was shown to predict a peak in scalar dissipation rate at a higher mixture fraction than the inhomogeneous model, and significantly overpredicted the DNS data for rich mixtures.

4.5 Summary

This chapter outlined the importance of the scalar dissipation rate in turbulent reacting flows. Two commonly used mixing models based upon homogeneous turbulence, AMC and Girimaji's presumed β-PDF model, were presented. Two forms of a mixing model based on inhomogeneous turbulence were derived. This model was derived from the PDF transport equation, and the two formulations differed based on the closure for the conditional velocity term. The linear and gradient diffusion conditional velocity models were examined. The computational approach used for the turbulent flow field and in the solution of the CMC equations are outlined in the following chapter.

Chapter 5

Computational Method

In this chapter the details of the turbulent flow field solution are provided. The computational approach of El Sayed et al. [26, 44] serves as the basis for the numerical method used in this study. The frozen mixing assumption allows the physical flow field to be solved independently of the CMC calculations. The overall solution methodology for the flow field and the CMC calculations is outlined, and the computational domain is described. Initial conditions and boundary conditions are presented, and the implementation of the inhomogeneous mixing models in the flow field solution is explained. Model assumptions and simplifications are discussed.

5.1 Frozen Mixing Assumption

In this study the calculation of the turbulent flow field is decoupled from the CMC routines. This allows for the flow field calculations to be performed first, and subsequently used as an input for the CMC calculations. This approximation, referred to as the frozen mixing assumption, is valid only for early stages of mixing, prior to ignition. Before ignition occurs the density and temperature variations in the jet are small due to slow reaction rates, and have little effect on the flow field. As a result, the variations can be neglected by decoupling the flow field solution from the CMC calculations, allowing the flow field to be solved as a non-reacting field. This approach has been used successfully in previous CMC

studies of autoignition [26, 30, 31, 44]. The changes in density and temperature become very significant after ignition, thus this technique is not applicable in the presence of flames.

5.2 Solution Methodology

The frozen mixing assumption simplifies the autoignition simulations as it allows the solution to be split into separate steps. The turbulent flow field solution considers the mixing of fuel and oxidizer within the shock tube, and does not require chemical kinetics to be considered. Data libraries are exported from the completed flow field solution, and then cross-stream averaged, to provide the necessary inputs for CMC calculations of species concentrations and enthalpy. An overview of the solution procedure is presented in Figure 5.1.

A 63 node grid is used in mixture fraction space. This grid has even spacing of 0.00275 between $\eta = 0$ and $\eta = 0.1$, a region containing the stoichiometric mixture fraction ($\eta_{st} = 0.055$) and the most reactive mixture fraction, which is on the lean side of stoichiometry (at around $\eta = 0.02$ [44]). This lean mixture region is where chemical activity is highest and ignition will occur, and thus a fine grid is required. For η values above 0.1, the grid is progressively coarsened up to the pure fuel limit of $\eta = 1$. A flow field simulation coupled with routines to perform the mixing model calculations is performed for each value of η in the mixture fraction grid. At 50 μs intervals in time 63 output files are generated from the flow field solutions, one for each of the 63 values in the mixture fraction grid. These output files each contain radial profiles of flow field data at 28 axial locations, equally spaced by 2.5 mm. A cross-stream averaging routine is implemented for each timestep, reading in the 63 flow field output files and outputting cross-stream averaged conditional quantities in one input file for the CMC calculations. In conjunction with previous work [26, 43, 44] a 75 K rise in the local conditional temperature is used as the criterion for autoignition. El Sayed [43] examined other ignition criteria for a similar autoignition problem, such as temperature exceeding 2000 K and maximum heat release rate, and found that they yielded slightly longer ignition delays but similar ignition locations.

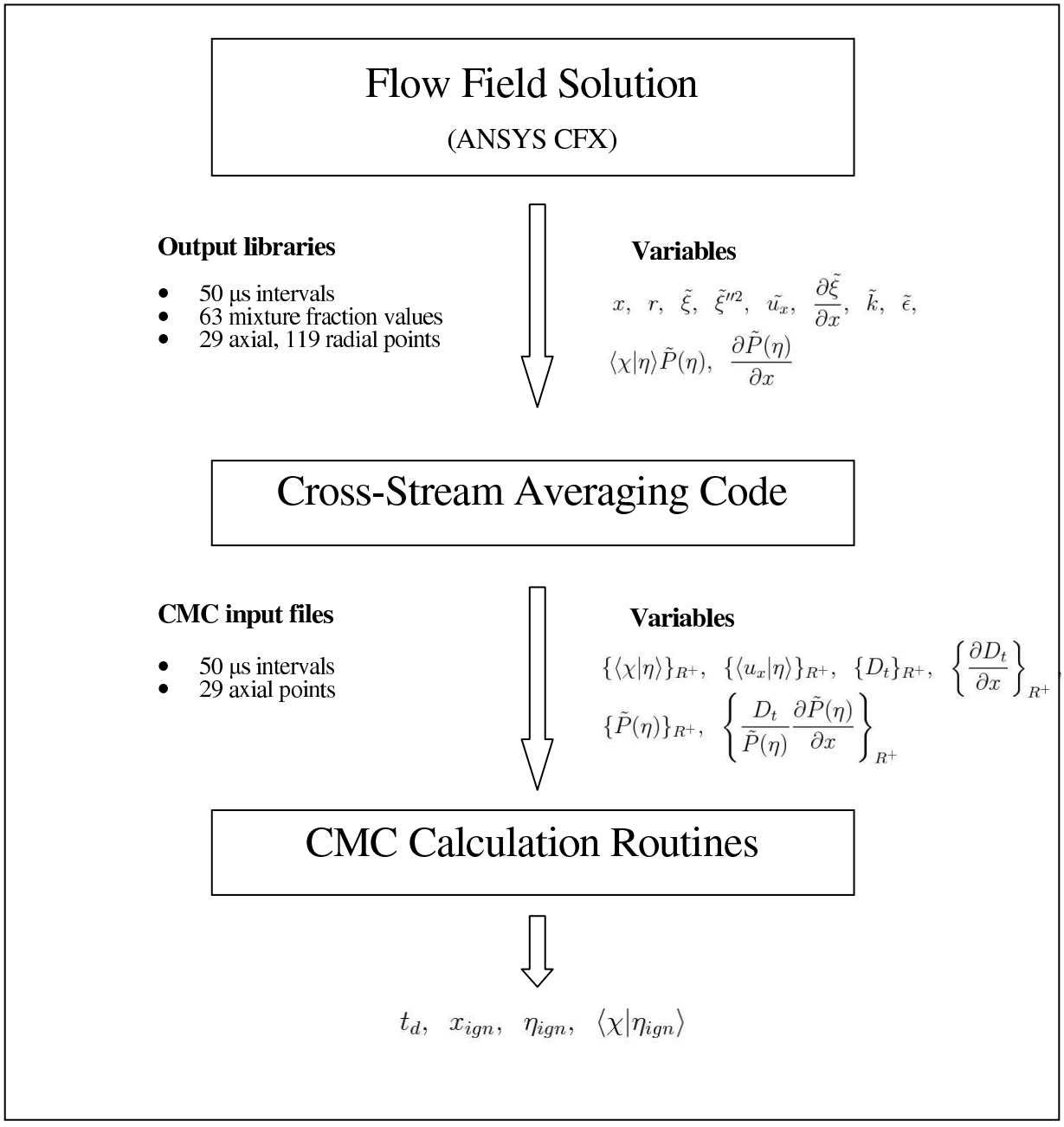

Figure 5.1: Outline of solution procedure.

5.3 Turbulent Flow Field Simulation

The axisymmetric computational domain used for the flow field solution has dimensions of 0.1 m in length and 0.029 m in the radial direction. The domain represents one half of the experimental shock tube test section due to symmetry in the geometry and flow. Three-dimensional domains and meshes are required by the CFD code, ANSYS CFX 11.0. Thus, a 5° wedge cutting through the centreline of the shock tube is defined. The computational domain is shown in Figure 5.2. The overall domain length is shorter than the full length of the shock tube in the experiments due to the fact that ignition observed in the experimental study always occurred within the first few centimetres of the injector exit [5]. An axisymmetric unstructured mesh is used, consisting of 259 x 72 x 1 unevenly spaced nodes in the axial, radial and circumferential directions, respectively. The mesh density is the highest at the fuel inlet and in the region in which ignition is expected, to more accurately capture the sharp gradients. Several meshes and domain lengths were tested and the results presented in this study were shown to be grid independent [44].

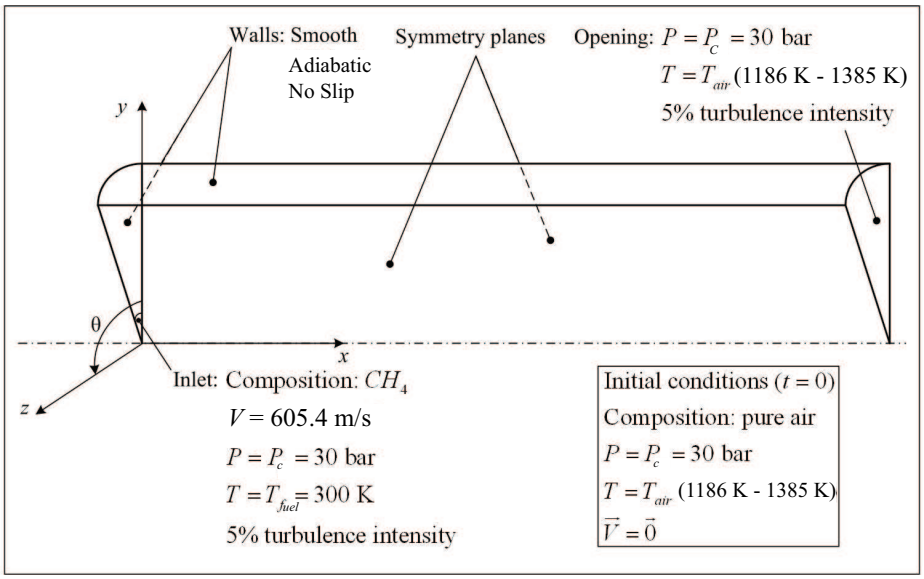

Figure 5.2: Shock tube computational domain and boundary conditions. Modified from [26].

The turbulent mixing field is solved in the commercial CFD software package ANSYS CFX 11.0 [10] using the standard k-ε model. Additional transport equations for the mean mixture fraction (Equation 2.54) and its variance (Equation 2.56) are solved within CFX. These additional variables allow for the calculation of the β-PDF at each location in the flow field domain. The advection terms are discretized using the second-order high resolution scheme. The time-dependent terms are discretized using the implicit second-order backwards Euler scheme. An adaptive solution timestep, varied between a minimum of $10^{-10}s$ and a maximum of $10^{-6}s$ is utilized to maintain Courant numbers below 5. A maximum of 15 coefficient loops are used for each timestep, and solver convergence is based upon maximum residuals dropping below 10^{-3}.

5.3.1 Initialization and boundary conditions

The domain is initialized with pure air at average temperatures and pressures taken from the experimental data sets [5]. The boundary conditions are summarized on Figure 5.2. The walls of the shock tube test section are assumed to be smooth and adiabatic with no-slip conditions. Due to the very short time periods being examined (less than 3 ms), there is insufficient time for significant heat transfer from the flow to the walls of the shock tube. Following the experimental conditions [5], a Mach number equal to 1 (choked flow) and temperature of 300 K are set at the inlet. The inlet fuel velocity is defined by assuming an isentropic expansion of the methane jet from the injection pressure of 120 bar to the chamber pressure of approximately 30 bar. The resulting injection velocity was found to be 608 m/s corresponding to a Reynolds number of 3.57×10^5. Following the experiments, the injection duration of the methane is 1 ms. After 1 ms the inlet is set to be a wall boundary condition, and fuel is no longer injected into the computational domain.

5.4 Turbulence Model

The k-ε turbulence model is well known to overpredict the spreading rate of steady state round jets [6]. The larger rate of spreading directly coincides with an underprediction of

Table 5.1: k-ε model constants

	$C_{\varepsilon 1}$	$C_{\varepsilon 2}$
Launder and Sharma[8] (standard constants)	1.44	1.92
Pope [56]	1.60	1.92
Ouellette and Hill [57]	1.52	1.92

the penetration length of developing, axisymmetric jets. One method that can be used to correct this is the modification of the k-ε model constants, $C_{\varepsilon 1}$ and/or $C_{\varepsilon 2}$. Most commonly, the value of $C_{\varepsilon 1}$ is increased while the standard value of $C_{\varepsilon 2}$ is retained. The standard model constants, as well as two recommended modifications, are presented in Table 5.1.

One issue with modifying the constants $C_{\varepsilon 1}$ or $C_{\varepsilon 2}$ is that none of the suggested modifications are universal. Pope suggests modifying the constant $C_{\varepsilon 1}$ to 1.60 to improve the predictions of turbulent round jets with the k-ε model, but notes that any generality of the model is lost in doing so [56]. Ouellette and Hill [57] examined predictions of penetration length predicted by the k-ε model for transient fuel jets at engine relevant conditions, and found that changing $C_{\varepsilon 1}$ to 1.52 improved the results.

5.4.1 Penetration length

No experimental data is available for the turbulent velocity and mixing fields in the shock tube for the present conditions. Instead, the predicted transient jet penetration length was compared with the correlation developed by Hill and Ouellette [57] for transient compressible jets at similar conditions. The penetration length is defined as the distance along the jet centerline extending from the origin to the point where the fuel mass fraction becomes zero. The correlation was successfully tested against non-reacting experimental data in the same shock tube used in the present study by Huang and Bushe [47]. The correlation is of the form

$$\frac{Z}{d\sqrt{\frac{\rho_n}{\rho_c}}} = \Gamma \left(\frac{\pi}{4}\right)^{\frac{1}{4}} \left(\frac{u_n t}{d\sqrt{\frac{\rho_n}{\rho_c}}}\right)^{\frac{1}{2}}, \tag{5.1}$$

in which Z is the penetration length, ρ_n is the density at the nozzle, ρ_c is the density within the chamber, u_n is the velocity at the nozzle, d is the diameter of the nozzle, and Γ is a

constant equal to 3.0 ± 0.1.

In previous work examining a similar flow configuration utilizing a larger diameter fuel injector, El Sayed [43] found that setting $C_{\varepsilon 1}$ to 1.535 yielded the best agreement with the penetration length correlation. The modification suggested by Pope [56] ($C_{\varepsilon 1} = 1.60$) yielded an underprediction of the jet penetration length, while the standard model constant ($C_{\varepsilon 1} = 1.44$) yielded an overprediction [43]. The jet penetration length for the flow examined in this study utilizing $C_{\varepsilon 1} = 1.535$ is compared with the standard k-ε model results, and with the correlation of Ouellette and Hill [57] in Figure 5.3.

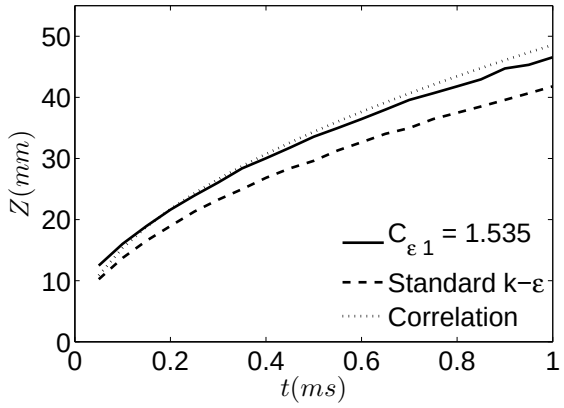

Figure 5.3: Penetration length results for $T_{air} = 1337$ K.

The jet penetration length results yield identical conclusions to those found by El Sayed [43]. Setting $C_{\varepsilon 1}$ to 1.535 results in the jet penetration length matching the correlation well. The standard $C_{\varepsilon 1}$ value of 1.44 yields lower jet penetration lengths, ranging from 18% lower at 0.05 ms to 10% lower at 1 ms.

However, the homogeneous mixing model results of El Sayed et al. [44] for the same flow configuration examined in this study use the standard k-ε model constants. The main objective of this study is to examine the impact of the mixing models based upon inhomogeneous turbulence on the autoignition predictions, and thus maintaining the same parameters in the turbulent flow field solution is desirable. To examine the relative effect on the autoignition results by modifying $C_{\varepsilon 1}$ to 1.535, a full autoignition simulation was performed at $T_{air} = 1337$ K using the AMC mixing model. The difference in the ignition delay was found to be less than 2%, while the ignition location moved 5 mm further

downstream. Thus, with the current results it is concluded that the ignition delays are not significantly affected by the standard k-ε model, while the resulting ignition locations are further upstream than they would be with a modified value of $C_{\varepsilon 1}$.

5.5 Flow Field Simplification

To reduce the large computational cost of the simulations, the flow field solution for the air temperature of $T_{air} = 1337$ K is used for all five air temperatures examined in this study. To examine the impact of this simplification, profiles of mean mixture fraction and its variance are plotted along the centreline (at the ignition time obtained using AMC [44]) and compared with profiles from the other air temperatures in Figures 5.4 to 5.7. For the two air temperatures closest to 1337 K ($T_{air} = 1385$ K in Figure 5.4 and $T_{air} = 1294$ K in Figure 5.5) the difference in the profiles of $\tilde{\xi}$ and $\widetilde{\xi''^2}$ is negligible. There are very small departures from the profiles of the 1337 K flowfield at the tip of the jet, but they are not expected to have any impact on the autoignition results. The mixture fraction decreases rapidly along the centreline in the inlet region, from a value of 1 (pure fuel) at the inlet. Closer to the tip of the jet the decrease in $\tilde{\xi}$ becomes more gradual, due to the spreading of the fuel jet. The mixture fraction variance reaches a peak early in the inlet region, where gradients are high, and decreases with increasing axial distance in a manner similar to mixture fraction.

For the two lowest air temperatures ($T_{air} = 1238$ K in Figure 5.6 and $T_{air} = 1186$ K in Figure 5.7), in which ignition is expected after the 1 ms duration of fuel injection, the difference between the profiles of $\tilde{\xi}$ and $\widetilde{\xi''^2}$ are more significant further downstream. Near the tip of the jet the flow field from $T_{air} = 1337$ K predicts higher values of mean mixture fraction, indicating a slightly higher penetration length. The overall trend of the profiles remains identical, with a shift of values by a small degree downstream. For $T_{air} = 1238$ K and $T_{air} = 1186$ K, the differences at the ignition location (from the AMC results [44]) are small. At $T_{air} = 1238$ K, ignition was predicted at 30 mm, and for $T_{air} = 1186$ K ignition was predicted at 37.5 mm. At both locations the relative difference in mean mixture fraction and variance are small. Further, the overall predicted behaviour of the flow field remains the same. The spike in $\widetilde{\xi''^2}$ that is observed at the tip of the jet at $T_{air} = 1238$ K and $T_{air} = 1186$ K is due to sharp gradients of mixture fraction in the axial direction that

are present at the tip of the jet. This increase in variance at the jet tip is also present for the higher air temperatures, but is not as noticeable as it is for the lower temperatures. The reason for this is that the gradients in the inlet region are much higher for those higher temperature flow fields due to the fact that the times in which the $\widetilde{\xi''^2}$ profiles are being examined are, unlike the lowest temperatures, during methane injection. The fact that injection has ceased can be observed in the mixture fraction profiles, which increase with increasing axial distance, from 0 (pure air) at the inlet rather than 1 (pure fuel). The values for $\tilde{\xi}$ along the centreline for T_{air} = 1238 K and T_{air} = 1186 K are considerably smaller than those observed for the higher air temperatures, falling below 0.1 and 0.05 respectively.

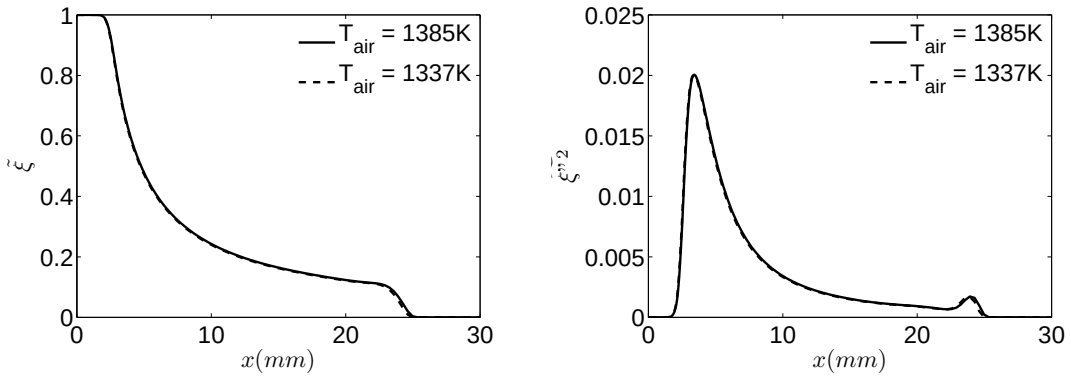

Figure 5.4: Centreline profiles of $\tilde{\xi}$ and $\widetilde{\xi''^2}$ at t = 0.37 ms.

To examine the difference in the flow fields near expected ignition, the radial profiles of mean mixture fraction and its variance are also examined for each air temperature at the time and axial location of predicted ignition from previous results using the AMC model [44]. These profiles are presented in Figures 5.8 to 5.11. The results coincide with the trends noted in the profiles of $\tilde{\xi}$ and $\widetilde{\xi''^2}$ along the centreline. or the two air temperatures closest to 1337 K (T_{air} = 1385 K in Figure 5.8 and T_{air} = 1294 K in Figure 5.9) the difference in the profiles of $\tilde{\xi}$ and $\widetilde{\xi''^2}$ is negligible. Once again, a larger degree of difference is noted for the two lowest air temperatures, T_{air} = 1238 K in Figure 5.10 and T_{air} = 1186 K in Figure 5.11. The overall trend of the radial profiles remains the same, but the 1337 K flow field predicts higher mean mixture fraction and variance for T_{air} = 1238 K near

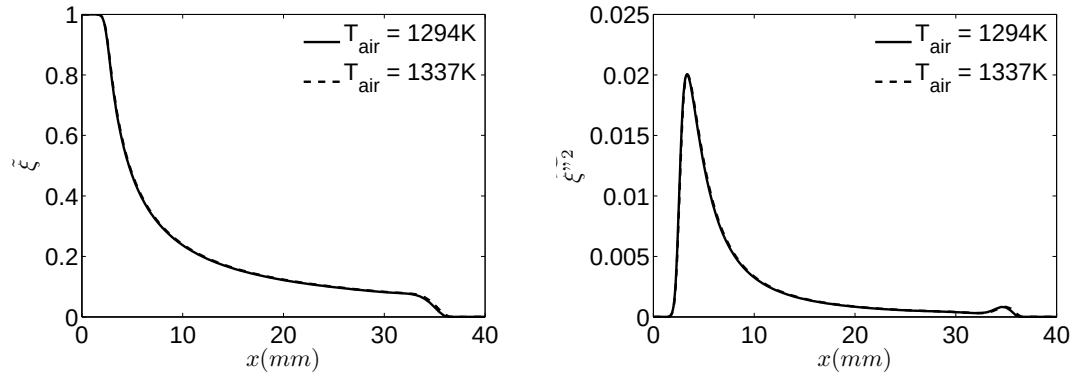

(a) (b)

Figure 5.5: Centreline profiles of $\tilde{\xi}$ and $\widetilde{\xi''^2}$ at t = 0.80 ms.

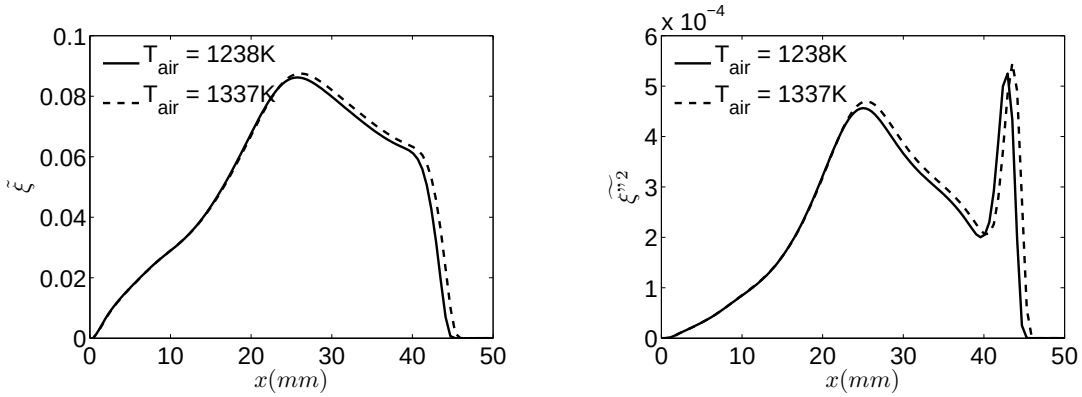

(a) (b)

Figure 5.6: Centreline profiles of $\tilde{\xi}$ and $\widetilde{\xi''^2}$ at t = 1.25 ms.

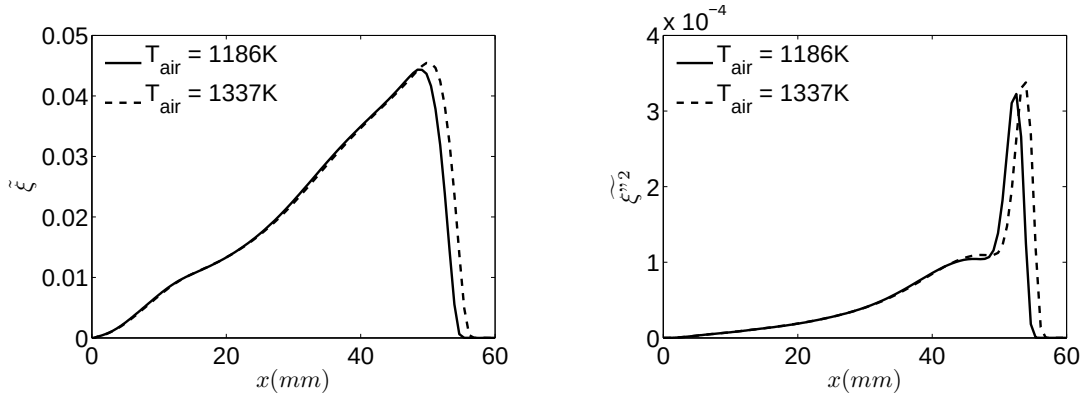

(a) (b)

Figure 5.7: Centreline profiles of $\tilde{\xi}$ and $\widetilde{\xi''^2}$ at t = 1.95 ms.

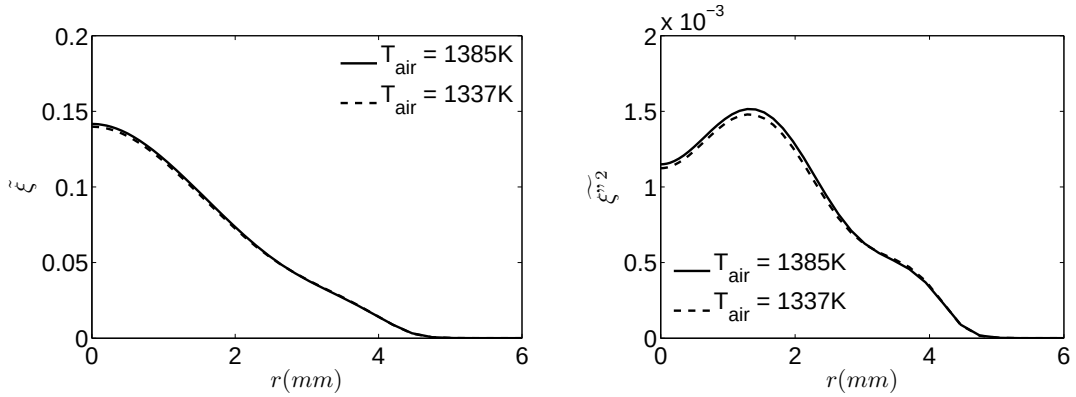

(a) (b)

Figure 5.8: Radial profiles of $\tilde{\xi}$ and $\widetilde{\xi''^2}$ at x = 17.5 mm, t = 0.37 ms.

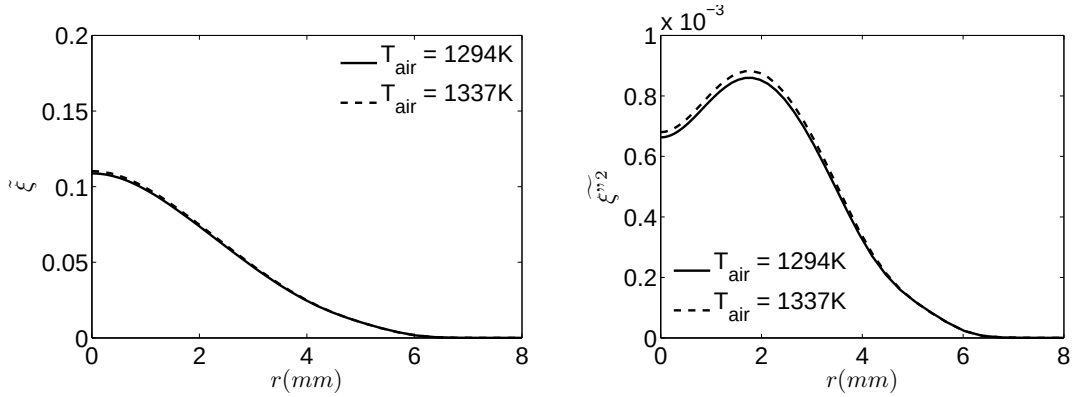

(a) (b)

Figure 5.9: Radial profiles of $\tilde{\xi}$ and $\widetilde{\xi''^2}$ at x = 22.5 mm, t = 0.80 ms.

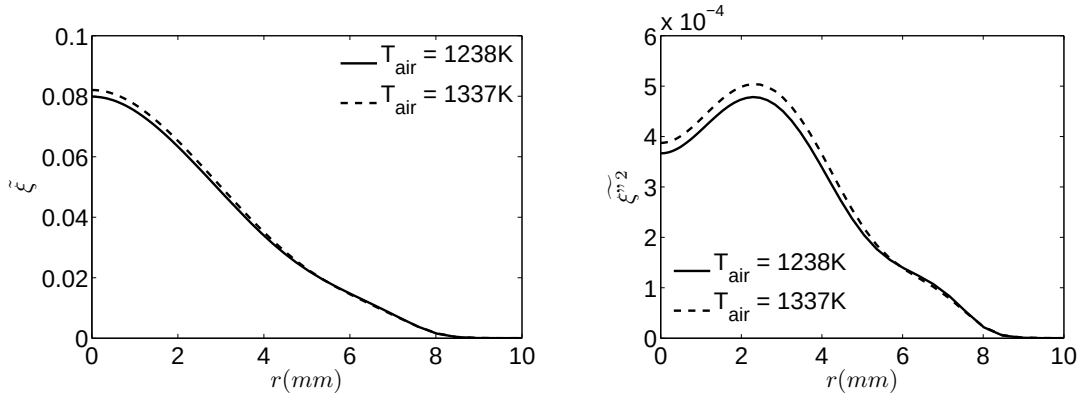

(a) (b)

Figure 5.10: Radial profiles of $\tilde{\xi}$ and $\widetilde{\xi''^2}$ at x = 30 mm, t = 1.25 ms.

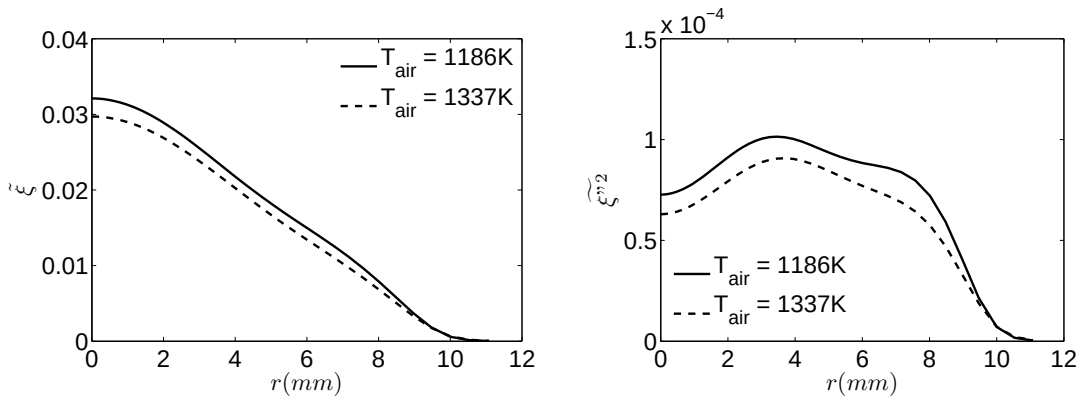

(a) (b)

Figure 5.11: Radial profiles of $\tilde{\xi}$ and $\widetilde{\xi''^2}$ at x = 37.5 mm, t = 1.95 ms.

the centreline. In contrast, the 1337 K flow field yields lower values for both $\tilde{\xi}$ and $\widetilde{\xi''^2}$ for T_{air} = 1186 K. The reason for the difference can be observed by examining the centreline profiles in Figures 5.6 and 5.7. At x = 30 mm in Figure 5.6 (for T_{air} = 1238 K), both $\tilde{\xi}$ and $\widetilde{\xi''^2}$ are in an area of negative slope as this is a location near the tip of the jet, behind the leading spherical vortex, where gradients of the mean mixture fraction are getting smaller due to mixing. In the 1337 K flow field the increased jet penetration length means that this region of decreasing mixture fraction and variance is shifted slightly upstream, which results in larger values of $\tilde{\xi}$ and $\widetilde{\xi''^2}$ across the jet. At x = 37.5 mm in Figure 5.7 (for T_{air} = 1186 K), it can be seen that the AMC ignition location is in a region where both mean mixture fraction and its variance are increasing with axial location. Unlike the 1238 K flow field, there is not a region behind the tip of the jet in which $\tilde{\xi}$ and $\widetilde{\xi''^2}$ are decreasing, due to the fact that the profiles in Figure 5.7 are at a much later time (considerably after ignition of fuel has ceased) and far more mixing has taken place. Thus, the increased jet penetration length in the 1337 K flow field results in lower values of $\tilde{\xi}$ and $\widetilde{\xi''^2}$ in the radial profiles.

The use of the 1337 K flow field for all five air temperatures is not expected to have a large effect on the autoignition results. The behaviour of mean mixture fraction and its variance remains identical, and the small difference in the flow fields lies in the degree of jet penetration. For the lowest two air temperatures, the difference in jet penetration may cause a small impact on the predicted axial ignition location. However, the downstream

shift in centreline profiles of $\tilde{\xi}$ and $\widetilde{\xi''^2}$ observed in Figures 5.6 and 5.7 is on the order of the axial grid spacing, and thus the resulting change is expected to be very minor.

5.6 Mixing Model Implementation

Equations 4.17 and 4.21 are implemented into ANSYS CFX 11.0 through the use of FORTRAN routines. For consistency with the CMC calculations, a presumed β PDF form is selected and is given by

$$P(\eta) = \frac{\eta^{\alpha-1}(1-\eta)^{\beta-1}}{I_b} \quad \text{with} \quad I_b = \int_0^1 \eta^{\alpha-1}(1-\eta)^{\beta-1} d\eta. \tag{5.2}$$

The parameters α and β are calculated from the flow solution using the Favre-averaged mixture fraction, $\tilde{\xi}$, and its variance $\widetilde{\xi''^2}$, using

$$\alpha = \tilde{\xi}\left(\frac{\tilde{\xi}\left(1-\tilde{\xi}\right)}{\widetilde{\xi''^2}} - 1\right) \quad \text{and} \quad \beta = \left(1-\tilde{\xi}\right)\left(\frac{\tilde{\xi}\left(1-\tilde{\xi}\right)}{\widetilde{\xi''^2}} - 1\right). \tag{5.3}$$

In the calculations of α and β, cutoff values of 10^{-5} and 10^{-8} are used for $\tilde{\xi}$ and $\widetilde{\xi''^2}$, respectively. Below these cut-off values, the PDF tends to a delta function close to $\eta = 0$ or $\eta = 1$ and no turbulent mixing takes place. Separate routines are implemented to calculate I_1, I_2, and the temporal derivatives of I_1 and $\tilde{\xi}$. These terms are used within the CFX solver to calculate the product of the PDF and the conditional scalar dissipation rate, $\tilde{P}(\eta)\langle\chi|\eta\rangle$, at every location in the domain. All computations are performed in double precision. The integrations performed in the routines for I_1 and I_2 utilize the adaptive quadrative routines of QUADPACK [58], and use a 1000 point grid in mixture fraction space. To avoid problems of numerical error the integrations for I_1 and I_2 are performed between 0 and η for values of η less than $\tilde{\xi}$, and between η and 1 for values of η greater than or equal to $\tilde{\xi}$, as suggested by Devaud et al.[21]. Using the appropriate boundary conditions for I_1 and I_2

$$\widetilde{I}_1(0) = \tilde{\xi}, \quad \tilde{I}_1(1) = 0, \quad \widetilde{I}_2(0) = \widetilde{\xi''^2} \quad \text{and} \quad \tilde{I}_2(1) = 0 \tag{5.4}$$

I_1 and I_2 are now calculated following Equations 5.5-5.8.

$$\widetilde{I}_1(\eta) = \tilde{\xi} - \eta - \int_0^\eta \left(\eta^0 - \eta\right)\tilde{P}(\eta^0)d\eta^0 \qquad \text{for } \eta < \tilde{\xi}, \tag{5.5}$$

$$\widetilde{I}_1(\eta) = \int_{\eta}^{1} \left(\eta^0 - \eta\right) \tilde{P}(\eta^0) d\eta^0 \quad \text{for } \eta \geq \tilde{\xi}, \tag{5.6}$$

$$\widetilde{I}_2(\eta) = \widetilde{\xi''^2} - \int_{0}^{\eta} \left(\eta^0 - \eta\right) \left(\eta^0 - \tilde{\xi}\right) \tilde{P}(\eta^0) d\eta^0 \quad \text{for } \eta < \tilde{\xi}, \tag{5.7}$$

$$\widetilde{I}_2(\eta) = \int_{\eta}^{1} \left(\eta^0 - \eta\right) \left(\eta^0 - \tilde{\xi}\right) \tilde{P}(\eta^0) d\eta^0 \quad \text{for } \eta \geq \tilde{\xi}. \tag{5.8}$$

The inhomogeneous model can potentially give negative values for the conditional scalar dissipation rate in very low probability regions. Values of $\langle\chi|\eta\rangle$ below zero are not physical, and may arise due to the fact that the linear conditional velocity model is not a good approximation for η values far from the mean mixture fraction, $\tilde{\xi}$ [21], or that the gradient model gives excessively high magnitudes of the conditional velocity in low probability regions [24]. Negative values that are calculated for $\tilde{P}(\eta)\langle\chi|\eta\rangle$ are set equal to zero in the flow field calculations.

5.7 Cross-stream Averaged Solution

Due to the weak dependence of conditional averages of scalars on the radial coordinate in self similar shear flows, cross-stream averaging is employed to greatly reduce the computational expense of solving the CMC equations [12, 41]. Klimenko [17] suggests that the radial dependence of the PDF should be assumed to be greater than that of the conditional mean concentrations. To account for this dependence the PDF-weighted axial component of the CMC equations is integrated in the radial direction. This simplification, referred to as the shear flow approximation, is discussed further in Section 3.5. This procedure allows for the CMC equations to be greatly simplified, reducing the dimensionality of the problem. For a given scalar, ψ(x,r,t), in an axisymmetric flow the PDF-weighted cross-stream average is defined as

$$\psi_{R^+}(x,t) = \frac{\int_0^R \psi(x,r,t)\tilde{P}(x,r,t,\eta) r dr}{\int_0^R \tilde{P}(x,r,t,\eta) r dr}, \tag{5.9}$$

where $\tilde{P}(x,r,t,\eta)$ is the Favre-averaged PDF and R is a cutoff radius larger than the width of the region of mixing. For each axial location flow field data is exported into data

libraries to be read in by the cross-stream averaging code. The cut-off radius, R, is set to be the radial position at which the Favre-averaged mixture fraction, $\tilde{\xi}$, drops below 10^{-3}. More stringent cut-off values were tested, and yielded negligible changes. A FORTRAN routine is used to determine the cross-stream averages for quantities that are output from the flow field solution, on an equally spaced axial grid of 29 points. To reduce error in numerical integration of Equation 5.9, the radial profiles from the flow field solution are linearly interpolated onto a 500 point radial grid. The cross-stream averaging routine uses trapezoidal numerical integration and outputs the necessary cross-stream averaged conditional quantities into libraries that are used in the solution of the CMC equations.

Applying Equation 5.9 to the conditional species transport equation, and considering the shear flow approximation, which allows conditional average of scalars to be moved outside the integral due to their weak dependence on the radial coordinate, yields the cross-stream averaged equation

$$\frac{\partial Q_\alpha}{\partial t} = -\left[\{\langle u_x|\eta\rangle\}_{R^+} - \left\{\frac{D_t}{\langle\rho\rangle\tilde{P}}\frac{\partial(\langle\rho\rangle\tilde{P})}{\partial x}\right\}_{R^+} - \left\{\frac{\partial D_t}{\partial x}\right\}_{R^+}\right]\frac{\partial Q_\alpha}{\partial x} + \{D_t\}_{R^+}\frac{\partial^2 Q_\alpha}{\partial x^2} + \frac{1}{2}\{\langle\chi|\eta\rangle\}_{R^+}\frac{\partial^2 Q_\alpha}{\partial \eta^2} + \frac{\langle\dot{\omega}_\alpha|\eta\rangle}{\rho_\eta}. \tag{5.10}$$

5.8 Fractional Step Method

In the solution of the CMC equations, the fractional step method (also known as operator splitting) is implemented [59, 60]. In this method a Partial Differential Equation (PDE) is split into two or more simpler, coupled ODEs which are solved in individual steps over sequential fractions of the timestep. The solution of an ODE over one fraction of the timestep provides initial conditions for the ODE in the subsequent timestep. This approach is valid provided the change in variables within the ODE are not large over the timestep. The main advantage in operator splitting lies in being able to treat terms in a complicated ODE differently based upon their nature. For example, stiff terms can be isolated and solved with a solution method that would not be necessary for non-stiff terms.

For the conditional species mass fraction transport equations, the fractional step method is advantageous because it allows for the stiff chemical source term to be treated separately from the other, non-stiff terms in the equation.

$$\frac{\partial Q_\alpha}{\partial t} = \underbrace{-\left[\{\langle u_x|\eta\rangle\}_{R^+} - \left\{\frac{D_t}{\langle\rho\rangle\tilde{P}}\frac{\partial(\langle\rho\rangle\tilde{P})}{\partial x}\right\}_{R^+} - \left\{\frac{\partial D_t}{\partial x}\right\}_{R^+}\right]\frac{\partial Q_\alpha}{\partial x} + \{D_t\}_{R^+}\frac{\partial^2 Q_\alpha}{\partial x^2}}_{\text{Physical transport terms}} \underbrace{+\frac{1}{2}\{\langle\chi|\eta\rangle\}_{R^+}\frac{\partial^2 Q_\alpha}{\partial \eta^2}}_{\text{Micro-mixing term}} \underbrace{+\frac{\langle\dot{\omega}_\alpha|\eta\rangle}{\rho_\eta}}_{\text{Chemical source term}}. \quad (5.11)$$

In the first step of the solution process, the non-stiff physical transport terms are solved using LU-decomposition over the interval [t, t+dt/2]. The physical transport terms deal only with physical space in the x-coordinate. The conditional species mass fractions from the first fractional step are used as the initial conditions for the second. In the second step the stiff chemical source term, as well as the micro-mixing term for convenience, are solved using a stiff ODE solver, VODE [61], over the interval [t,t+dt]. These two terms both deal with only the mixture fraction, or η coordinate. The third step consists of the physical transport terms again being solved over the last half of the timestep, [t+dt/2, t+dt].

5.8.1 Physical transport terms

$$\frac{\partial Q_\alpha}{\partial t} = -\left[\{\langle u_x|\eta\rangle\}_{R^+} - \left\{\frac{D_t}{\langle\rho\rangle\tilde{P}}\frac{\partial(\langle\rho\rangle\tilde{P})}{\partial x}\right\}_{R^+} - \left\{\frac{\partial D_t}{\partial x}\right\}_{R^+}\right]\frac{\partial Q_\alpha}{\partial x} + \{D_t\}_{R^+}\frac{\partial^2 Q_\alpha}{\partial x^2} \quad (5.12)$$

For all internal nodes ($1 \leq i < N_x$, where N_x is the total number of axial positions) first order backward differencing is used for first derivatives, and second order central differencing for second derivatives.

$$\frac{\partial Q_\alpha}{\partial x} = \frac{Q_\alpha|_i - Q_\alpha|_{i-1}}{\Delta x}, \quad (5.13)$$

$$\frac{\partial^2 Q_\alpha}{\partial x^2} = \frac{Q_\alpha|_{i+1} - 2Q_\alpha|_i + Q_\alpha|_{i-1}}{(\Delta x)^2}, \quad (5.14)$$

Substituting the above derivative approximations into Equation 5.12 and making use of the following simplification

$$\Psi|_i^{t+\Delta t} = -\left[\{\langle u_x|\eta\rangle\}_{R^+} - \left\{\frac{D_t}{\langle\rho\rangle\tilde{P}}\frac{\partial(\langle\rho\rangle\tilde{P})}{\partial x}\right\}_{R^+} - \left\{\frac{\partial D_t}{\partial x}\right\}_{R^+}\right], \quad (5.15)$$

yields

$$\frac{\partial Q_\alpha}{\partial t} = \Psi|_i^{t+\Delta t}\left[\frac{Q_\alpha|_i - Q_\alpha|_{i-1}}{\Delta x}\right] + \{D_t\}_{R^+}\left[\frac{Q_\alpha|_{i+1} - 2Q_\alpha|_i + Q_\alpha|_{i-1}}{(\Delta x)^2}\right]. \tag{5.16}$$

Integration of Equation 5.16 with respect to time and use of the fully implicit scheme at node i leads to

$$\begin{aligned} Q_\alpha|_i^{t+\Delta t} - Q_\alpha|_i^t = \Psi|_i^{t+\Delta t}\left[\frac{Q_\alpha|_i^{t+\Delta t} - Q_\alpha|_{i-1}^{t+\Delta t}}{\Delta x}\right]\Delta t \\ +\{D_t\}_{R^+}\left[\frac{Q_\alpha|_{i+1}^{t+\Delta t} - 2Q_\alpha|_i^{t+\Delta t} + Q_\alpha|_{i-1}^{t+\Delta t}}{(\Delta x)^2}\right]\Delta t. \end{aligned} \tag{5.17}$$

To simplify Equation 5.17, it can be rewritten

$$Q_\alpha|_{i,j}^t = AQ_\alpha|_{i-1}^{t+\Delta t} + BQ_\alpha|_i^{t+\Delta t} + CQ_\alpha|_{i+1}^{t+\Delta t} \tag{5.18}$$

where

$$A = \left[\frac{\Psi|_i^{t+\Delta t}}{\Delta x} - \frac{\{D_t\}_{R^+}}{(\Delta x)^2}\right]\Delta t, \tag{5.19}$$

$$B = \left[1 - \frac{\Psi|_i^{t+\Delta t}}{\Delta x} + \frac{2\{D_t\}_{R^+}}{(\Delta x)^2}\right]\Delta t, \tag{5.20}$$

$$C = \left[-\frac{\{D_t\}_{R^+}}{(\Delta x)^2}\right]\Delta t, \tag{5.21}$$

This discretized equation and its corresponding coefficients apply at all interior axial nodes ($1 < i < N_x$). At the furthest axial node in the 1-D grid ($i = N_x$) first order backwards differencing is used for both first and second derivatives.

$$\frac{\partial^2 Q_\alpha}{\partial x^2} = \frac{Q_\alpha|_i^{t+\Delta t} - 2Q_\alpha|_{i-1}^{t+\Delta t} + Q_\alpha|_{i-2}^{t+\Delta t}}{(\Delta x)^2}, \tag{5.22}$$

In a manner similar to that for the internal nodes, the substitution of the above derivative approximation into Equation 5.12, with subsequent simplification, yields

$$Q_\alpha|_{i,j}^t = AQ_\alpha|_{i-1}^{t+\Delta t} + BQ_\alpha|_i^{t+\Delta t} + CQ_\alpha|_{i-2}^{t+\Delta t}, \tag{5.23}$$

in which

$$A = \left[\frac{\Psi|_i^{t+\Delta t}}{\Delta x} - \frac{2\{D_t\}_{R^+}}{(\Delta x)^2} \right] \Delta t, \tag{5.24}$$

$$B = \left[1 - \frac{\Psi|_i^{t+\Delta t}}{\Delta x} - \frac{\{D_t\}_{R^+}}{(\Delta x)^2} \right] \Delta t, \tag{5.25}$$

$$C = \left[-\frac{\{D_t\}_{R^+}}{(\Delta x)^2} \right] \Delta t. \tag{5.26}$$

The composition at the first axial node ($Q_\alpha|_{i=1}$), which corresponds to the injector inlet, is known at all times. Using Equations 5.18 and 5.22, the system of equations can be represented by the following matrix.

$$\begin{bmatrix} 1 & 0 & 0 & 0 & \cdots & 0 & 0 & 0 \\ A_2 & B_2 & C_2 & 0 & \cdots & 0 & 0 & 0 \\ 0 & A_3 & B_3 & C_3 & \cdots & 0 & 0 & 0 \\ \vdots & & \vdots & & \ddots & \vdots & & \vdots \\ 0 & 0 & 0 & 0 & \cdots & A_{N_x-1} & B_{N_x-1} & C_{N_x-1} \\ 0 & 0 & 0 & 0 & \cdots & A_{N_x} & B_{N_x} & C_{N_x} \end{bmatrix} \times \begin{bmatrix} Q_\alpha|_1^{t+\Delta t} \\ Q_\alpha|_2^{t+\Delta t} \\ Q_\alpha|_3^{t+\Delta t} \\ \vdots \\ Q_\alpha|_{N_x-1}^{t+\Delta t} \\ Q_\alpha|_{N_x}^{t+\Delta t} \end{bmatrix} = \begin{bmatrix} Q_\alpha|_1^{t} \\ Q_\alpha|_2^{t} \\ Q_\alpha|_3^{t} \\ \vdots \\ Q_\alpha|_{N_x-1}^{t} \\ Q_\alpha|_{N_x}^{t} \end{bmatrix}$$

This system of equations is solved using the LU-decomposition method. The solution is implemented with two FORTRAN routines - LUDCMP and LUBKSB [59]. The routine LUDCMP performs the LU-decomposition using Crout's algorithm and implicit pivoting [59]. This is used in conjunction with LUBKSB, which performs the required forward and back substitutions, to obtain the solution to the equation set.

5.8.2 Chemical source and micromixing terms

The stiff chemical source term, along with the micromixing term, are solved in the second fractional step, with the solutions from the previous fractional step (solving the physical transport terms) used as initial conditions.

$$\frac{\partial Q_\alpha}{\partial t} = \frac{1}{2}\{\langle \chi|\eta \rangle\}_{R^+} \frac{\partial^2 Q_\alpha}{\partial \eta^2} + \frac{\langle \dot{\omega}_\alpha|\eta \rangle}{\rho_\eta}. \tag{5.27}$$

Equation 5.27 is solved using the double precision version of the ODE solver VODE [61] at each axial position. VODE is a variable step ODE solver that utilizes variable coefficient Backwards Differentiation Formula (BDF) methods for solving stiff systems [62]. The user interface allows input for the overall time step, absolute and relative solution tolerances, and maximum number of internal time steps used. For this study the overall time step implemented is 50 μs, which corresponds to the interval between exported data libraries from the flow field calculations, along with a maximum of 1500 internal time steps. The relative tolerance used is 10^{-5}, the absolute tolerance is 10^{-20}. Further details of the VODE solver can be found in references [61] and [62].

5.9 Linear Coupling of Enthalpy and Mixture Fraction

For the conditions being examined in this study, enthalpy is conserved. This is because radiation is negligible prior to ignition, as soot and flames are both absent in the shock tube. In previous work, El Sayed and Devaud [26] showed that the pressure fluctuations, and hence the pressure work, was also negligible. With these terms removed, the enthalpy transport equation takes the form

$$\frac{\partial(\rho h)}{\partial t} + \frac{\partial(\rho u_i h)}{\partial x_i} = \frac{\partial}{\partial x_i}\left(\rho D_\alpha \frac{\partial h}{\partial x_i}\right). \tag{5.28}$$

Equation 5.28 is of identical form to the transport equation for mixture fraction,

$$\frac{\partial(\rho \xi)}{\partial t} + \frac{\partial(\rho u_i \xi)}{\partial x_i} = \frac{\partial}{\partial x_i}\left(\rho D_\alpha \frac{\partial \xi}{\partial x_i}\right), \tag{5.29}$$

and is therefore also a conserved scalar. With this simplified enthalpy equation, the enthalpy can be related to the mixture fraction by the linear coupling relation

$$h = h_2 + \xi(h_1 - h_2). \tag{5.30}$$

in with h_1 is the enthalpy of the fuel, and h_2 is the enthalpy of the air. Conditionally averaging this expression with respect to η yields a linear relation for determining the conditional enthalpy

$$Q_h = \langle h_2|\eta\rangle + \eta(\langle h_1|\eta\rangle - \langle h_2|\eta\rangle). \tag{5.31}$$

The conditional temperature, Q_T, can be calculated either from its transport equation, or from Q_h. However, Q_T is not a linear function of Q_h due to the temperature dependence of C_p. In this study iterative linear interpolation is used to calculate Q_T from Q_h. This approach is advantageous in that is saves computational expense when compared with solving the transport equation for conditional temperature. In previous work, El Sayed and Devaud [26], solved for Q_T using linear interpolation and through the transport equations, and found the differences to be negligible.

5.10 Chemical Kinetics

The chemical kinetics package CHEMKIN II [63], developed by Sandia National laboratories for gas-phase reacting flows, is used in this study. This FORTRAN package is used to compute reaction rates, and important thermodynamic quantities such as specific heats. The CHEMKIN package consists of five components, two of which are user-supplied files and must correspond to the format required by CHEMKIN. The chemical kinetics mechanism, specific to the combustion application of the individual study, is provided by the user along with a database of thermodynamic data for the species involved in the mechanism. The CHEMKIN Interpreter is a piece of code that reads in the chemical mechanism and takes the relevant thermodynamic data from the thermodynamic data library. The output of the Interpreter is called the Linking File. This file contains all important information regarding elements, species and reactions in the chemical kinetics mechanism. The Linking File is initialized to create three data arrays that are used within subroutines in the final part of the package, the Gas-Phase Subroutine Library. This Library contains subroutines that are used to calculate chemical reaction rates, thermodynamic properties, and all relevant quantities concerning the species and reactions involved in the mechanism. In the context of this study, these subroutines return the required species production rates in the solution of the CMC equations.

5.10.1 Chemical kinetics mechanism

The chemical kinetics mechanism UBC Mech 1.0 [64] is used in this study. This methane oxidation mechanism consists of 38 species, 192 reactions, and is optimized for methane combustion at pressure above 16 atmospheres and temperatures between 1000 K and 1350 K. The conditions in which the mechanism is intended match the autoignition problem of this study. UBC Mech 1.0 is based upon the modified GRI-mech 2.1 mechanism of Petersen et al. [65], but contains six additional species and utilizes different thermodynamic data. Performance of the mechanism was evaluated against experimental ignition delay data for methane autoignition in a shock tube for a range of pressures up to 40 atmospheres and showed very good agreement [64].

5.11 Summary

The computational nethodology employed in this study was presented in this chapter. The flow field simulations and the implementation of cross-stream averaging were described. The well known deficiencies of the k-ε model for free shear flows was addressed, and the penetration length of the flow field solution was examined. The accuracy of using one air temperature flow field for all five air temperatures was addressed. The overall behaviour of the jet development remained the same, but small differences in penetration were noted. The fractional step approach to solving the cross-stream averaged CMC equations was outlined, and the linear coupling of mixture fraction and enthalpy was explained. Chemical kinetics mechanism UBC Mech 1.0 was described and its implementation through CHEMKIN II was summarized. In the next chapter the performance of the two formulations of the inhomogeneous mixing model, and their relevant closures for conditional velocity, are assessed. Autoignition results are presented and compared with previous results and experimental data.

Chapter 6

Inhomogeneous Model Results

In this section the results from the inhomogeneous mixing model, with the linear and gradient models for conditional velocity, are presented and compared. In addition to the cross-stream averaged quantities of interest, profiles of conditional velocity, conditional scalar dissipation rate, and equation budgets at specific points in physical space are also examined. Autoignition predictions from the two formulations of the inhomogeneous model are compared with results using homogeneous mixing models [44] and experimental data [5].

6.1 Physical Locations for Analysis

Two axial locations and times are selected that represent two important areas of the jet. The first, at a distance of 0.5 cm from the injector 0.3 ms after injection, illustrates the mixing field close to the injector at an early stage of mixing. The second, at a distance of 2 cm from the injector 0.7 ms after injection, roughly corresponds to the location and time of ignition at $T_{air} = 1337$ K for the two implementations of the inhomogeneous model. At both axial locations three radial positions are examined. These three points correspond to the jet centreline, a point approximately halfway to the edge of the jet, and a point near the edge of the jet where the mean mixture fraction is near the most reactive mixture. Figure 6.1 shows the six points in physical space that are examined along with contours of the mean mixture fraction at 0.3 ms and 0.7 ms respectively.

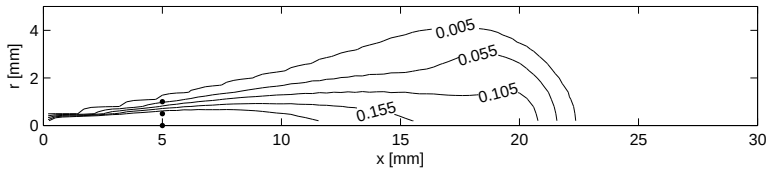

(a) t = 0.3 ms

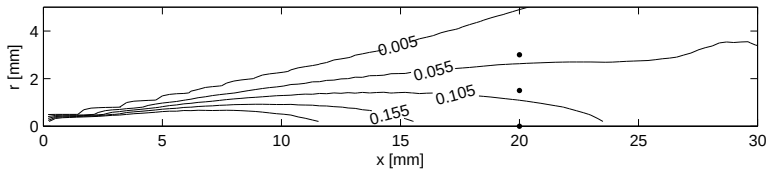

(b) t = 0.7 ms

Figure 6.1: Physical locations for results comparison with mean mixture fraction contours.

6.2 Conditional Velocity

6.2.1 Conditional velocities without cross-stream averaging

The axial and radial conditional velocity behaviour of the linear and gradient conditional velocity models provide some insight into the applicability of the models and their influence on the conditional scalar dissipation rate. Figure 6.2 presents the axial and radial conditional velocities at x = 5 mm and t = 0.3 ms. At all three radial positions, the conditional velocities from the gradient model differ considerably from the linear model for some values of η. Along the centreline, in Figure 6.2 (a), the gradient and linear models yield similar results for the axial conditional velocity between η values of 0.2 and 0.6. This region corresponds to roughly three to four standard deviations about the mean mixture fraction. Below $\eta = 0.2$ and above $\eta = 0.6$ the gradient model yields sharply increasing values which depart significantly from the linear relationship. Similar behaviour is observed at a radial position of r = 0.5 mm, shown in Figure 6.2 (c). The gradient and linear models correspond closely between η values of 0.1 and 0.5, but the gradient model shows increasing divergent behaviour on both the lean and rich side of that range. In contrast, near the edge of the jet, in Figure 6.2 (e), the two conditional velocity models are in close agreement for the entire lean region. The gradient model only diverges from the linear relationship near $\eta = 0.7$, where the axial velocity approaches large negative values. To explain this behaviour it is useful to examine the plots of the PDF at each of these three

locations, shown in Figures 6.5 (b), (d), and (f) respectively. The regions in which the gradient model's conditional axial velocity diverges from the linear relationship corresponds to regions of very low probability. This causes the gradient conditional velocity model to yield large positive and negative values in areas in which the PDF approaches zero. The unphysical behaviour of the gradient model utilizing a β-PDF in low probability regions was also noticed by Mortensen and de Bruyn Kops [24]. Similar trends in the conditional velocity have also been noted by Sawford [66] using the Interaction by Exchange with the Conditional Mean (IECM) model to examine a scalar mixing layer in a Lagrangian framework, and Brethouwer and Nieuwstadt [67] using DNS to investigate conditional statistics in a turbulent channel flow.

The radial conditional velocities show similar behaviour, as shown in Figures 6.2 (b) (d) and (f). However, for the centreline the gradient model is in agreement with the linear model for a much larger range of η values. It is only below $\eta = 0.1$ that the gradient model diverges from the linear relationship, although the magnitude of the velocity remains small. Similarly in Figure 6.2 (d), for a radial position of 0.5 mm, the gradient model matches the linear behaviour closely for the range of η values from 0.1 to 1. Below 0.1 the gradient radial conditional velocity also diverges to very large negative velocities. Near the edge the jet the radial conditional velocity exhibits similar behaviour to the axial conditional velocity, with the exception of the gradient model diverging to very large positive values above $\eta = 0.7$ for the radial velocity as opposed to the negative values observed in the axial direction.

The conditional velocities further downstream at x = 20 mm and t = 0.7 ms, in Figure 6.3 show similar behaviour. Figure 6.3 (a) shows the axial conditional velocities on the centreline, and the gradient and linear models correspond closely from $\eta = 0$ to $\eta = 0.3$. For values of η above 0.3 the gradient model diverges to much higher values than the linear model. The behaviour at r = 1.5 mm is very similar to the centreline, as shown in Figure 6.3 (c). For η values from 0 to roughly 0.2 the gradient and linear models are in reasonable agreement, although there is a small sharp increase in values for the gradient model very close to $\eta = 0$. Above $\eta = 0.2$ the gradient model diverges to very large positive velocities. Near the edge of the jet, in Figure 6.3 (e) the trend is the same, however the range over which the gradient and linear models agree is considerably smaller. The gradient model axial velocity shows approximately linear behaviour from $\eta \simeq 0.05$ to approximately $\eta = 0.1$, after which it yields continually increasing values, as opposed to decreasing values from

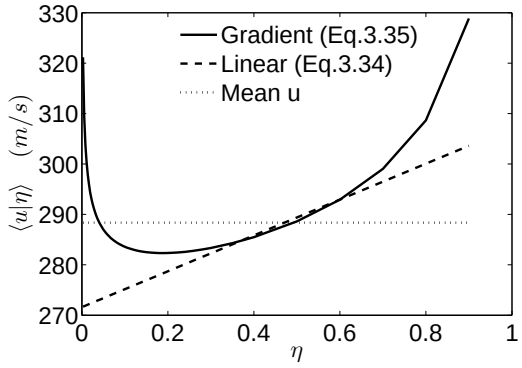

(a) r = 0 mm

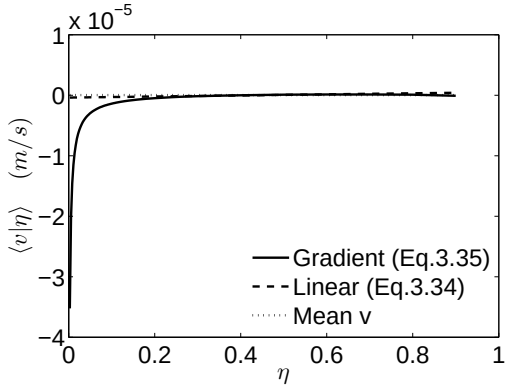

(b) r = 0 mm

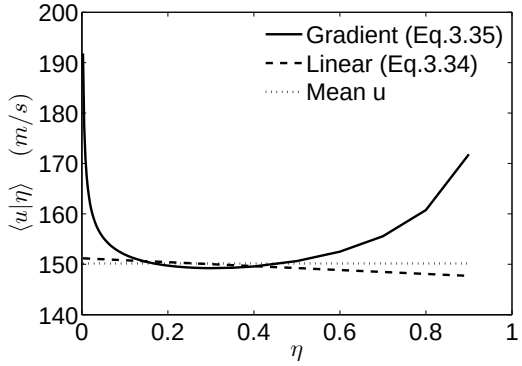

(c) r = 0.5 mm

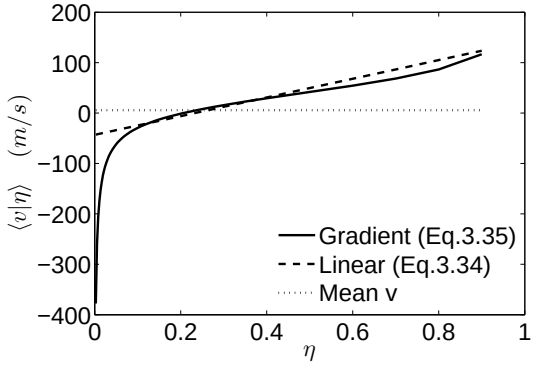

(d) r = 0.5 mm

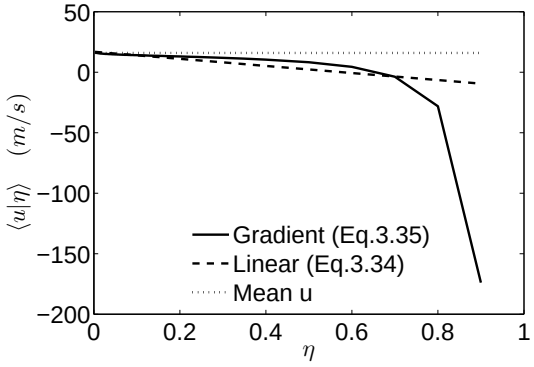

(e) r = 1 mm

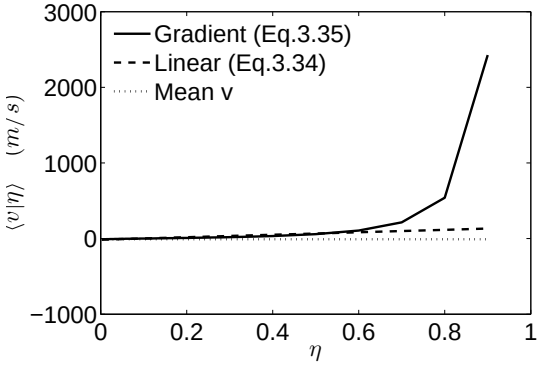

(f) r = 1 mm

Figure 6.2: Axial (left) and radial (right) conditional velocity profiles at x = 5 mm, t = 0.3 ms.

the linear model. Examining the PDF profiles at these three points, in Figures 6.6 (b), (d), and (f) respectively, it can be seen that the range of η values over which the two conditional velocity models are in reasonable agreement roughly corresponds to the width of the non-zero part of PDF. For the centreline and r = 1.5 mm, after the corresponding PDF approaches zero, at approximately $\eta = 0.25$ and $\eta = 0.2$ respectively, the gradient axial conditional velocities diverge to very large values for richer mixtures. Near the edge of the jet the range of agreement between the two models is even smaller, which corresponds to the very narrow PDF observed in Figure 6.6 (f), which approaches zero at approximately $\eta = 0.15$.

The radial conditional velocities at x = 20 mm and t = 0.7 ms exhibit very similar behaviour. Along the centreline and at r = 1.5 mm, in Figure 6.3 (b) and (d), the gradient radial conditional velocity diverges from the linear relationship for η values above roughly 0.2, which is similar to the axial velocity behaviour, with the exception of divergence to large negative instead of positive values. For rich mixtures the gradient model yields rapidly decreasing values for the velocity, in sharp contrast to the increasing values from the linear model. Near the edge of the jet, in Figure 6.3 (e), the gradient model yields significantly different conditional radial velocities for η values greater than 0.1, but without diverging behaviour. The gradient profile is nearly linear, but with a significantly lower slope than that of the linear model. These rich regions in which the gradient model shows a clear departure from the linear model correspond to areas in which the PDF approaches zero, as shown in Figures 6.6 (b), (d), and (f). Along the centreline the overall magnitude of the radial conditional velocity from the gradient model remains small, but the divergence from linear behaviour is still significant as radial velocity along the centreline in an axisymmetric system should remain at zero. At r = 1.5 mm, the divergence of the gradient model for very lean mixtures also produces large negative velocities. The diverging behaviour close to $\eta = 0$ corresponds to regions in which the PDFs are also close to zero. While the low values of PDF in these lean regions did not cause the axial velocity to diverge, the impact is more noticeable with the radial conditional velocity. Near the edge of the jet the gradient radial velocity yields values similar to the linear model for only a short range of η values up to approximately 0.1. After 0.1 the gradient model shows somewhat linear behaviour rather than divergence to ∞ or $-\infty$, but with a very different slope than that of the linear model.

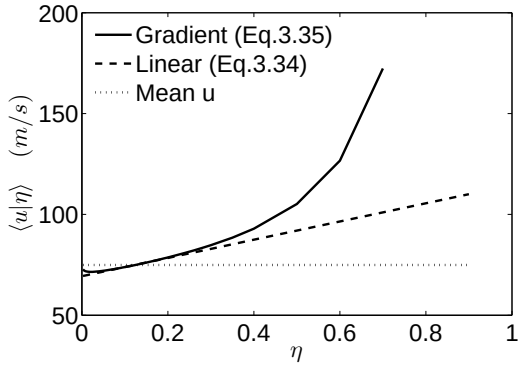

(a) r = 0 mm

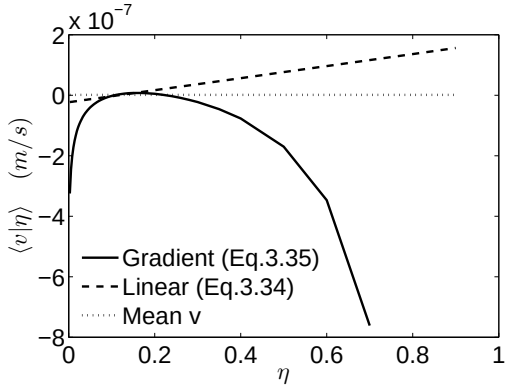

(b) r = 0 mm

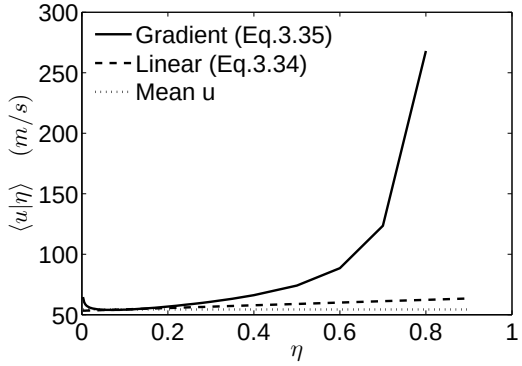

(c) r = 1.5 mm

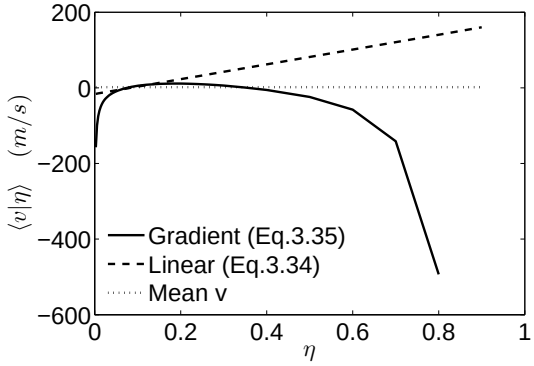

(d) r = 1.5 mm

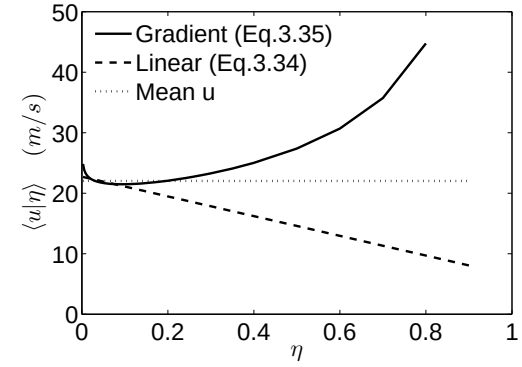

(e) r = 3 mm

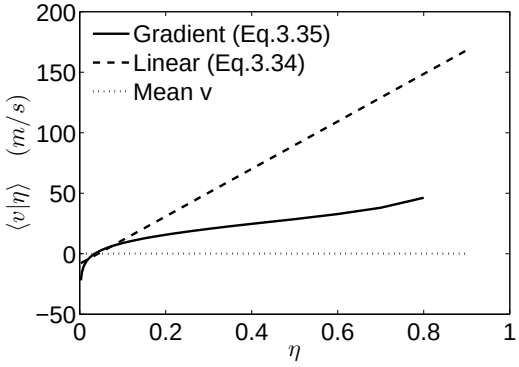

(f) r = 3 mm

Figure 6.3: Axial (left) and radial (right) conditional velocity profiles at x = 20 mm, t = 0.7 ms.

6.2.2 Cross-stream averaged conditional velocities

The axial and radial conditional velocities appear in the mixing model expressions, Equations 4.17 and 4.17, and have a direct impact on the values of $\langle \chi | \eta \rangle$ that are obtained. The conditional velocity also appears in the CMC equations, but since the cross-stream averaged form of these equations are being solved, only the cross-stream averaged axial conditional velocity is considered in the CMC equations. Therefore the radial conditional velocities will only have an impact on the conditional scalar dissipation rate. The cross-stream averaged axial conditional velocities are shown in Figure 6.4. For x = 5 mm and t = 0.3 ms the cross-stream averaging yields profiles for the gradient and linear models that are very similar. From $\eta = 0$ to $\eta = 0.6$ the curves are nearly identical, and above $\eta = 0.6$ the gradient model produces slightly higher velocities. In the area of interest, for lean values around the stoichiometric mixture fraction of 0.055, the cross-stream averaged axial velocities are in good agreement. Further downstream at a later time, at x = 20 mm and t = 0.7 ms, shown in Figure 6.4 (b), the gradient and linear models show close agreement for the interval $\eta = 0$ to $\eta = 0.2$. Above $\eta = 0.2$ the gradient model shows very different behaviour than the linear model, decreasing slightly before increasing sharply to a peak at $\eta = 0.8$. The discrepancy with the cross-stream averaged velocities after $\eta = 0.2$ corresponds to the divergence seen in Figure 6.3, and is related to the PDF quickly approaching zero near $\eta = 0.2$ for each of the three points examined in the width of the jet. Due to the fact that the gradient and linear cross-stream averaged conditional velocity profiles are so similar in the region of interest for autoignition (around the stoichiometric mixture fraction and the most reactive mixture), this shows that the impact of the two conditional velocity models will be the greatest through their influence on the conditional scalar dissipation rate that is obtained through the mixing model.

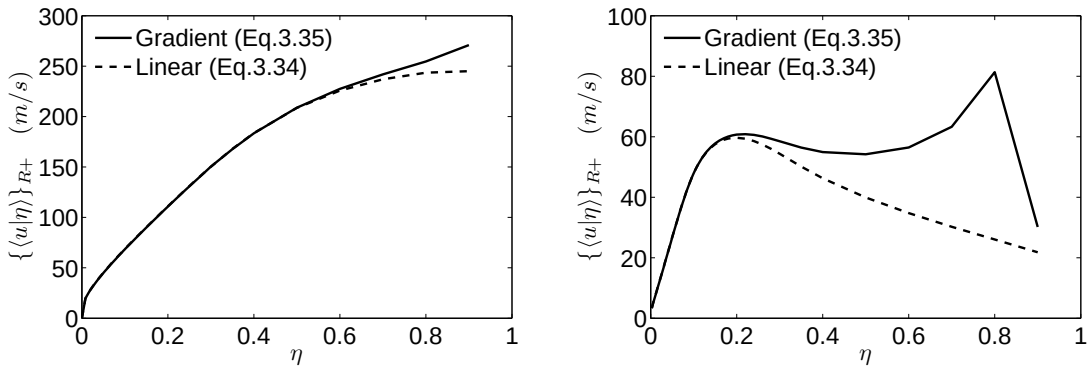

(a) x = 5 mm and t = 0.3 ms

(b) x = 20 mm and t = 0.7 ms

Figure 6.4: Cross-stream averaged axial conditional velocity.

6.3 Conditional Scalar Dissipation Rate

6.3.1 Conditional scalar dissipation rate without cross-stream averaging

The resulting conditional scalar dissipation rates from the inhomogeneous mixing model, using both the gradient and linear conditional velocity models are examined and compared at the physical locations shown in Figure 6.1. For x = 5 mm and t = 0.3 ms, the profiles of the conditional scalar dissipation rate-PDF product are shown on the left of Figure 6.5, while the PDF profiles are shown on the right. The difference between the Inhomogeneous-Gradient and Inhomogeneous-Linear results are greatest along the centreline, shown in Figure 6.5 (a). The peak value of approximately 55000 s^{-1} for $\langle\chi|\eta\rangle\widetilde{P}(\eta)$ from the Inhomogeneous-Gradient model is nearly an order of magnitude greater than the peak observed for the Inhomogeneous-Linear model. The Inhomogeneous-Gradient model also exhibits an extensive plateau at the peak value along the centreline, which starts at very lean values of η and continues past $\eta = 0.2$. The plateau region corresponds to η values in which the PDF, shown in Figure 6.5 (b), is approaching zero. Over the range of $\eta = 0$ to $\eta = 0.7$, the Inhomogeneous-Gradient model yields far higher values for $\langle\chi|\eta\rangle\widetilde{P}(\eta)$, until both models approach zero for very rich mixtures. At a radial position of r = 0.5 mm, shown in Figure 6.5 (c), the Inhomogeneous-Gradient model also yields much higher

$\langle\chi|\eta\rangle\widetilde{P}(\eta)$ values than the Inhomogeneous-Linear model, but the large plateau region at the peak value is no longer present. A small plateau at a value of approximately 12000 s^{-1} is noticeable at η values near zero, but this is considerably lower than the peak value and spans a much smaller interval of η than the plateau on the centreline. The small plateau region is also over values of η in which the PDF approaches zero, as illustrated in Figure 6.5 (d). At η values above 0.05, the Inhomogeneous-Gradient model yields similar trends to the Inhomogeneous-Linear model, but with considerably higher values. Near the edge of the jet, presented in Figure 6.5 (e), the Inhomogeneous-Gradient model results correspond closely to those from the Inhomogeneous-Linear model. This progression shows that the difference in the $\langle\chi|\eta\rangle\widetilde{P}(\eta)$ profiles between the two models is greatest at the core of the jet, and diminishes toward the edge of the mixing layer. In all cases, the linear $\langle\chi|\eta\rangle\tilde{P}(\eta)$ values always tend to 0 towards to the two bounds of mixture fraction space, i.e at η=0 and η= 1, and the location of the peak in mixture fraction closely follows the location of the PDF peak, consistent with the expected behaviour [12].

Further downstream and later in the mixing process, similar behaviour in the profiles of $\langle\chi|\eta\rangle\widetilde{P}(\eta)$ are observed. Figure 6.6 shows the profiles of $\langle\chi|\eta\rangle\widetilde{P}(\eta)$ on the left, and the PDF on the right, at x = 20 mm and t = 0.7 ms. Along the centreline, in Figure 6.6 (a), the peak value from the Inhomogeneous-Gradient model is well over an order of magnitude larger than the peak from the Inhomogeneous-Linear model. Once again, the Inhomogeneous-Linear model exhibits the general behavioural trend (similar to that of the PDF) that is expected for the $\langle\chi|\eta\rangle\widetilde{P}(\eta)$ profile, while the Inhomogeneous-Gradient model has a large plateau region at its peak value that spans from $\eta = 0$ to $\eta = 0.1$. As before, the plateau region of $\langle\chi|\eta\rangle\widetilde{P}(\eta)$ matches the lean mixture η values at which the PDF is approaching zero. At a radial position of r = 1.5 mm, in Figure 6.6 (c), the plateau region for the Inhomogeneous-Gradient model extends over a smaller range of η near $\eta = 0$, and is at a value lower than the peak. In a manner similar to that observed in the upstream behaviour in Figure 6.5 (c), the Inhomogeneous-Gradient profile exhibits a similar general trend to the Inhomogeneous-Linear profile after the plateau region, but with significantly higher values. Close to the edge of the jet the two profiles become close in shape and magnitude, as shown in Figure 6.6 (e). The peak of the Inhomogeneous-Gradient model is still higher than the peak from the Inhomogeneous-Linear model, and occurs at a leaner value of η, but the discrepancy between the profiles is significantly less than it is closer

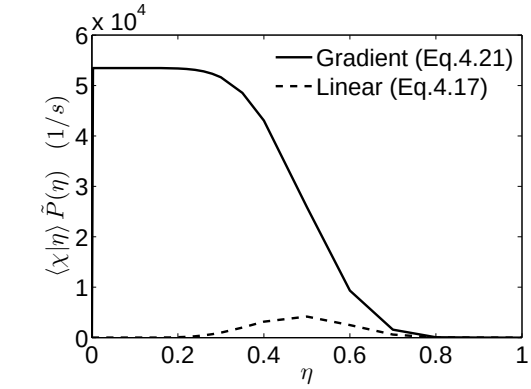

(a) r = 0 mm

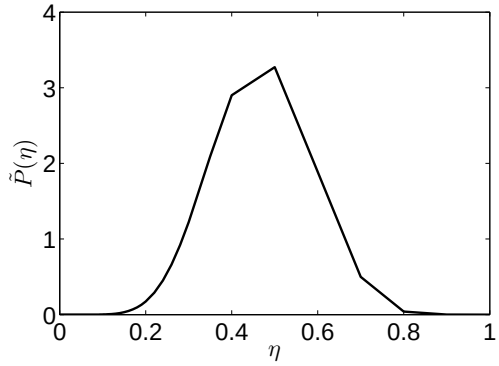

(b) r = 0 mm

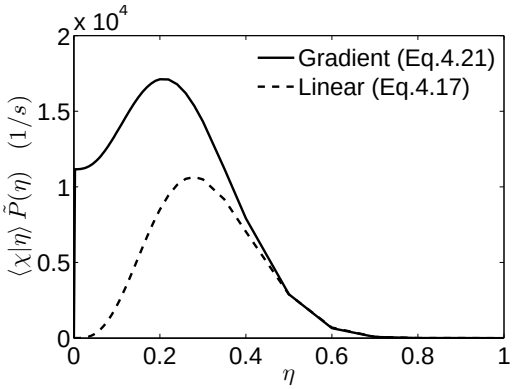

(c) r = 0.5 mm

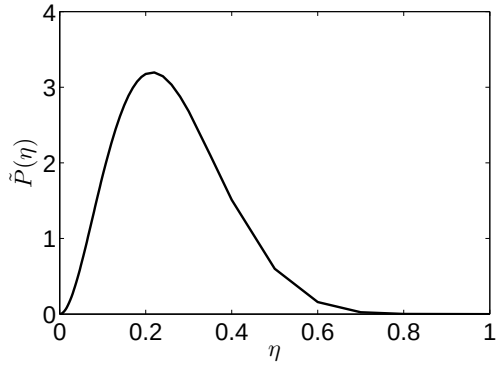

(d) r = 0.5 mm

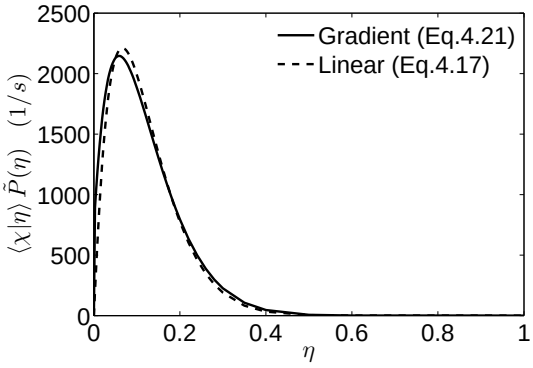

(e) r = 1 mm

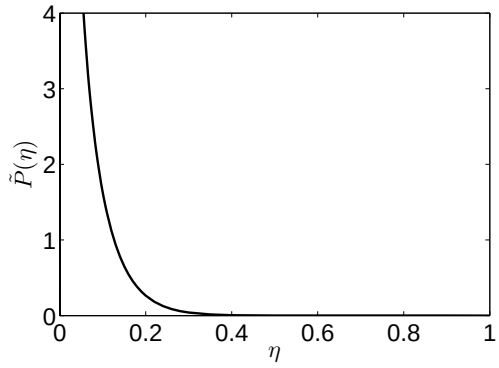

(f) r = 1 mm

Figure 6.5: $\langle\chi|\eta\rangle\tilde{P}(\eta)$ (left) and PDF (right) profiles at x = 5 mm, t = 0.3 ms.

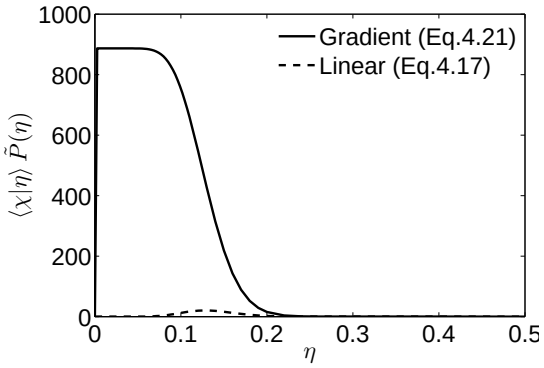

(a) r = 0 mm

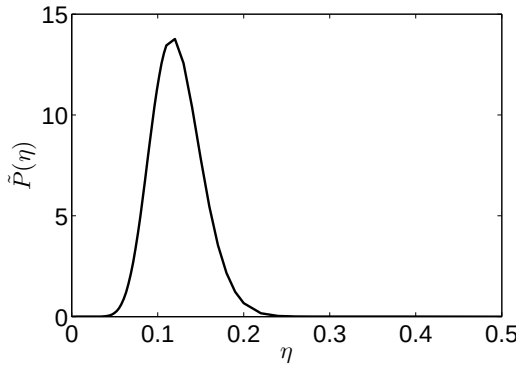

(b) r = 0 mm

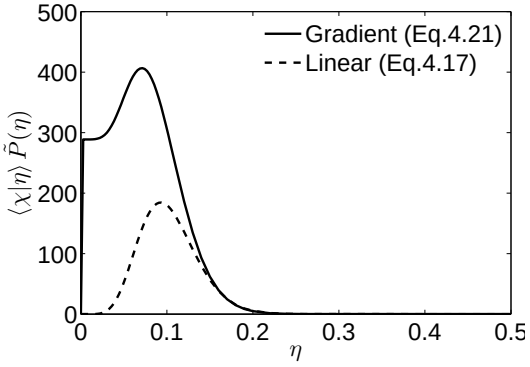

(c) r = 1.5 mm

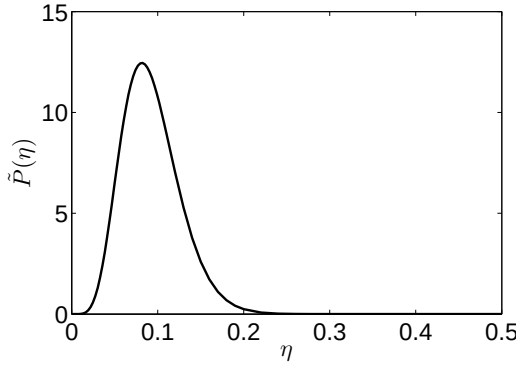

(d) r = 1.5 mm

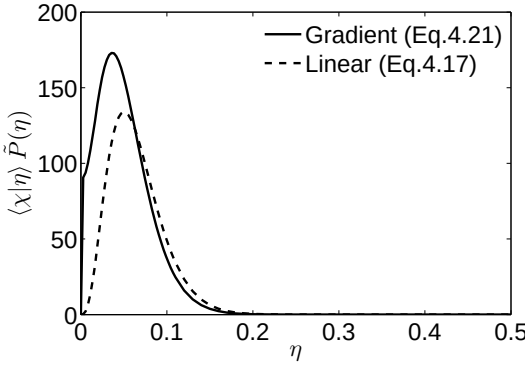

(e) r = 3 mm

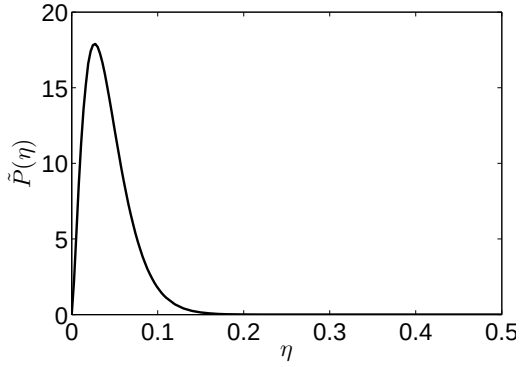

(f) r = 3 mm

Figure 6.6: $\langle\chi|\eta\rangle\tilde{P}(\eta)$ (left) and PDF (right) profiles at x = 20 mm, t = 0.7 ms.

to the centreline. In both axial locations, shown in Figures 6.5 and 6.6, the discrepancy between the two implementations of the inhomogeneous model is noted to decrease as the peak of the PDF moves to leaner mixtures.

The plateau regions being observed in the Inhomogeneous-Gradient profiles of $\langle\chi|\eta\rangle\widetilde{P}(\eta)$ near the centreline of the jet are unphysical and correspond to the divergent behaviour observed in the gradient conditional velocity model at the low-probability regions. This indicates that the numerical issues in the gradient conditional velocity model carry through the inhomogeneous mixing model and cause unphysical behaviour in the profiles of the conditional scalar dissipation rate. As the PDF increases at low η values the two versions of the inhomogeneous model yield similar profiles. Near the edge of the jet the gradient and linear conditional velocity models yield similar predictions in both the axial and radial directions at lean values of η, as shown in Figures 6.2 (e) and 6.3 (e). As a result, the profiles of $\langle\chi|\eta\rangle\widetilde{P}(\eta)$ from the two versions of the inhomogeneous mixing model are very similar at these points. The discrepancy between the conditional velocities at higher η values at the edge of the jet (for η values above 0.6 for x = 5 mm, and for η values above 0.2 for x = 20 mm) do not seem to have much effect on the corresponding profiles of $\langle\chi|\eta\rangle\widetilde{P}(\eta)$.

6.3.2 Plateau Correction

The expected behaviour of the $\langle\chi|\eta\rangle\widetilde{P}(\eta)$ profile is to increase from zero at $\eta = 0$ to a peak value, followed by a decrease to zero with increasing η, similar to the shape of the PDF. The numerical issues at low probability regions in the gradient conditional velocity model yield unphysical values in the profile of $\langle\chi|\eta\rangle\widetilde{P}(\eta)$ from the Inhomogeneous-Gradient model. To assess the degree to which the plateau region affects the autoignition results, the large values in the plateau region are set equal to zero. Since only the values within a lean plateau are considered, this correction will modify the Inhomogeneous-Gradient model profiles near the core of the jet substantially, while leaving the profiles near the edge of the jet, where no plateaus occur, unaltered.

6.3.3 Consistency with the unconditional mean scalar dissipation rate

For consistency with the mean mixture fraction variance transport equation (Equation 2.56) the conditional scalar dissipation rate determined by a mixing model should return the mean Favre-averaged scalar dissipation rate given by the expression

$$\widetilde{\chi} = 2\frac{\widetilde{\varepsilon}}{\widetilde{k}}\widetilde{\xi''^2}. \tag{6.1}$$

This value can be calculated directly in the flow-field solution. The integration of the product of the conditional scalar dissipation rate and the PDF should yield the same value for the mean scalar dissipation rate.

$$\widetilde{\chi}_{integration} = \int_0^1 \langle\chi|\eta\rangle \widetilde{P}(\eta)d\eta. \tag{6.2}$$

In the homogeneous mixing models (AMC and Girimaji's model) the Favre-averaged unconditional scalar dissipation rate is a model input, and by the nature of the models the integration yields the input of mean $\widetilde{\chi}$. The inhomogeneous model, however, does not use $\widetilde{\chi}$ to calculate the $\langle\chi|\eta\rangle$. The scalar dissipation rate profile is calculated at each point using the model equation that is derived through the double-integration of the PDF transport equation. This model equation includes a model for the conditional velocity and a presumed form for the PDF itself.

Figures 6.7 and 6.8 show radial profiles of $\widetilde{\chi}_{integration}$ compared with $\widetilde{\chi}$ at two axial locations for the Inhomogeneous-Linear and Inhomogeneous-Gradient model, respectively. For the Inhomogeneous-Linear model the integrated quantity is considerably lower than $\widetilde{\chi}$ near the centreline, but approaches similar values near the edge of the shear layer. The Inhomogeneous-Gradient model shows much higher values than $\widetilde{\chi}$ in the core of the jet, including a very sharp peak along the centreline, before approaching $\widetilde{\chi}$ near the edge of the jet. Figures 6.7 and 6.8 illustrate that the mean scalar dissipation rate resulting from the inhomogeneous model, with both the linear and gradient conditional velocities models, has significant discrepancies from in the core of the jet. The conditional velocity model used in the mixing model can cause the unconditional conditional scalar dissipation rate that is calculated from Equation 6.2 to differ from the value determined from Equation 6.1. Devaud et al. [21] showed analytically that the Inhomogeneous-Linear model is not fully consistent with the mean mixture fraction variance equation. However, the magnitude of the

discrepancy from $\widetilde{\chi}$ is much higher than anticipated. The Inhomogeneous-Gradient model, however, is expected to be consistent with the Favre-averaged mean scalar dissipation rate. A central reason for using the gradient diffusion conditional velocity model in the implementation of the inhomogeneous mixing model is the fact that it allows for the conditional scalar dissipation rate expression to be consistent with the first and second moment of the mixture fraction [38]. Thus, the same value for $\widetilde{\chi}$ used in the variance equation would be expected to be recovered upon integration of $\langle\chi|\eta\rangle\widetilde{P}(\eta)$. Figure 6.8 shows that the mean value from the Inhomogeneous-Gradient model, particularly along the centreline, exhibit an even larger departure from $\widetilde{\xi}$ than observed with the Inhomogeneous-Linear model. This further illustrates that the diverging behaviour of the gradient diffusion conditional velocity model has a significantly detrimental affect on the corresponding profiles for the conditional scalar dissipation rate.

To correct the discrepancy between $\widetilde{\chi}_{integration}$ and the flow-field calculated $\widetilde{\chi}$, the

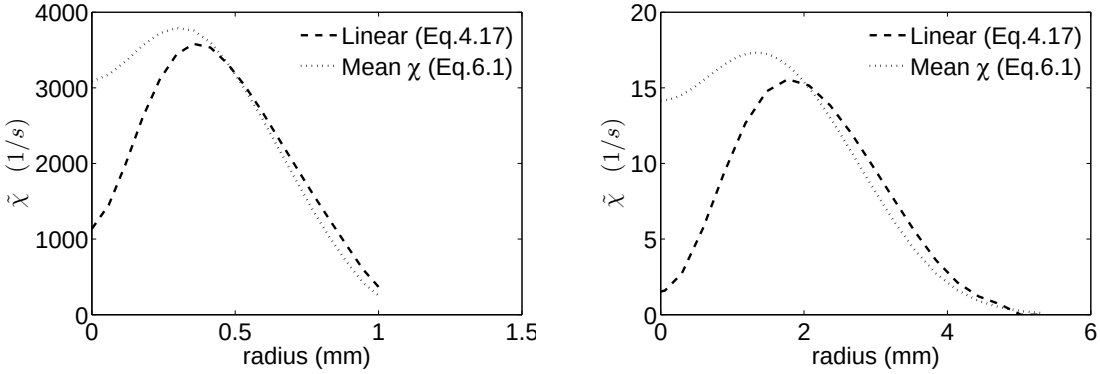

(a) x = 5 mm and t = 0.3 ms

(b) x = 20 mm and t = 0.7 ms

Figure 6.7: Radial profiles of unconditional scalar dissipation rate compared with Equation 6.2 for the Inhomogeneous-Linear model.

conditional scalar dissipation profile, $\langle\chi|\eta\rangle$, can be scaled to yield the desired mean scalar dissipation rate. At each location in the CMC domain, prior to cross-stream averaging, the scalar dissipation rate is modified by the expression

$$\langle\chi|\eta\rangle_{new} = \langle\chi|\eta\rangle_{old}\frac{\widetilde{\chi}}{\widetilde{\chi}_{integration}}. \tag{6.3}$$

This operation scales the conditional scalar dissipation rate profile at a given location by the same ratio for each value of η to yield a mean scalar dissipation rate that corresponds

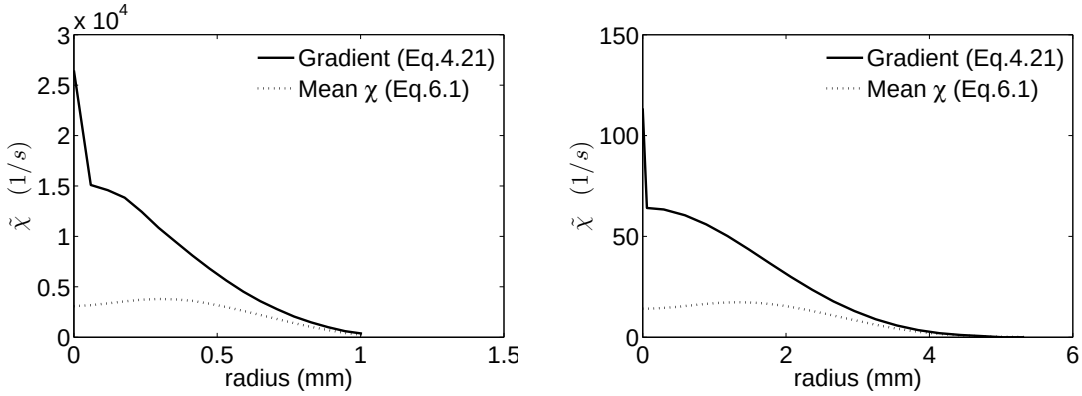

(a) x = 5 mm and t = 0.3 ms

(b) x = 20 mm and t = 0.7 ms

Figure 6.8: Radial profiles of unconditional scalar dissipation rate compared with Equation 6.2 for the Inhomogeneous-Gradient model (not plateau-corrected).

Table 6.1: Peak values of $\langle\chi|\eta\rangle\widetilde{P}(\eta)$ $[s^{-1}]$ at x = 5 mm, t = 0.3 ms

Radius[mm]	Inhom.-Lin.	Inhom.-Lin. scaled	Inhom.-Grad.	Inhom.-Grad. scaled
0	4200	11000	54000	9300
0.5	11000	11000	17000	9100
1	2200	1450	2150	1350

exactly with $\widetilde{\chi}$ calculated from the flowfield. For the Inhomogeneous-Gradient model, this scaling is performed after the plateau correction outlined in the previous section. The scaled and plateau-corrected profiles for the three radial points at x = 5 mm and t = 0.3 ms are presented in Figure 6.9. The corresponding profiles for x = 20 mm, t = 0.7 ms are presented in Figure 6.10.

At x = 5 mm and t = 0.3 ms the resulting profiles of $\langle\chi|\eta\rangle\widetilde{P}(\eta)$ have similar peak values for all three radial positions. Along the centreline, in Figure 6.9 (a), the effect of the plateau correction on the Inhomogeneous-Gradient model is obvious, as the profile increases suddenly from zero at approximately $\eta = 0.15$. While the magnitude of the peaks are roughly similar, the Inhomogeneous-Gradient profile has its peak around $\eta = 0.2$, which is much leaner than the Inhomogeneous-Linear peak near $\eta = 0.5$. The peak of the Inhomogeneous-Gradient model has dropped from approximately 54,000 to roughly 10,000, while the peak of the Inhomogeneous-Linear model increased from approximately 4,000 to

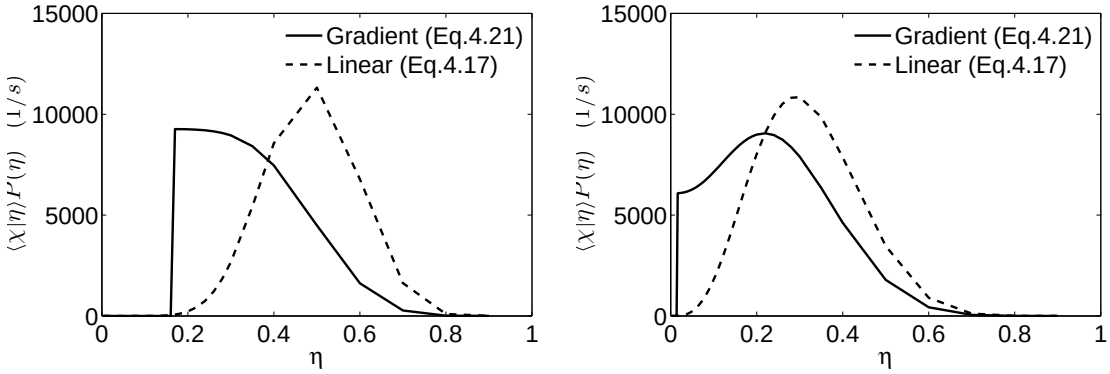

(a) r = 0 mm

(b) r = 0.5 mm

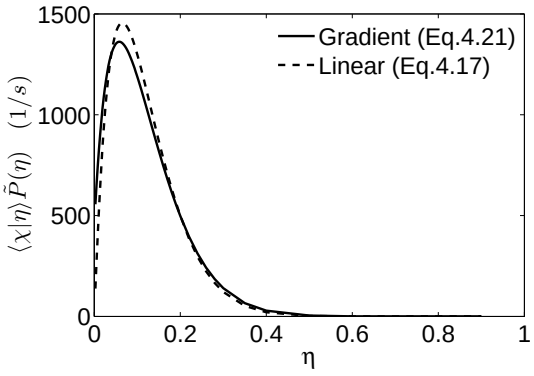

(c) r = 1 mm

Figure 6.9: Scaled profiles of $\langle\chi|\eta\rangle\widetilde{P}(\eta)$ at x = 5 mm, t = 0.3 ms.

over 10,000. At r = 0.5 mm, in Figure 6.9 (b), the scaling also forces the peaks to be closer in magnitude. The area of the Inhomogeneous-Gradient profile affected by the plateau correction is very small when compared with the centreline. At the edge of the jet, in Figure 6.9 (c), the plateau correction does not affect the Inhomogeneous-Gradient profile, but the peaks are changed due to the scaling. The change in peak values due to the scaling is illustrated in Table 6.1. As a result of the scaling, the peak of the Inhomogeneous-Linear model is increased by approximately 160% along the centreline, and decreased by 34% near the edge of the jet. The Inhomogeneous-Gradient model has its peak along the centreline reduced by 83% and by 37% near the edge of the jet.

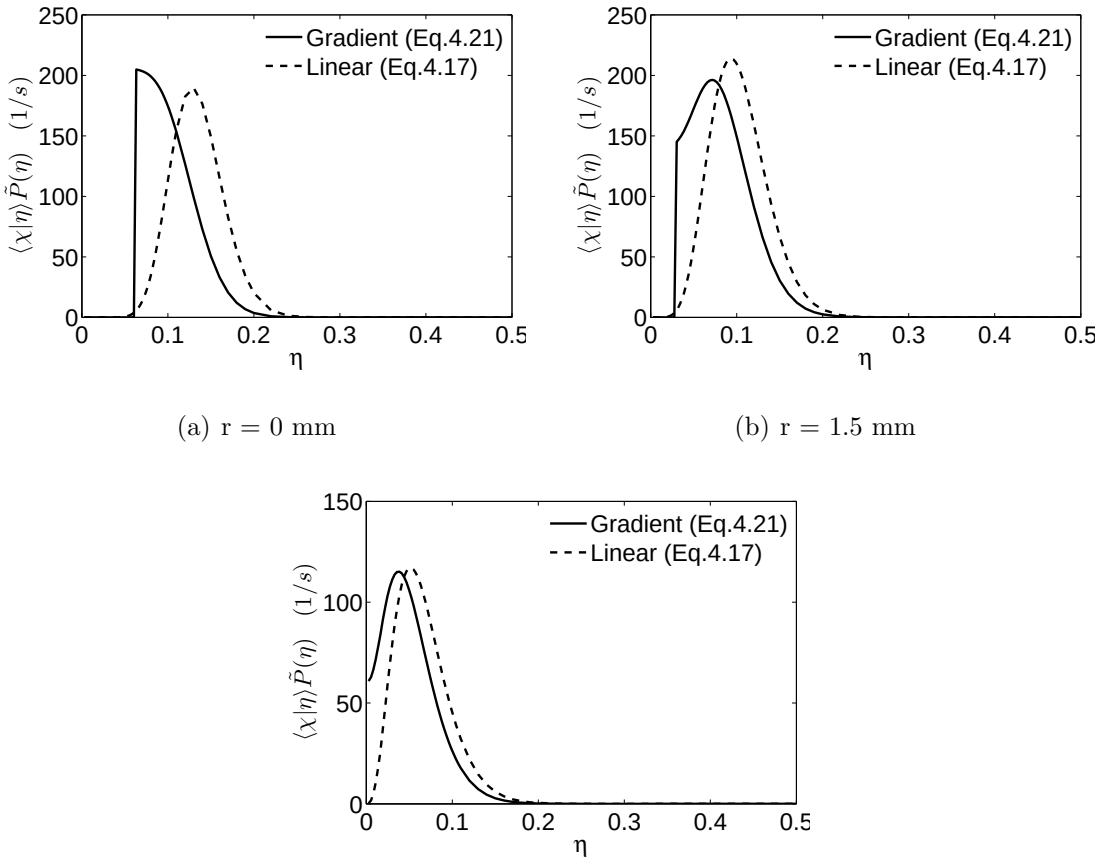

(a) r = 0 mm

(b) r = 1.5 mm

(c) r = 3 mm

Figure 6.10: Scaled profiles of $\langle\chi|\eta\rangle\widetilde{P}(\eta)$ at x = 20 mm, t = 0.7 ms.

Table 6.2: Peak values of $\langle\chi|\eta\rangle\widetilde{P}(\eta)$ $[s^{-1}]$ at x = 20 mm, t = 0.7 ms

Radius[mm]	Inhom.-Lin.	Inhom.-Lin. scaled	Inhom.-Grad.	Inhom.-Grad. scaled
0	20	190	900	200
1.5	180	215	410	195
3	130	115	175	113

The results are similar at x = 20 mm and t = 0.7 ms. At the centreline, shown in Figure 6.10 (a), the plateau correction of the Inhomogeneous-Gradient profile is evident by the sharp rise in $\langle\chi|\eta\rangle\widetilde{P}(\eta)$ that occurs at roughly $\eta = 0.06$. The effect of the scaling is to bring the peak values of the two profiles to roughly the same value. The peak of the Inhomogeneous-Gradient model remains at a considerably leaner value of η. At a radial position of 1.5 mm, presented in Figure 6.10 (b), the plateau correction has a smaller effect as the profile is forced to zero from $\eta = 0$ to approximately $\eta = 0.03$. Both the Inhomogeneous-Linear and Inhomogeneous-Gradient models now yield peaks near 200. Near the edge of the jet, in Figure 6.10 (c), the plateau correction has no impact on the Inhomogeneous-Gradient profile, as there was no unphysical plateau to correct. The effect of the scaling process on the peak values for the two implementations of the mixing model for these three locations are presented in Table 6.2. For the Inhomogeneous-Linear model, the change in the peak value ranges from an increase of nearly an order of magnitude along the centreline, to a decrease of roughly 11% near the edge of the jet. For the Inhomogeneous-Gradient model the scaling causes a reduction in the peak value of 78% along the centreline and 35% near the edge of the jet.

6.3.4 Cross-stream averaged conditional scalar dissipation rate

The conditional scalar dissipation rates from the mixing models are cross-stream averaged for use in the CMC calculations. The cross-stream averaged profiles of the conditional scalar dissipation rate and PDF are presented in Figure 6.11 (a) and (b) respectively for x = 5 mm, t = 0.3 ms and in Figure 6.11 (c) and (d) for x = 20 mm, t = 0.7 ms. For both locations, $\{\tilde{P}(\eta)\}_{R+}$ peaks at very lean mixtures. At x = 5 and t = 0.3 ms, the Inhomogeneous-Linear model yields very similar values to AMC for η values between 0 and 0.2. However, the peak values of $\{\langle\chi|\eta\rangle\}_{R+}$ are very different, as AMC reaches a much

higher peak at $\eta = 0.5$ while the Inhomogeneous-Linear peak occurs at approximately $\eta = 0.3$. For η values above 0.3 AMC produces much higher values, which is consistent with what Devaud et al. [21] observed in comparing the Inhomogeneous-Linear model with a different homogeneous mixing model (Girimaji's model). In the range of η in which the AMC values are much larger, the PDF (in Figure 6.11 (b)) is small, and thus the differences in $\{\langle\chi|\eta\rangle\}_{R+}$ between the two models for rich mixtures is not expected to have a significant impact on the CMC predictions of autoignition. The Inhomogeneous-Gradient model produces higher $\{\langle\chi|\eta\rangle\}_{R+}$ values over the lean mixture η values below 0.1, which encompasses the range of interest including the stoichiometric mixture fraction of 0.055 and the most reactive mixture, which is on the lean side of stoichiometry. The peak in the Inhomogeneous-Gradient profile occurs at a leaner mixture than the other two models, at roughly $\eta = 0.1$. The overall shape of the gradient profile is similar to the linear profile, in that it rises from zero, reaches a peak at relatively lean mixtures, and then decreases to zero with increasing η.

Further downstream, at x = 20 mm and t = 0.7 ms (Figure 6.11 (c) and (d)), the Inhomogeneous-Linear model reaches a peak of $\{\langle\chi|\eta\rangle\}_{R+} \simeq 15\ s^{-1}$ at approximately $\eta = 0.08$, while again the AMC profile by definition peaks at $\eta = 0.5$. Similar to the upstream location, the Inhomogeneous-Linear model yields very similar values to AMC up until its peak. For η values corresponding to richer mixtures than that of the the linear model's peak, the AMC results are much larger. Once again, the Inhomogeneous-Gradient model produces larger values of $\{\langle\chi|\eta\rangle\}_{R+}$ in the lean region of η, before reaching a peak of $\{\langle\chi|\eta\rangle\}_{R+} \simeq 11\ s^{-1}$ near $\eta = 0.06$. Although the peak for the gradient model is smaller the lean region of η below stoichiometry sees larger values of the conditional scalar dissipation rate, which is expected to have an impact on the autoignition results. The overall shape of the profiles from the two versions of the inhomogeneous model are in better agreement than they are at x = 5 mm, as they depict very similar behaviour with differences only in magnitude and peak η values.

The evolution in time of the conditional scalar dissipation rates, at the ignition mixture fraction and location of the Inhomogeneous-Linear model ($\eta_{ign} = 0.0220$, x = 20 mm), is presented in Figure 6.12 for the two inhomogeneous models and AMC. All three models see a sharp rise in $\langle\chi|\eta\rangle$ at t = 0.2 ms, when the tip of the fuel jet reaches the axial position. The Inhomogeneous-Gradient and Inhomogeneous-Linear model both see higher peak conditional scalar dissipation rates than the AMC model, with the Inhomogeneous-Gradient

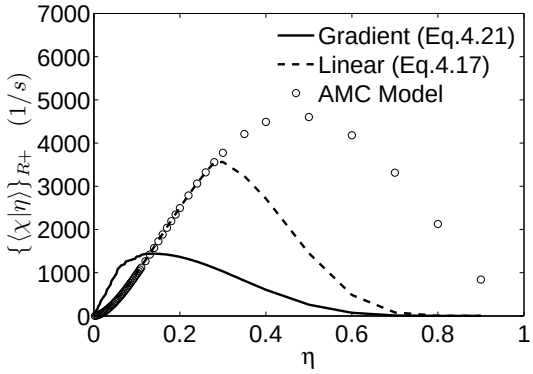

(a) x = 5 mm and t = 0.3 ms

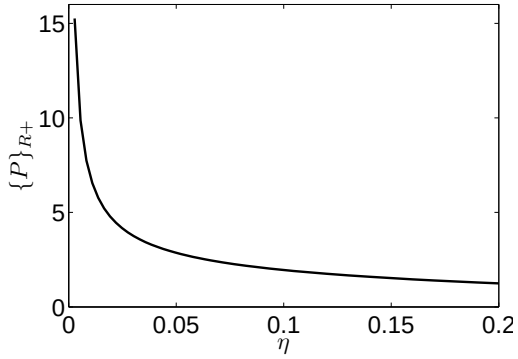

(b) x = 5 mm and t = 0.3 ms

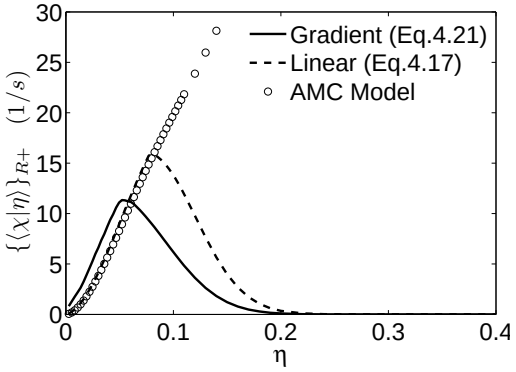

(c) x = 20 mm and t = 0.7 ms

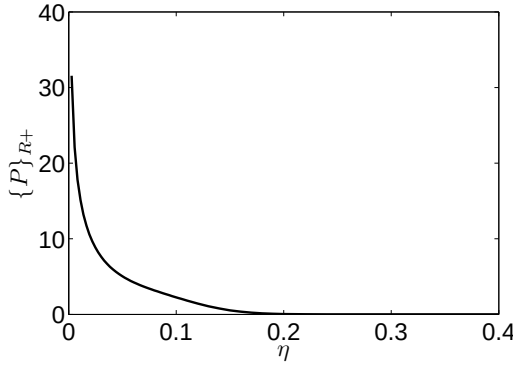

(d) x = 20 mm and t = 0.7 ms

Figure 6.11: $\{\langle\chi|\eta\rangle\}_{R+}$ (left) and $\widetilde{P}(\eta)_{R+}$ (right) profiles

peak being highest of the three. After approximately t = 0.5 ms all three models level out to an approximately constant value of $\langle\chi|\eta\rangle$. The AMC and Inhomogeneous-Linear models level off at values of $\langle\chi|\eta\rangle \simeq 1.5\ s^{-1}$, while the Inhomogeneous-Gradient model levels off at $\langle\chi|\eta\rangle \simeq 3.5\ s^{-1}$. The larger peak and higher sustained values of $\langle\chi|\eta\rangle$ for the Inhomogeneous-Gradient at this reactive mixture fraction should cause a longer ignition delay.

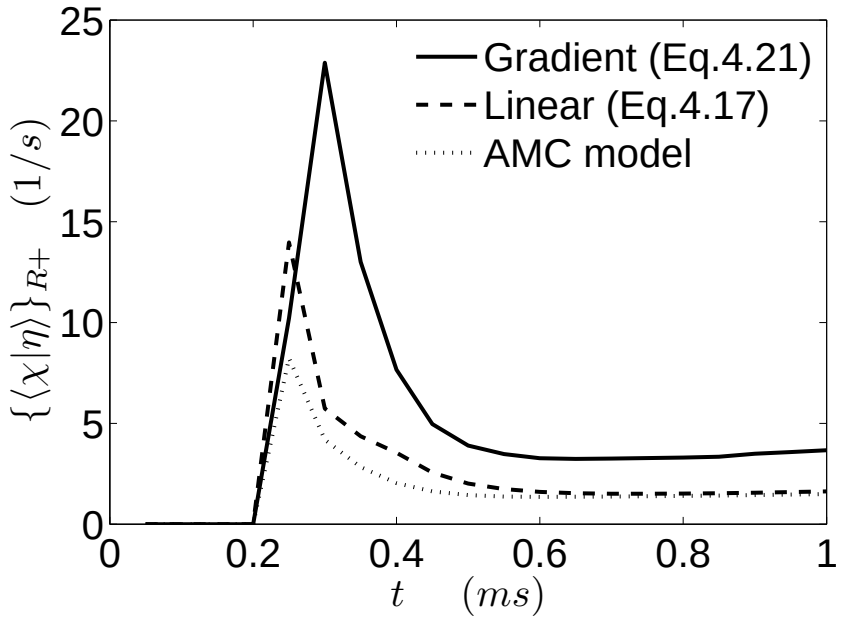

Figure 6.12: Evolution in time of $\langle\chi|\eta = 0.022\rangle$ at x = 20 mm.

6.4 Equation Budgets

The individual terms in the two inhomogeneous mixing model expressions, Equations 4.17 and 4.21, are compared by examining their behaviour at the same six physical locations used previously. The first two terms on the right hand side of both equations (terms I and II) are identical. The difference in the two versions of the inhomogeneous mixing model lies in the remaining terms - terms III and IV in the linear version and term 3

in the gradient version. Figure 6.13 presents the contribution of terms at x = 5 mm and t = 0.3 ms. At all three locations term I, which is the temporal derivative of the integral I_1, is negligible. For the Inhomogeneous-Linear model, term III is negligible along the centreline, and the production of term II is counterbalanced by term IV. For the Inhomogeneous-Gradient model, term 3 is very small along the centreline, which leaves the production of term II unopposed. This causes the large values of $\langle\chi|\eta\rangle\widetilde{P}(\eta)$ along the centreline with an extensive plateau region at lean values of η. At r = 0.5 mm, shown in Figures 6.13 (c) and (d), term II and term III are source terms for the Inhomogeneous-Linear model, while term II and term 3 are source terms for the Inhomogeneous-Gradient model. Once again, the Inhomogeneous-Gradient model does not have a negative term to counterbalance the effect of these source terms, as term IV does for the Inhomogeneous-Linear model. The general profiles of term III and term 3 are somewhat similar, although term 3 does not go to zero at $\eta = 0$ like term III does. Near the edge of the jet, in Figures 6.13 (e) and (f), the equation budgets for the Inhomogeneous-Linear model and Inhomogeneous-Gradient model look similar. At this location term II has become negative and counterbalances the production of term III and term IV in the Inhomogeneous-Linear model, and correspondingly counterbalances term 3 in the Inhomogeneous-Gradient model. The combined production of term III and term IV appears to be closely matched by that of term 3, which explains the good agreement in $\langle\chi|\eta\rangle\widetilde{P}(\eta)$ profiles at this location.

Figure 6.14 presents the contribution of terms in the mixing model equations at x = 20 mm and t = 0.7 ms. Similar to Figure 6.13, term I is negligible at each of the locations. Since this is the only time dependent term in the mixing model equations, this implies that computational expense can be saved by solving Equations 4.17 and 4.21 in steady state with little impact on the solution. Although the temporal derivative of $\widetilde{\xi}$ appears in term IV, this is due to the substitution of the transport equation of $\widetilde{\xi}$ used to simplify Equation 4.15. The trends of term II are the same as in Figure 6.13, in which it is the dominant production term along the centreline and r = 1.5 mm, but becomes negative near the edge of the jet. In the Inhomogeneous-Linear model, term IV acts to counterbalance term II along the centreline and at r = 1.5mm, and that balance is missing in the Inhomogeneous-Gradient model. Once again, the equation budgets near the edge of the jet, in Figures 6.14 (e) and (f), are similar, resulting in similar $\langle\chi|\eta\rangle\widetilde{P}(\eta)$ profiles.

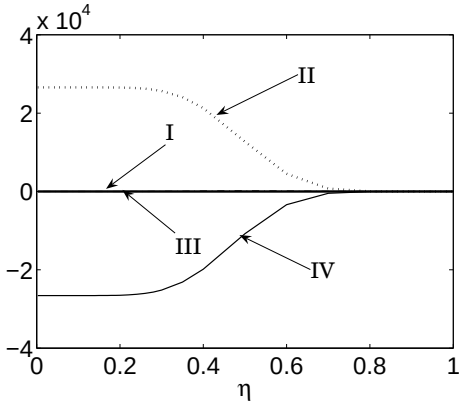

(a) r = 0 mm - linear

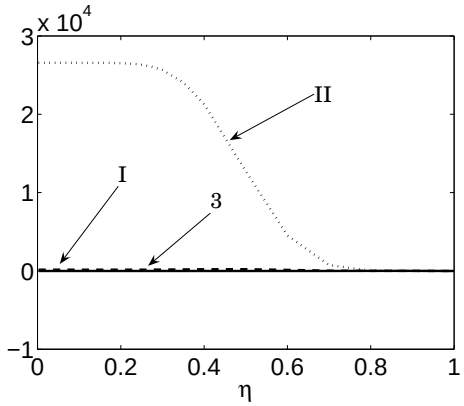

(b) r = 0 mm - gradient

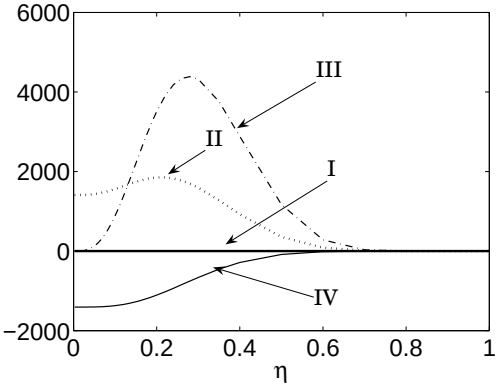

(c) r = 0.5 mm - linear

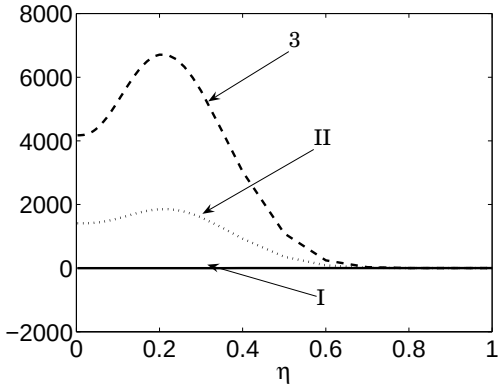

(d) r = 0.5 mm - gradient

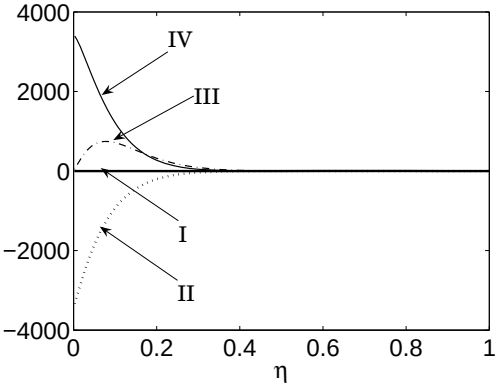

(e) r = 1 mm - linear

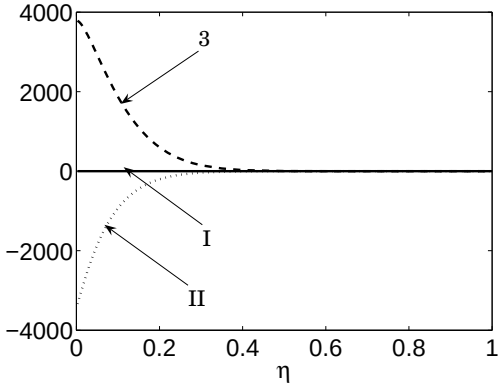

(f) r = 1 mm - gradient

Figure 6.13: Equation budgets at x = 5 mm, t = 0.3 ms.

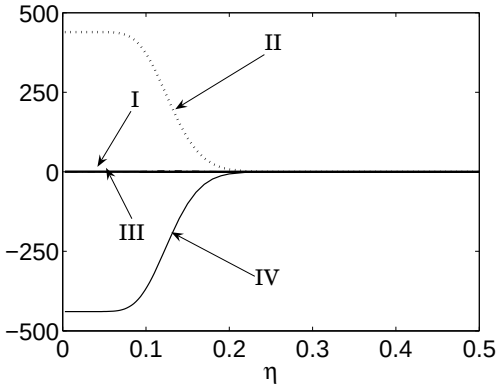

(a) r = 0 mm - linear

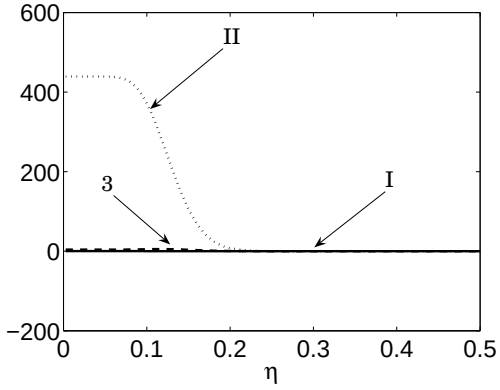

(b) r = 0 mm - gradient

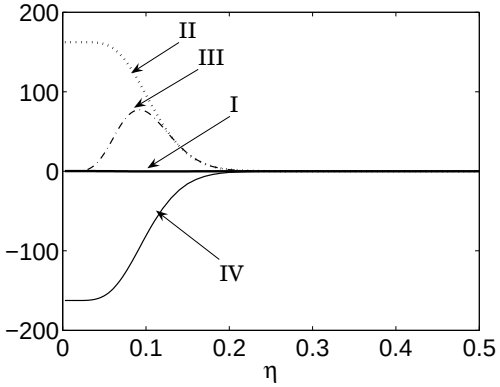

(c) r = 1.5 mm - linear

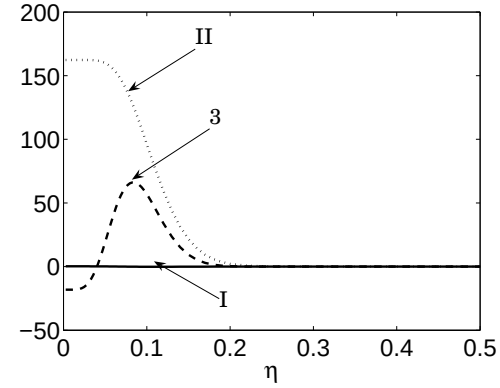

(d) r = 1.5 mm - gradient

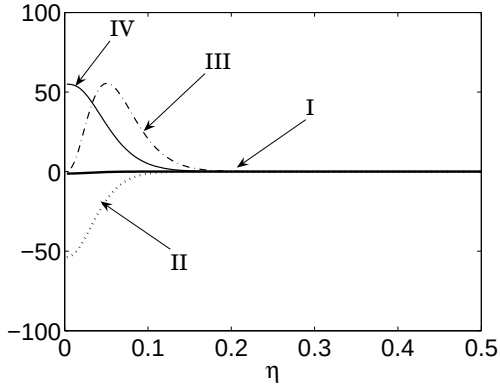

(e) r = 3 mm - linear

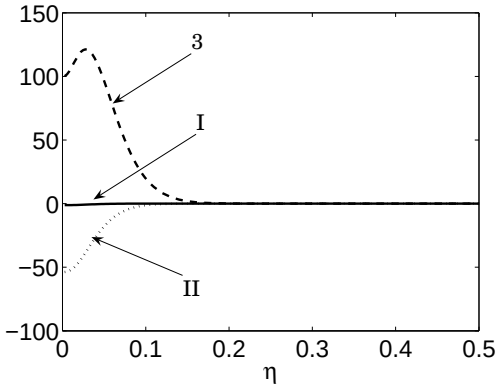

(f) r = 3 mm - gradient

Figure 6.14: Equation budgets at x = 20 mm, t = 0.7 ms.

6.5 Cross-stream Averaged CMC Autoignition Results

Figure 6.15 presents the predicted ignition delays using the two inhomogeneous expressions and two homogeneous models [44] (AMC [40] and Girimaji's [39]) with the experimental data [5]. The numerical values for the four sets of predictions are also included in Tables 6.3-6.7. As shown in Figure 6.15, the general trend of increasing ignition delay with decreasing air temperature, due to lower chemical activity at lower temperatures, is well reproduced for all models. As discussed in previous work by El Sayed and Devaud[26], both homogeneous scalar dissipation models yield comparable ignition delays, with the AMC model predicting ignition slightly earlier. This can be explained by the fact that the conditional scalar dissipation rate determined from Girimaji's model is slightly higher than that obtained using the AMC model. At all five air temperatures, the ignition delays from the Inhomogeneous-Linear model nearly identical to those from Girimaji's presumed β-PDF model.

The Inhomogeneous-Gradient model yields higher ignition delays over all air temperatures, which corresponds to the larger values of the conditional scalar dissipation rates predicted in the range of η values corresponding to lean mixtures, where chemical activity is high. Ignition is known to occur at the most reactive mixture, which is on the lean side of stoichiometry, when $\langle\chi|\eta\rangle_{R+}$ drops below its critical value [44]. The longer ignition delays for the Inhomogeneous-Gradient model is due to its higher values of $\langle\chi|\eta\rangle_{R+}$ in this lean mixture region, as more time is required for the conditional scalar dissipation rate to decrease below its critical value and approach the low values associated with ignition. The increase in ignition delay, relative to the Inhomogeneous-Linear model, ranges from 39% for the air temperature of 1385 K to 7.5% for the air temperature of 1186 K. This indicates that the conditional velocity model that is used within the inhomogeneous mixing model has a significant impact on the prediction of ignition delay. Compared the results from AMC, the ignition delays from the Inhomogeneous-Linear model range from 12 % higher at 1385 K to 3% higher at 1186 K, while the ignition delays from the Inhomogeneous-Gradient model are 56% higher than AMC at 1385 K, and 11% higher at 1186 K.

The values of the cross-stream averaged scalar dissipation rate at ignition are also shown in Tables 6.3-6.7. Ignition always occurs at low scalar dissipation rates, much lower than the critical value based on flamelet-type calculations as shown by El Sayed and De-

vaud [26]. The ignition mixture fraction, η_{ign}, is slightly different according to the air temperature and the mixing model model in agreement with previous findings [68]. The Inhomogeneous-Linear version always produces values of η_{ign} between those obtained from AMC and Girimaji's model, i.e. 0.0138 and 0.0220 depending on the air temperature. In contrast, the Inhomogeneous-Gradient model results in larger η_{ign} values ranging from 0.0192 for $T_{air} = 1385$ K to 0.0275 for $T_{air} = 1238$ K. The values found for η_{ign} are consistent with the most reactive mixture fraction (around 0.025) obtained by Kim et al.[27] for methane jets at high pressure using a different ignition criterion.

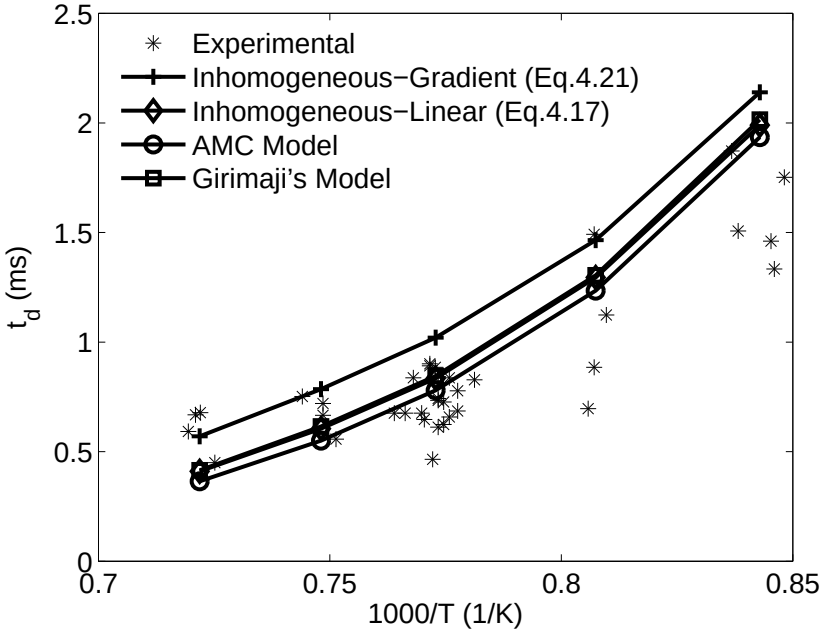

Figure 6.15: Ignition delay.

Table 6.3: Ignition results, air temperature, $T_{air} = 1385$ K

Model	t_d (ms)	χ_{ign} $(1/s)$	x_{ign} (mm)	η_{ign}
Inhomogeneous-Gradient	0.570	3.868	20	0.0192
Inhomogeneous-Linear	0.410	2.355	15	0.0138
AMC [44]	0.365	1.977	15	0.0138
Girimaji's model [44]	0.415	2.650	17.5	0.0165

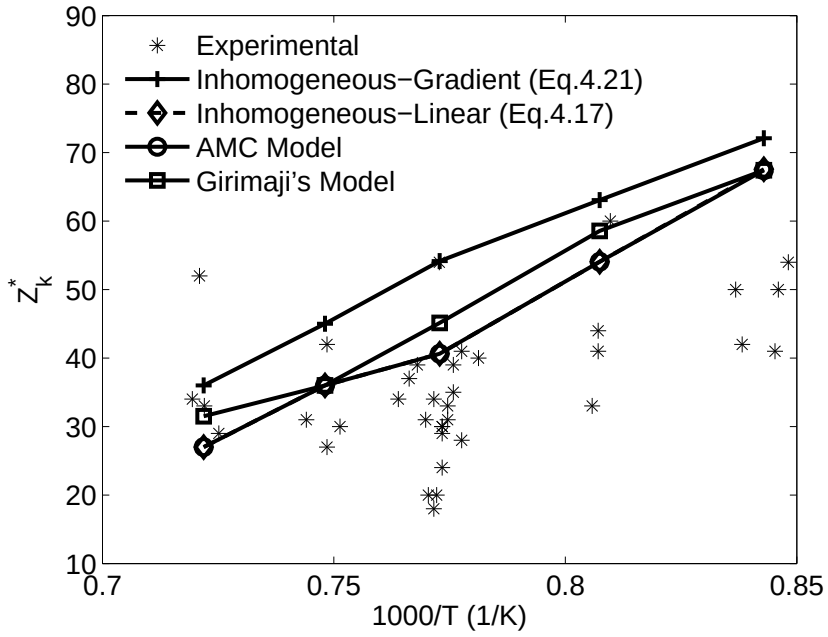

Figure 6.16: Ignition location.

Table 6.4: Ignition results, $T_{air} = 1337$ K

Model	t_d (ms)	χ_{ign} $(1/s)$	x_{ign} (mm)	η_{ign}
Inhomogeneous-Gradient	0.785	2.578	25	0.0220
Inhomogeneous-Linear	0.605	1.534	20	0.0165
AMC [44]	0.550	1.371	20	0.0165
Girimaji's model [44]	0.610	1.817	20	0.0165

Table 6.5: Ignition results, $T_{air} = 1294$ K

Model	t_d (ms)	χ_{ign} $(1/s)$	x_{ign} (mm)	η_{ign}
Inhomogeneous-Gradient	1.020	1.679	30	0.0248
Inhomogeneous-Linear	0.835	1.475	22.5	0.0192
AMC [44]	0.780	1.017	22.5	0.0192
Girimaji's model [44]	0.845	1.252	25	0.0165

Table 6.6: Ignition results, $T_{air} = 1238$ K

Model	t_d (ms)	χ_{ign} $(1/s)$	x_{ign} (mm)	η_{ign}
Inhomogeneous-Gradient	1.465	0.664	35	0.0275
Inhomogeneous-Linear	1.295	0.884	30	0.0220
AMC [44]	1.235	0.666	30	0.0192
Girimaji's model [44]	1.305	0.719	32.5	0.0220

Table 6.7: Ignition results, $T_{air} = 1186$ K

Model	t_d (ms)	χ_{ign} $(1/s)$	x_{ign} (mm)	η_{ign}
Inhomogeneous-Gradient	2.140	0.094	40	0.0248
Inhomogeneous-Linear	1.990	0.274	37.5	0.0220
AMC [44]	1.935	0.292	37.5	0.0220
Girimaji's model [44]	2.015	0.218	37.5	0.0220

Generally the autoignition predictions lie close to the experimental data. However, the scatter in the experimental data is considerable at low air temperatures and the measurements are few in number, making conclusions regarding the fit of the results to experimental data marginal. The ignition delay results from the Inhomogeneous-Linear model, AMC, and Girimaji's model are in good agreement with the experiments at T = 1294 K (corresponding to $1000/T \simeq 0.77$), where the experimental data points are most numerous and closely clustered. At this location the Inhomogeneous-Gradient results overpredict the experimental ignition delay, which indicates that the higher conditional scalar dissipation rates due to divergent conditional velocity behaviour is adversely affecting the predictions of autoignition. For the lowest air temperature, $T_{air} = 1186$ K, the previous results obtained using AMC and Girimaji's model were noted to overpredict experimental values for low air temperatures [44], and the Inhomogeneous-Gradient model yields an even larger overprediction. For the highest air temperature, $T_{air} = 1385$ K, the previous homogeneous mixing models results slightly underpredicted the experimental data [44]. The use of the Inhomogeneous-Gradient mixing model brought the predictions closer to the cluster of experimental data. However, due to the numerical issues observed with the gradient conditional velocity model due to use of the β-PDF, it cannot be concluded that this improved agreement with experimental data is due to more accurate modelling of the autoignition problem.

Figure 6.16 shows the normalized ignition locations given by the expression

$$Z_k^* = x_{ign}/d(p_i/p_o)^{1/2}, \tag{6.4}$$

where x_{ign} is the axial ignition location, d the injector diameter, p_i the fuel injection pressure and p_o the initial air pressure. The Inhomogeneous-Gradient model ignition locations are all further downstream than those from the Inhomogeneous-Linear model, ranging from 33% higher for the highest air temperature to 6% higher for the lowest air temperature. This trend is linked to the higher values of the conditional scalar dissipation rate from the mixing model, as large values of $\langle\chi|\eta\rangle$ are expected to delay ignition and move the ignition location further downstream. For low air temperatures all four mixing models yield results that overpredict the experimental data. At higher air temperatures the ignition locations are closer to the experimental scatter. However, at the air temperature with the most experimental data available, $T_{air} = 1294$ (corresponding to $1000/T \simeq = 0.77$), the predicted ignition locations are not as in good agreement with the measured locations when compared with the results of ignition delay. The scatter in experimental data is significant for all five air temperatures, and the general trend of increasing distance with decreasing air temperature is not clearly visible from the data, as some of the smallest experimental values of Z_k^* are at the middle air temperature.

For all four of the mixing models, the conditional scalar dissipation rate at ignition decreases with decreasing air temperature. At higher air temperatures ignition occurs at higher χ_{ign} in the Inhomogeneous-Gradient model when compared with the other models. However, for lower air temperature the ignition scalar dissipation rate for the Inhomogeneous-Gradient model is the smallest. Similarly, ignition for the Inhomogeneous-Linear model is found at χ_{ign} values higher than those of the AMC model for high air temperatures, but at a lower value of χ_{ign} for the lowest air temperature.

6.5.1 Impact of plateau correction

The impact of the plateau correction, or conversely the effect of the unphysical plateau itself, on the autoignition predictions is examined by comparing the ignition delay and location results from Section 6.5 with CMC results obtained using unaltered Inhomogeneous-Gradient $\langle\chi|\eta\rangle$ profiles. The difference in predicted ignition delay, without considering

Table 6.8: Inhomogeneous-Gradient ignition delay comparison with and without the plateau correction

T_{air}	t_d with plateau correction (ms)	t_d without correction (ms)	difference (%)
1385 K	0.655	0.735	10.8
1337 K	0.905	0.950	4.7
1294 K	1.160	1.200	3.3
1238 K	1.630	1.670	2.4
1186 K	2.300	2.335	1.5

Table 6.9: Inhomogeneous-Gradient Ignition location comparison with and without the plateau correction

T_{air}	x_{ign} with plateau correction (mm)	x_{ign} without correction (mm)	difference (%)
1385 K	22.5	25.0	10.0
1337 K	27.5	30.0	8.3
1294 K	32.5	35.0	7.1
1238 K	40.0	40.0	0
1186 K	42.5	42.5	0

scaling of the profiles of $\langle\chi|\eta\rangle\widetilde{P}(\eta)$, is presented in Table 6.8. For all air temperatures the end result is a shortened ignition delay. The plateau correction has a larger relative impact for higher air temperatures, which correspond to the shortest ignition delays. Forcing the unphysical plateau to zero causes a drop in the ignition delay of nearly 11% for T_{air} = 1385 K. For lower air temperatures the effect is less pronounced, as the ignition delay is decreased by only 1.5% for T_{air} = 1186 K.

Table 6.9 shows the impact of the plateau correction on the ignition locations predicted by the Inhomogeneous-Gradient model. The trends are very similar to those observed in ignition delay. For higher air temperatures the ignition location is moved closer toward the injector, while for low air temperatures there is no change. The reduction in the value for x_{ign} at high air temperatures corresponds to the shortened ignition delay observed with the plateau correction. At T_{air} = 1385 K the distance to the ignition location decreases by 10%.

To illustrate why the plateau-correction yields shorter ignition delays, Figure 6.17 shows the effect of the plateau-correction on the profiles of $\langle\chi|\eta\rangle_{R+}$ at x = 5 mm, t =

0.3 ms and at x = 20 mm, t = 0.7 ms. For both locations the plateau-corrected profiles yield lower values of the conditional scalar dissipation rate for η values on the lean side of stoichiometry ($\eta_{stoich} = 0.055$), around the most reactive mixture. In this lean mixture region chemical activity is the highest, and ignition will occur at the most reactive mixture if the scalar dissipation rate is below its critical value [26]. With a reduction in the values of $\langle\chi|\eta\rangle_{R+}$, this indicates that the scalar dissipation rate will drop below its critical value earlier due to the effects of the plateau correction, yielding shorter ignition delays and correspondingly smaller values of x_{ign}.

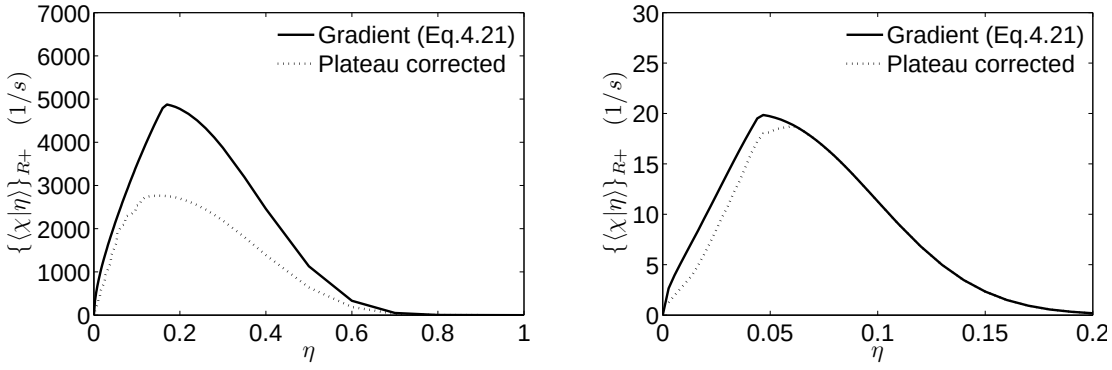

(a) x = 5 mm and t = 0.3 ms

(b) x = 20 mm and t = 0.7 ms

Figure 6.17: Impact of plateau correction in the Inhomogeneous-Gradient model on (unscaled) profiles of $\langle\chi|\eta\rangle_{R+}$

6.5.2 Impact of scaling

In a similar manner, the impact of scaling the profiles of $\langle\chi|\eta\rangle\widetilde{P}(\eta)$ to yield mean $\tilde{\chi}$ values consistent with that from the mixture fraction variance equation (Equation 2.56) can be examined by comparison of the autoignition results with those obtained without scaling. The impact on the predicted ignition delay for the Inhomogeneous-Gradient and Inhomogeneous-Linear models are presented in Tables 6.10 and 6.11 respectively. It should be noted that the results presented with and without scaling for the Inhomogeneous-Gradient model already include the plateau-correction outlined in Section 6.3.2.

Table 6.10: Inhomogeneous-Gradient ignition delay comparison with and without scaling

T_{air}	t_d with scaling (ms)	t_d without scaling (ms)	difference (%)
1385 K	0.570	0.655	13.0
1337 K	0.785	0.905	13.3
1294 K	1.020	1.160	12.1
1238 K	1.465	1.630	10.0
1186 K	2.140	2.300	7.0

Table 6.11: Inhomogeneous-Linear ignition delay comparison with and without scaling

T_{air}	t_d with scaling (ms)	t_d without scaling (ms)	difference (%)
1385 K	0.410	0.470	12.8
1337 K	0.605	0.675	10.3
1294 K	0.835	0.910	8.2
1238 K	1.295	1.375	5.8
1186 K	1.990	2.055	3.2

For the Inhomogeneous-Gradient model, the scaling of $\langle\chi|\eta\rangle\widetilde{P}(\eta)$ causes a noticeable decrease in the ignition delays for all air temperatures. The relative decrease in ignition delay for the two highest air temperatures, 1385 K and 1337 K, is slightly higher than the others at roughly 13 %. At the lowest air temperature, $T_{air} = 1186$ K, the relative change is 7%. A similar trend is observed in the results for the Inhomogeneous-Linear model. The ignition delays are reduced for all five air temperatures, with the relative change being the highest for the high air temperatures. The decrease in ignition delays range from 13% for $T_{air} = 1385$ K, to 3% for $T_{air} = 1186$ K. Comparing the relative change with the Inhomogeneous-Gradient model, the act of scaling $\langle\chi|\eta\rangle\widetilde{P}(\eta)$ has roughly the same impact for high air temperature. However, the scaling causes a larger relative decrease in the ignition delay for low air temperatures in the Inhomogeneous-Gradient model.

The change in predicted ignition locations for the Inhomogeneous-Gradient and Inhomogeneous-Linear models are presented in Tables 6.12 and 6.13 respectively. Corresponding to the noted decrease in ignition delays, the ignition locations are observed to decrease with scaling of $\langle\chi|\eta\rangle\widetilde{P}(\eta)$ as well, with the exception of $T_{air} = 1337$ K and 1186 K for the Inhomogeneous-Linear model, which saw no change. For the Inhomogeneous-Gradient model, the general trend in the impact of scaling on x_{ign} is to decrease with

Table 6.12: Inhomogeneous-Gradient ignition location comparison with and without scaling

T_{air}	x_{ign} with scaling (mm)	x_{ign} without scaling (mm)	difference (%)
1385 K	20.0	22.5	11.1
1337 K	25.0	27.5	9.1
1294 K	30.0	32.5	7.7
1238 K	35.0	40.0	12.5
1186 K	40.0	42.5	5.9

Table 6.13: Inhomogeneous-Linear ignition location comparison with and without scaling

T_{air}	x_{ign} with scaling (mm)	x_{ign} without scaling (mm)	difference (%)
1385 K	15.0	17.5	14.3
1337 K	20.0	20.0	0
1294 K	22.5	25.0	10.0
1238 K	30.0	32.5	7.7
1186 K	37.5	37.5	0

increasing air temperature, except at $T_{air} = 1238$ K, which sees the largest change. The decrease in x_{ign} ranges from 12.5% at $T_{air} = 1238$ K to 6 % at $T_{air} = 1186$ K. For the Inhomogeneous-Linear model, the general observed trend in x_{ign} reduction is decreasing impact with decreasing air temperature. Outside of the trend is $T_{air} = 1337$ K, at which x_{ign} did not change with scaling. The highest relative change in ignition location is 14% for $T_{air} = 1385$ K.

The impact of scaling the profiles of $\langle\chi|\eta\rangle\widetilde{P}(\eta)$ on the cross-stream averaged profiles of the conditional scalar dissipation rate is illustrated in Figure 6.18. For both models the scaling causes a decrease in values of $\langle\chi|\eta\rangle_{R+}$ in the lean mixture region near stoichiometry ($\eta_{stoich} = 0.055$) and the most reactive mixture fraction. The relative decrease in $\langle\chi|\eta\rangle_{R+}$ for the Inhomogeneous-Gradient model is larger than that for the Inhomogeneous-Linear model, which is in agreement with the generally larger reduction in ignition delay for the Inhomogeneous-Gradient model, particularly for lower air temperatures. The lower values for $\langle\chi|\eta\rangle_{R+}$ in this important range of η values indicate that the scalar dissipation rate will drop below the critical value at the most reactive mixture fraction earlier, yielding shorter ignition delays.

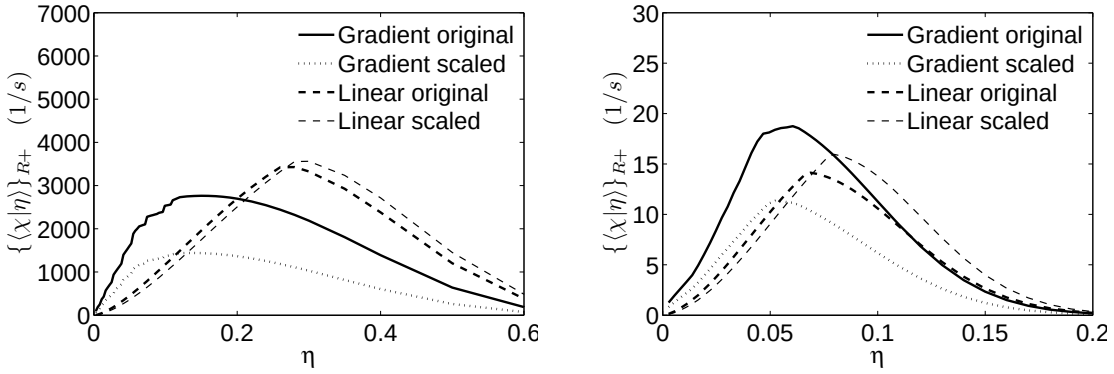

(a) x = 5 mm and t = 0.3 ms

(b) x = 20 mm and t = 0.7 ms

Figure 6.18: Impact of scaling of $\langle\chi|\eta\rangle\widetilde{P}(\eta)$ on profiles of $\langle\chi|\eta\rangle_{R+}$

6.6 Summary

The behaviour of the gradient conditional velocity model departed significantly from the linear relationship in some regions. The gradient model showed diverging behaviour at the rich and lean limits in locations in the flow where the values of the corresponding PDF were near zero. The conditional velocity obtained by the linear model was in agreement with that of the gradient model within 1.5 - 4 standard deviations of the mean mixture fraction. Cross-stream averaging of the conditional velocity yielded profiles that were similar for both models in the lean region of mixture fraction space where chemical activity can take place. Consequently, the differences observed in the predicted ignition delay and ignition location between the two formulations of the inhomogeneous model were only due to the subsequent effect of the conditional velocity models within the conditional scalar dissipation rate expression. Only the cross-stream averaged axial component of the conditional velocity was considered in the CMC calculations, and thus the difference in conditional velocity models did not impact the convective terms appearing in the CMC equations.

The conditional velocity used in the mixing model equations significantly affected the magnitude and shape of the conditional scalar dissipation rate within the fuel jet. In particular, the Inhomogeneous-Gradient expression resulted in some unphysical behaviour of the conditional scalar dissipation rate in low probability regions and for values of mixture fraction smaller than the Favre-averaged value. This unphysical behaviour disappeared

when the PDF moved to leaner mixtures. At locations where the PDF was large at lean mixtures, such as near the edge of the mixing layer, both inhomogeneous versions produced qualitatively similar profiles of $\langle\chi|\eta\rangle$, with larger values for the Inhomogeneous-Gradient. When cross-stream averaged, the profiles did not display any implausible values. However, some significant discrepancies were noticed between the mean value of the scalar dissipation rate, used in the mixture fraction variance transport equation, and the mean value obtained by integration of $\langle\chi|\eta\rangle\widetilde{P}(\eta)$ over mixture fraction space for both models. The discrepancy was expected for the Inhomogeneous-Linear model as this formulation was shown not to be consistent with the second moment of mixture fraction [21]. The departure from the mean value was even larger for the Inhomogeneous-Gradient. This was initially unexpected as the advantage of using the gradient diffusion model for the conditional velocity was that it was completely consistent with the unconditional and conditional fluxes of reactive and passive scalars [38]. However, the discrepancies in the Inhomogeneous-Gradient results are in agreement with the findings of Mortensen and de Bruyn Kops [24] when they used a β PDF. The gradient diffusion model is proportional to the gradient of the mixture fraction PDF, thus the presumed form of the PDF has a direct impact the conditional velocity model. The β-PDF is known to characterize homogeneous flows accurately, but its use for inhomogeneous flows may be questionable [38, 39]. Thus, improvement in the description of the PDF could yield better results with the gradient model. Further comparison for the scalar dissipation rate may be needed when more accurate experimental measurements of $\tilde{\chi}$ and DNS data for inhomogeneous flows are made available. In particular, it would be very useful to evaluate the possible uncertainties introduced by the gradient model when implemented with the β PDF. For consistency, all the scalar dissipation rate profiles at each position and time were scaled to yield the same mean scalar dissipation rate used in the mixture fraction variance transport equation.

The Inhomogeneous-Gradient mixing model had a significant effect on the prediction of ignition delay and location in comparison with the results using AMC or Girimaji's model. In contrast, the Inhomogeneous-Linear form did not produce any significant differences with the two homogeneous models. The Inhomogeneous-Gradient version yielded longer ignition delays and predicted ignition locations further downstream when compared with the Inhomogeneous-Linear form. The difference in predictions between the two forms of the inhomogeneous model was larger at high air temperatures and decreased with decreasing air temperatures. The predicted ignition delays and ignition locations using the

Inhomogeneous-Gradient conditional scalar dissipation rate equation was larger than those using the homogeneous mixing models, while maintaining similar trends. These differences are explained by the different temporal and spatial evolution and magnitude of $\langle\chi|\eta\rangle$ in mixture fraction space determined by the Inhomogeneous-Gradient mixing model compared to those produced by AMC or Girimaji's model. The time evolution of the conditional scalar dissipation rate at a given value of η and position was qualitatively similar for all models. In all cases, ignition occurred when the scalar dissipation rate was at its lowest and steady-state value.

In the next chapter a preliminary two-dimensional solution of the CMC equations is presented, to assess the impact of cross-stream averaging on the autoignition results. Ignition delay and location are also extracted from a two-dimensional temperature field that is obtained through integration of the PDF and axial conditional temperature results from the cross-stream averaged CMC solution.

Chapter 7

Two-dimensional CMC Solution

In addition to solving the cross-stream averaged CMC equations, a preliminary two-dimensional solution is performed to assess the impact of the shear flow approximation that is used to justify cross-stream averaging of the CMC equations. In this chapter the two-dimensional form of conditional species mass fraction is presented along with the solution methodology. The alternating direction implicit method is outlined, and its implementation within the fractional step approach is described. The two-dimensional autoignition results using the AMC mixing model are compared with corresponding cross-stream averaged results. Further, a two-dimensional temperature field is calculated from the cross-stream averaged AMC results and used to estimate a two-dimensional ignition delay location.

7.1 Solution Methodology

The autoignition problem examined in this study involves an axisymmetric fuel jet, allowing for a two dimensional implementation by neglecting any variation in the circumferential direction of the shock tube. The conditional species mass fraction transport equation for two dimensions is given by

$$\frac{\partial Q_\alpha}{\partial t} = -\left[\langle u|\eta\rangle - \frac{D_t}{\langle\rho\rangle}\frac{\partial\langle\rho\rangle}{\partial x} - \frac{\partial D_t}{\partial x}\right]\frac{\partial Q_\alpha}{\partial x} - \left[\langle v|\eta\rangle - \frac{D_t}{\langle\rho\rangle}\frac{\partial\langle\rho\rangle}{\partial y} - \frac{\partial D_t}{\partial y}\right]\frac{\partial Q_\alpha}{\partial y} \qquad (7.1)$$
$$+D_t\frac{\partial^2 Q_\alpha}{\partial x^2} + D_t\frac{\partial^2 Q_\alpha}{\partial y^2} + \frac{1}{2}\langle\chi|\eta\rangle\frac{\partial^2 Q_\alpha}{\partial\eta^2} + \frac{\langle\dot{\omega}|\eta\rangle}{\langle\rho|\eta\rangle}.$$

The two-dimensional CMC simulations do not feature implementations of the two forms of the inhomogeneous mixing model. For simplicity only the homogeneous AMC model is used. Due to computational expense only the three highest air temperatures (T_{air} = 1385 K, 1337 K, and 1294 K) are considered. These three air temperatures feature the shortest ignition delays of the experimental data set and allow for a smaller two-dimensional section of the shock tube to be used in the solution of the CMC equations. For direct comparison with the cross-stream averaged autoignition results using the AMC model [44] flow field simulations are performed in CFX for each of the three air temperatures. In contrast to the inhomogeneous mixing model implementation discussed in Chapter 5, the conditional scalar dissipation rate from the AMC model is not calculated within the flow field solution, but instead is performed after the flow field data libraries have been exported. The reason for this is that the AMC model is straightforward to calculate using the exported values of the mixture fraction and its variance, and does not require local gradients to be resolved as is the case with the inhomogeneous mixing models. Thus, the computational expense for the flow field solution is significantly lower for the AMC implementation. Flow field data is exported from CFX simulations at 50 μs intervals in a manner identical to that outlined in Chapter 5.

A two-dimensional grid in physical space is used for the solution of the CMC equations, extending 70 mm in the axial direction and 13 mm in the radial direction. This region encompasses the full extent of the fuel jet for all three air temperatures being examined, and autoignition is expected to occur well within its bounds. In the axial direction 29 equally spaced points are used, identical to those in the cross-stream averaged solution. In the place of cross-stream averaging implemented previously [44], the data from the flow field is instead processed and the relevant conditionally averaged quantities are exported at 15 equally spaced radial points. To examine the effect of grid spacing in the radial direction, a grid with 25 equally spaced points is also examined. The difference in ignition delay between the two radial grid densities ranged from 5% for the highest air temperature to 1% for the lowest of the three air temperatures. The axial ignition locations were identical for T_{air} = 1385 K and 1337 K, while the finer radial grid predicts ignition one grid point closer to the injector for $T_{air} = 1294K$. The results from the 15 point radial grid are presented in this chapter. The chemical kinetics utilize CHEMKIN II [63] and UBC Mech 1.0 [64], as outlined in Chapter 5. The same ignition criteria as the cross-stream averaged simulations, a rise in the conditional temperature by 75 K, is employed.

7.2 Application of the Fractional Step Method

In a manner similar to the cross-stream averaged CMC equations, the two dimensional equations are solved using the fractional step method. The non-stiff physical transport terms are split from the stiff chemical source term and the micromixing term. In the first fractional step, the physical transport terms are solved in spatial coordinates over the interval [t, t+dt/2]. The second fractional step is used for the solution of the chemical source term and micromixing term in mixture fraction space over the interval [t,t+dt]. Finally the physical transport terms are solved again in the third fractional step over the interval [t+dt/2,t+dt]. Due to the added complexity of considering a second spatial coordinate (the radial coordinate), the solution of the physical transport terms is not as straightforward as it was in the cross-stream averaged case.

7.2.1 Alternating Direction Implicit method

Due to the addition of a radial dimension, a simple application of LU-decomposition cannot be used. A procedure called the Alternating Direction Implicit method (ADI) provides a convenient way to address this problem. This approach falls under the category of operator splitting, is unconditionally stable, and is second-order accurate in time and space [59]. The idea behind it is to divide the timestep into two equal substeps. In the first substep one direction (x) is treated implicitly by using finite differences using known values, while the other direction (y) is treated explicitly by utilizing known values. In the subsequent substep, the treatments are reversed, with x being treated explicitly and y being treated implicitly [69].

The ADI method allows for each of the fractional steps in which the physical transport terms are solved to be further split into two substeps. The same LU-decomposition approach used for the cross-stream averaged solution can then be applied twice, once for each substep in the ADI method. The first application of the LU-decomposition solves the transport equation in which the x-direction is treated implicitly, while the second applica-

tion solves the transport equation in which the y-direction is treated implicitly.

7.2.2 Physical transport terms

In the first fractional step, the equation

$$\frac{\partial Q_\alpha}{\partial t} = -\left[\langle u|\eta\rangle - \frac{D_t}{\langle\rho\rangle}\frac{\partial\langle\rho\rangle}{\partial x} - \frac{\partial D_t}{\partial x}\right]\frac{\partial Q_\alpha}{\partial x} - \left[\langle v|\eta\rangle - \frac{D_t}{\langle\rho\rangle}\frac{\partial\langle\rho\rangle}{\partial y} - \frac{\partial D_t}{\partial y}\right]\frac{\partial Q_\alpha}{\partial y} + D_t\frac{\partial^2 Q_\alpha}{\partial x^2} + D_t\frac{\partial^2 Q_\alpha}{\partial y^2}, \tag{7.2}$$

is solved over the interval [t,t+dt/2]. Following the procedure outlined in the cross-stream averaged solution, finite differences are used to discretize Equation 7.2. For all internal nodes first order backward differencing is used for first derivatives, and second order central differencing for second derivatives. Since the flowfield is an axisymmetric jet, radial derivatives along the centreline are set equal to zero. Spacing is uniform in the axial direction and the radial direction, but it should be noted that $\Delta x \neq \Delta r$.

$$\frac{\partial Q_\alpha}{\partial x} = \frac{Q_\alpha|_{i,j}^{t+\Delta t} - Q_\alpha|_{i-1,j}^{t+\Delta t}}{\Delta x}, \tag{7.3}$$

$$\frac{\partial Q_\alpha}{\partial r} = \frac{Q_\alpha|_{i,j}^{t+\Delta t} - Q_\alpha|_{i,j-1}^{t+\Delta t}}{\Delta r}, \tag{7.4}$$

$$\frac{\partial^2 Q_\alpha}{\partial x^2} = \frac{Q_\alpha|_{i+1,j}^{t+\Delta t} - 2Q_\alpha|_{i,j}^{t+\Delta t} + Q_\alpha|_{i-1,j}^{t+\Delta t}}{(\Delta x)^2}, \tag{7.5}$$

$$\frac{\partial^2 Q_\alpha}{\partial x^2} = \frac{Q_\alpha|_{i,j+1}^{t+\Delta t} - 2Q_\alpha|_{i,j}^{t+\Delta t} + Q_\alpha|_{i,j-1}^{t+\Delta t}}{(\Delta r)^2}. \tag{7.6}$$

Substituting the above derivative approximations into Equation 7.2 and making use of the following simplifications

$$\Psi|_{i,j}^{t+\Delta t} = \langle u|\eta\rangle - \frac{D_t}{\langle\rho\rangle}\frac{\partial\langle\rho\rangle}{\partial x} - \frac{\partial D_t}{\partial x}, \tag{7.7}$$

$$\Psi_r|_{i,j}^{t+\Delta t} = \langle v|\eta\rangle - \frac{D_t}{\langle\rho\rangle}\frac{\partial\langle\rho\rangle}{\partial r} - \frac{\partial D_t}{\partial r}, \tag{7.8}$$

the discretized two-dimensional CMC equation for spatial terms becomes

$$\begin{aligned} Q_\alpha|_{i,j}^{t+\Delta t} - Q_\alpha|_{i,j}^{t} = &-\Psi|_{i,j}^{t+\Delta t}\left[\frac{Q_\alpha|_{i,j}^{t+\Delta t} - Q_\alpha|_{i-1,j}^{t+\Delta t}}{\Delta x}\right]\Delta t - \Psi_r|_{i,j}^{t+\Delta t}\left[\frac{Q_\alpha|_{i,j}^{t+\Delta t} - Q_\alpha|_{i,j-1}^{t+\Delta t}}{\Delta r}\right]\Delta t \\ &+ D_t\left[\frac{Q_\alpha|_{i+1,j}^{t+\Delta t} - 2Q_\alpha|_{i,j}^{t+\Delta t} + Q_\alpha|_{i-1,j}^{t+\Delta t}}{(\Delta x)^2}\right]\Delta t + D_t\left[\frac{Q_\alpha|_{i,j+1}^{t+\Delta t} - 2Q_\alpha|_{i,j}^{t+\Delta t} + Q_\alpha|_{i,j-1}^{t+\Delta t}}{(\Delta r)^2}\right]\Delta t. \end{aligned} \tag{7.9}$$

Equation 7.9 can be rewritten as

$$Q_\alpha|_{i,j}^{t} = AQ_\alpha|_{i-1,j}^{t+\Delta t} + BQ_\alpha|_{i,j}^{t+\Delta t} + CQ_\alpha|_{i+1,j}^{t+\Delta t} + DQ_\alpha|_{i,j-1}^{t+\Delta t} + EQ_\alpha|_{i,j+1}^{t+\Delta t}, \tag{7.10}$$

where the coefficients are given by

$$A = \left[\frac{\Psi|_{i,j}^{t+\Delta t}}{\Delta x} - \frac{D_t}{(\Delta x)^2} + \frac{2D_t}{(\Delta r)^2}\right]\Delta t, \tag{7.11}$$

$$B = \left[1 - \frac{\Psi|_{i,j}^{t+\Delta t}}{\Delta x} - \frac{\Psi_r|_{i,j}^{t+\Delta t}}{\Delta r} + \frac{2D_t}{(\Delta x)^2} + \frac{2D_t}{(\Delta r)^2}\right]\Delta t, \tag{7.12}$$

$$C = \left[-\frac{D_t}{(\Delta x)^2}\right]\Delta t, \tag{7.13}$$

$$D = \left[\frac{\Psi_r|_{i,j}^{t+\Delta t}}{\Delta r} - \frac{D_t}{(\Delta r)^2}\right]\Delta t, \tag{7.14}$$

$$E = \left[-\frac{D_t}{(\Delta r)^2}\right]\Delta t. \tag{7.15}$$

Using the ADI method, the physical transport fractional step must be further split into two parts. Over the first half of the fractional step (substep 1), the transport equation to be solved is

$$Q_\alpha|_{i,j}^{t} - \underbrace{DQ_\alpha|_{i,j-1}^{t+\Delta t} - EQ_\alpha|_{i,j+1}^{t+\Delta t}}_{\text{Treat as known}} = \underbrace{AQ_\alpha|_{i-1,j}^{t+\Delta t} + BQ_\alpha|_{i,j}^{t+\Delta t} + CQ_\alpha|_{i+1,j}^{t+\Delta t}}_{\text{Solve in LU decomposition}}. \tag{7.16}$$

For simplicity, the terms on the left hand side are grouped together into one term

$$Q^*_\alpha|^{t+}_{i,j} = Q_\alpha|^t_{i,j} - DQ_\alpha|^{t+\Delta t}_{i,j-1} - EQ_\alpha|^{t+\Delta t}_{i,j+1}. \tag{7.17}$$

The system of equations for the axial direction can be represented by

$$\begin{bmatrix} 1 & 0 & 0 & 0 & \cdots & 0 & 0 & 0 \\ A_{2,j} & B_{2,j} & C_{2,j} & 0 & \cdots & 0 & 0 & 0 \\ 0 & A_{3,j} & B_{3,j} & C_{3,j} & \cdots & 0 & 0 & 0 \\ \vdots & & \vdots & & \ddots & \vdots & & \vdots \\ 0 & 0 & 0 & 0 & \cdots & A_{N_x-1,j} & B_{N_x-1,j} & C_{N_x-1,j} \\ 0 & 0 & 0 & 0 & \cdots & A_{N_x,j} & B_{N_x,j} & C_{N_x,j} \end{bmatrix} \times \begin{bmatrix} Q_\alpha|^{t+\Delta t}_{1,j} \\ Q_\alpha|^{t+\Delta t}_{2,j} \\ Q_\alpha|^{t+\Delta t}_{3,j} \\ \vdots \\ Q_\alpha|^{t+\Delta t}_{N_x-1,j} \\ Q_\alpha|^{t+\Delta t}_{N_x} \end{bmatrix} = \begin{bmatrix} Q^*_\alpha|^t_{1,j} \\ Q^*_\alpha|^t_{2,j} \\ Q^*_\alpha|^t_{3,j} \\ \vdots \\ Q^*_\alpha|^t_{N_x-1,j} \\ Q^*_\alpha|^t_{N_x,j} \end{bmatrix}$$

The LU-decomposition is performed for each radial position (j=1,2,...N_y). The solution proceeds in the same manner as the cross-stream averaged solution, using the routines LUDCMP and LUBKSB [59]. The routine LUDCMP performs the LU-decomposition using Crout's algorithm and implicit pivoting [59] while LUBKSB performs the required forward and back substitutions to obtain the solution to the equation set.

Over the second half of first fractional step (substep 2), the ADI method requires that the transport equation becomes

$$Q_\alpha|^t_{i,j} - \underbrace{AQ_\alpha|^{t+\Delta t}_{i-1,j} - CQ_\alpha|^{t+\Delta t}_{i+1,j}}_{\text{Treat as known}} = \underbrace{DQ_\alpha|^{t+\Delta t}_{i,j-1} + BQ_\alpha|^{t+\Delta t}_{i,j} + EQ_\alpha|^{t+\Delta t}_{i,j+1}}_{\text{Solve in LU decomposition}}, \tag{7.18}$$

in which the terms in the axial direction that are calculated in substep 1 are now known and moved to the left hand side of the equation. Once again, the known terms on the left hand side of the equation are grouped into a single term.

$$Q^*_\alpha|^t_{i,j} = Q_\alpha|^t_{i,j} - AQ_\alpha|^{t+\Delta t}_{i-1,j} - CQ_\alpha|^{t+\Delta t}_{i+1,j}. \tag{7.19}$$

This equation set for the radial direction is solved in the same manner as substep 1, and can be represented by

$$\begin{bmatrix} 1 & 0 & 0 & 0 & \cdots & 0 & 0 & 0 \\ D_{i,2} & B_{i,2} & E_{i,2} & 0 & \cdots & 0 & 0 & 0 \\ 0 & D_{i,3} & B_{i,3} & E_{i,3} & \cdots & 0 & 0 & 0 \\ \vdots & & \vdots & & \ddots & \vdots & & \vdots \\ 0 & 0 & 0 & 0 & \cdots & D_{i,N_y-1} & B_{i,N_y-1} & E_{i,N_y-1} \\ 0 & 0 & 0 & 0 & \cdots & D_{i,N_y} & B_{i,N_y} & E_{i,N_y} \end{bmatrix} \times \begin{bmatrix} Q_\alpha|^{t+\Delta t}_{i,1} \\ Q_\alpha|^{t+\Delta t}_{i,2} \\ Q_\alpha|^{t+\Delta t}_{i,3} \\ \vdots \\ Q_\alpha|^{t+\Delta t}_{i,N_y-1} \\ Q_\alpha|^{t+\Delta t}_{i,N_y} \end{bmatrix} = \begin{bmatrix} Q_\alpha|^t_{i,1} \\ Q_\alpha|^t_{i,2} \\ Q_\alpha|^t_{i,3} \\ \vdots \\ Q_\alpha|^t_{i,N_y-1} \\ Q_\alpha|^t_{i,N_y} \end{bmatrix}$$

Once again, the routines LUDCMP and LUBKSB [59] are implemented to solve for the conditional species mass fractions. Due to time constraints, the impact of changing the axial grid spacing, Δx, and the timestep are not examined.

7.2.3 Mixture Fraction Space Terms

The stiff chemical source term and micromixing terms are solved in the second fractional step in the same manner as outlined in Section 5.8.2. The added radial dimension does not affect the procedure in this fractional step, as both terms being considered are dependant only on the mixture fraction space variable η. The stiff ODE solver, VODE [61], is called at each location in the 2D CMC grid, and solves the equation

$$\frac{\partial Q_\alpha}{\partial t} = \frac{1}{2}\langle\chi|\eta\rangle\frac{\partial^2 Q_\alpha}{\partial \eta^2} + \frac{\langle\dot{\omega}|\eta\rangle}{\langle\rho|\eta\rangle}, \tag{7.20}$$

over the interval [t,t+dt]. The values of Q_alpha from the previous fractional step are used as initial conditions.

7.3 Two-Dimensional Autoignition Results

In this section the results from the solution of two-dimensional CMC equations utilizing the AMC mixing model are presented and compared with the cross-stream averaged results. The ignition delays, along with the radial and axial ignition locations, are listed in Table 7.1. The ignition delays are plotted against the experimental data and cross-stream averaged results in Figure 7.1. The ignition locations are shown in Figure 7.2. The predicted ignition delays for all three air temperatures are in excellent agreement with the cross-stream averaged results. The largest difference is noted for $T_{air} = 1337$ K (corresponding to $1/T = 0.75$), in which the ignition delay from the two-dimensional solution is 7% lower than the cross-stream averaged result. These results indicate that the use of cross-stream averaging to simplify the solution of the CMC equations has little effect on the predictions of ignition delay.

Table 7.1: 2D CMC ignition results

Model	$t_d \quad (ms)$	$\chi_{ign} \quad (1/s)$	$x_{ign} \quad (mm)$	$r_{ign} \quad (mm)$	η_{ign}
1385 K	0.360	0.890	10	2.66	0.0110
1337 K	0.510	0.204	12.5	4.43	0.0138
1294 K	0.770	0.152	15.0	5.32	0.0138

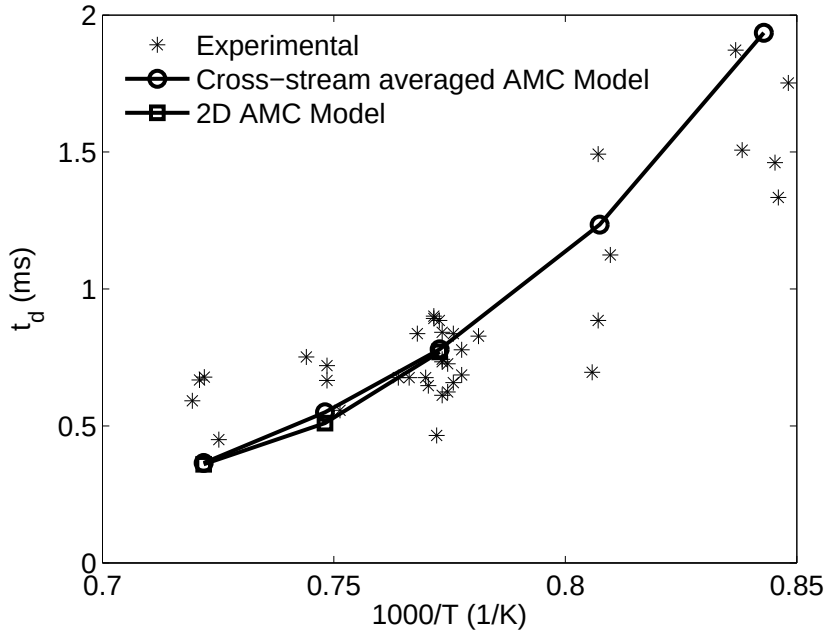

Figure 7.1: Comparison of 2D ignition delay with cross-stream averaged results.

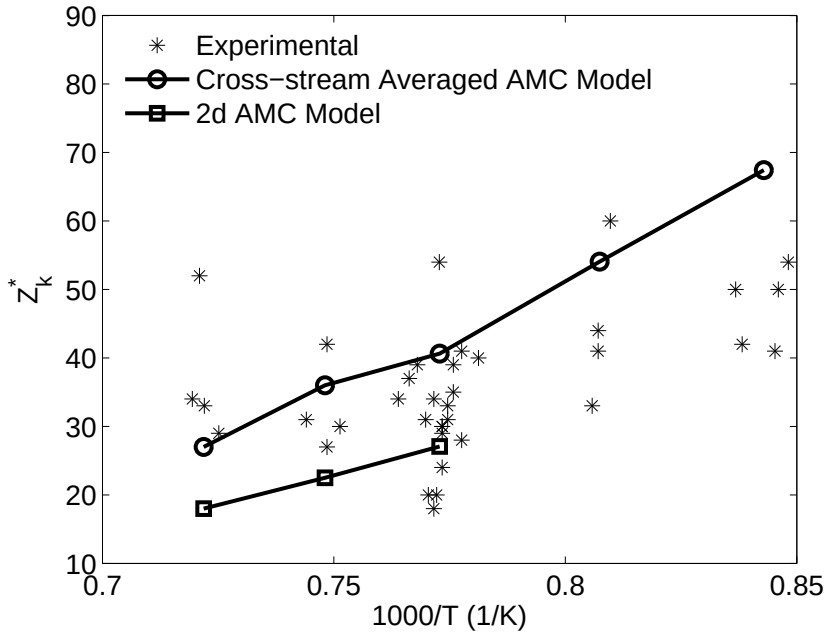

Figure 7.2: Comparison of 2D axial ignition location with cross-stream averaged results.

The axial ignition locations from the two-dimensional solution of the CMC equations are considerably closer to the injector, with a reduction of 50% in the cross-stream averaged values for all three air temperatures. Ignition in the 2D solution is predicted at lower values of the conditional scalar dissipation rate. The two-dimensional results underpredict the experimental data for the two highest temperatures, but falls within the considerable experimental scatter for $T_{air} = 1294$ K. This implies that the cross-stream averaging of the CMC equations could have an impact on the predicted axial location of ignition. However, the effect of axial grid spacing and timestep within the ADI method that is employed to solve the two-dimensional equations has not been explored, and could provide additional insight.

The ignition mixture fractions η_{ign} are all slightly leaner than their corresponding cross-stream averaged results. Ignition is predicted at $\eta = 0.011$ for $T_{air} = 1385$ K, compared to 0.0138 for the cross-stream averaged solution. $T_{air} = 1337$ K and 1294 K have ignition mixture fractions of 0.0138, rather than the cross-stream averaged results of 0.0165 and 0.0195 respectively. Similar to the cross-stream averaged results, ignition occurs at locations where the scalar dissipation rate is well below its critical value (which is around 25

s^{-1} [26] for the present conditions and chemistry).

7.3.1 Integrated two-dimensional temperature field

The two-dimensional predictions of ignition delay and location can be further compared with the cross-stream averaged results by estimating a two-dimensional unconditional temperature field, $T(x, r)$, based upon the PDF profiles and conditional temperature profiles that are obtained in the cross-stream averaged solution of the CMC equations. Unconditional temperature data in the axial and radial directions is obtained by integrating the product of the conditional temperature, Q_T at a given axial position, and the PDF, $\widetilde{P}(\eta)$, from $\eta = 0$ to 1.

$$\widetilde{T}(t, x, r) = \int_0^1 Q_T(t, x, \eta)\widetilde{P}(t, x, r, \eta)d\eta. \tag{7.21}$$

The values for Q_T are obtained at each axial location considered in the cross-stream averaged CMC solution, and output into data libraries. The values for $\widetilde{P}(\eta)$ are calculated at all grid points in the domain within the flow field solution. This allows PDF values over a range of radial positions to be used to calculate radial profiles of temperature at a specific axial position from a single value of Q_T. Using linear interpolation a 500 point grid is implemented in η-space for the profiles of Q_T and $\widetilde{P}(\eta)$, to reduce numerical error in the trapezoidal integration. The cross-stream averaged solution of the CMC equations utilizing the AMC model was performed for all five air temperatures, and output files of conditional temperature and PDF were generated five timesteps past the occurance of ignition to allow calculation of the 2D temperature field over a time interval longer than the cross-stream averaged ignition delays.

Two ignition criteria are investigated. In contrast to the findings of El Sayed [43], a rise in unconditional temperature of 75 K over the initial air temperature (based upon the ignition criterion of a rise in conditional temperature of 75 K used for the cross-stream averaged solution) resulted in ignition delays significantly longer than the resulting cross-stream averaged delays. The second criterion, a rise in temperature 1 K over the initial unconditional air temperature, yields results in much closer agreement to the cross-stream averaged predictions. This criterion is used for the autoignition results presented here for the integrated temperature field. The ignition delays and locations are presented in

Table 7.2. The ignition delays from the integrated temperature field are shown with the cross-stream averaged and two-dimensional results in Figure 7.3, and the ignition locations are compared in Figure 7.4. The radial ignition location is 37% higher than the two-dimensional prediction for $T_{air} = 1385$ K, but agreement is much better for the two lower air temperatures. For $T_{air} = 1337$ K the radial ignition locations are within 4%, and the values at $T_{air} = 1294$ K are within 11 %.

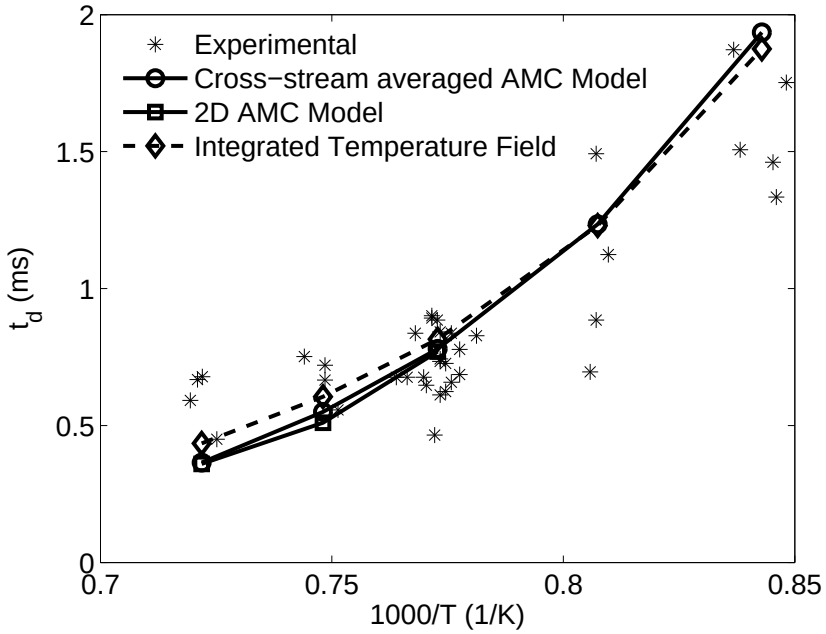

Figure 7.3: Comparison of ignition delay from integrated temperature field with cross-stream averaged and 2D results.

The resulting ignition delays are very similar to those obtained from both the cross-stream averaged and two-dimensional solution of the CMC equations. At higher air temperatures the ignition delay is longer relative to the previous results, while at the lowest air temperature the ignition delay is shorter. For $T_{air} = 1385$ K the ignition delay from the integrated temperature field is 19% longer than the cross-stream averaged prediction, while the ignition delay at $T_{air} = 1186$ K is 7% lower. These differences result in the ignition delays from the integrated temperature field corresponding closer to the experimental data. The axial ignition locations fall between the two-dimensional and the cross-stream

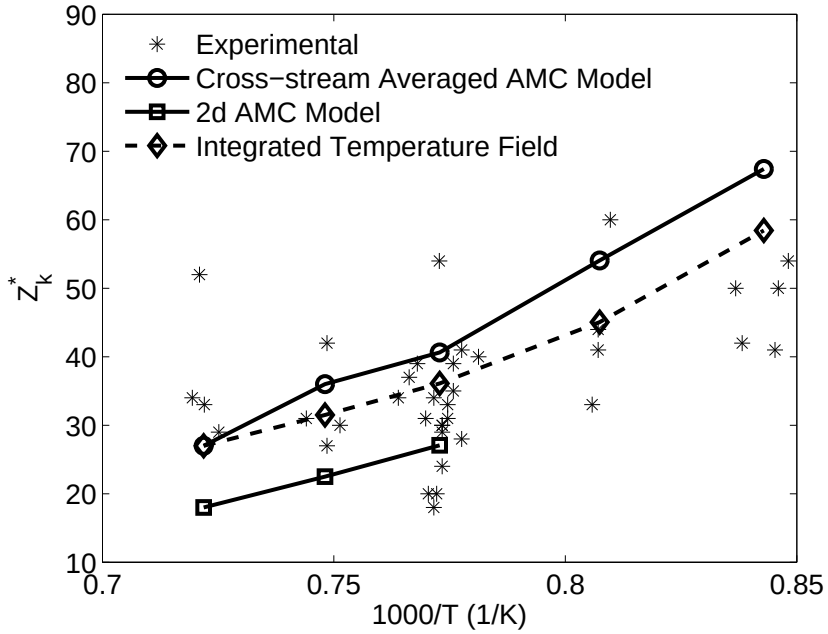

Figure 7.4: Comparison ignition location from integrated temperature field with cross-stream averaged and 2D results.

Table 7.2: CMC ignition results from integrated temperature field

Model	$t_d \quad (ms)$	$x_{ign} \quad (mm)$	$r_{ign} \quad (mm)$
1385 K	0.435	15.0	3.65
1337 K	0.605	17.5	4.26
1294 K	0.815	20.0	4.79
1238 K	1.230	25.0	5.91
1186 K	1.875	32.5	7.21

averaged results. The axial ignition location at $T_{air} = 1385$ is the same as the cross stream averaged results. With decreasing air temperature the ignition location from the integrated temperature field moves closer to the injector compared to the corresponding cross-stream averaged predictions. Comparison with the experimental data is marginal due to the high degree of scatter and small number of points. The decrease in ignition location at the lowest temperature relative to the cross-stream averaged prediction results in values that are in better agreement with the few points of experimental data. The ignition location for $T_{air} = 1385$ K, determined from the integrated temperature field, is presented in Figure 7.5. Ignition is predicted to occur on the lean side of the mixing layer, which is consistent with previous autoignition studies of methane [27, 28, 43, 44]. However, in contrast to the previous studies, ignition from the integrated temperature fields for all five air temperatures is found to occur in very lean regions of the flow, at mixture fraction values around 0.005. Ignition is expected to occur in lean regions slightly closer to the stoichiometric mixture fraction of 0.055. Further investigation in regard to the ignition location is needed to explain this discrepancy.

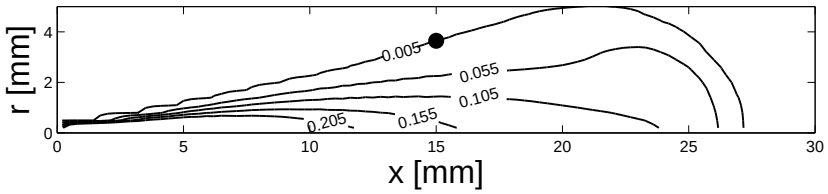

Figure 7.5: Integrated temperature field ignition location (black dot) for $T_{air} = 1385$ K.

7.4 Summary

The resulting ignition delays for the three highest air temperatures utilizing a two-dimensional solution of the CMC equations are within 7% of the cross-stream averaged results. This excellent agreement supports the use of cross-stream averaging to significantly simplify the solution of the CMC equations. However, the resulting ignition locations are closer to the injector than the corresponding cross-stream averaged predictions and ignition is predicted

at slightly leaner mixture fractions. As these two-dimensional results are preliminary, further investigation into the effect of axial grid spacing and timstep within the ADI method would be useful. Further analysis of the two-dimensional solution would provide greater insight into the impact of the shear flow approximation on the autoignition results.

Both the ignition delay and location from the integrated temperature field are in better agreement with the experimental data. The axial ignition locations are closer to the injector than the cross-stream averaged results for all but the highest air temperature, but are still further downstream than the predictions from the two-dimensional solution of the CMC equations. However, a different ignition criterion, based upon unconditional temperature rather than conditional temperature, was applied, and thus has an significant influence on the results.

Chapter 8

Conclusions

The present research investigated the impact of two modelling assumptions previously used by El Sayed [43] and El Sayed et al. [26, 44] in simulations of methane autoignition at engine relevant conditions using CMC. In this study the impact of a turbulent mixing model that is formulated based upon inhomogeneous turbulence on the predictions of autoignition was examined. Two forms of the inhomogeneous mixing model were implemented, one utilizing the linear conditional velocity model and the other making use of the gradient diffusion conditional velocity model. In this thesis the CMC equations were presented, and the unclosed terms and subsequent closures were discussed. The overall solution methodology was outlined. Using the frozen mixing assumption, the flow field calculations were decoupled from the CMC calculations. For this study this simplification was reasonable because density and temperature changes prior to autoignition are negligible. The flow field solution was performed in ANSYS CFX using the standard k-ε turbulence model. Data was exported from the flow field solution and was cross-stream averaged to create input files for the CMC calculations. Cross-stream averaging of the CMC equations based upon the shear flow approximation was discussed, and the impact of cross-stream averaging on the autoignition predictions was further investigated. The CMC equations were solved using the fractional step method, which allowed for the stiff chemical source term to be treated separately. The chemical source and micromixing terms were solved using the stiff ODE solver VODE [61], and the physical transport terms were solved using the LU-decomposition routines LUDCMP and LUBKSB [59]. The chemical kinetics package CHEMKIN II [63] and mechanism UBC Mech 1.0 [64] were employed. Differences between

the two formulations of the inhomogeneous turbulent mixing model were examined, and the autoignition predictions were compared with previous results using homogeneous mixing models [44] and with the experimental data of Wu [5].

8.1 Impact of Conditional Velocity Model

The behaviour of the linear and gradient diffusion conditional velocity models were examined and their impact on the predictions of the conditional scalar dissipation rate were assessed. The gradient diffusion conditional velocity model was shown to depart significantly from the linear relationship in mixture fraction space for low probability regions, diverging toward $\pm\infty$ at the lean and rich limits when the corresponding PDF values were near zero. Similar divergent behaviour for the gradient model, when used with the presumed β-PDF, was reported by Mortensen and de Bruyn Kops [24]. For regions that were roughly three to four standard deviations about the mean mixture fraction, the linear and gradient models yielded similar profiles. Cross-stream averaging of the conditional velocities produced very similar behaviour in the lean mixture region for both models, as the divergent behaviour of the gradient model at low probability lean values does not negatively impact the cross-stream averaged velocity. Below $\eta = 0.2$, corresponding to the range of mixture fraction values where chemical activity is highest, the models were in excellent agreement. Since only the cross-stream averaged axial conditional velocity appears in the convective term of the CMC equations, the effect of the conditional velocity model will be solely in its impact on the predictions of the conditional scalar dissipation rate from the inhomogeneous mixing model.

The diverging behaviour of the gradient conditional velocity model at low probability regions caused some unphysical behaviour in the profiles of $\langle\chi|\eta\rangle\tilde{P}(\eta)$. The Inhomogeneous-Linear model yielded profiles consistent with expectations, similar in shape to that of the PDF. The gradient version showed significant departures from the expected behaviour at the centreline, where a much larger peak than the linear version was noted and an unphysical plateau at very lean mixtures was observed. With increasing radial position the differences between the two versions of the inhomogeneous model decreased, and the profiles were similar in shape and magnitude near the edge of the mixing layer. The plateau region at small mixture fraction values for the Inhomogeneous-Gradient model was cor-

rected by setting the value of $\langle\chi|\eta\rangle\tilde{P}(\eta)$ to zero. When cross-stream averaged both models yielded profiles with plausible behaviour. The Inhomogeneous-Gradient model exhibited peak values at lower values of mixture fraction, and predicted higher conditional scalar dissipation rates in the region of interest, near the most reactive mixture. For lean mixtures the Inhomogeneous-Linear model produced values very similar to those obtained with the AMC model.

8.2 Consistency With Mean Scalar Dissipation Rate

To maintain consistency with the form of the mean scalar dissipation rate that was implemented in the mean mixture fraction variance transport equation, the profiles of $\langle\chi|\eta\rangle\tilde{P}(\eta)$ were integrated over mixture fraction space to yield unconditional values. Both models yielded unconditional expectations in poor agreement with the mean $\tilde{\chi}$ near the centreline, with better agreement noted near the edge of the mixing layer. The Inhomogeneous-Linear model was shown to be not fully consistent with the variance equation by Devaud et al. [21], thus some discrepancy was expected. However, the magnitude of the difference was greater than anticipated. One major advantage of the Inhomogeneous-Gradient formulation was that it was supposed to be consistent with the first and second moment of the mixture fraction [38]. The fact that the value of $\tilde{\chi}$ used in the mixture fraction variance equation is not recovered from integrating $\langle\chi|\eta\rangle\tilde{P}(\eta)$ shows that the diverging behaviour of the gradient conditional velocity model in low probability areas had a significant effect on the overall predictions of the mixing model.

8.3 Autoignition Results

The Inhomogeneous-Linear model yielded ignition delays and locations very similar to those obtained with AMC and Girimaji's model for all air temperatures. In contrast, the Inhomogeneous-Gradient model produced noticeably higher ignition delays and predicted ignition to occur further downstream from the injector. For all models ignition was found to occur when scalar dissipation rates were considerably below the critical value [26] and

at their steady state value. Ignition for the gradient version was found to occur at slightly richer mixtures when compared with the Inhomogeneous-Linear model and homogeneous models. The larger ignition delays of the Inhomogeneous-Gradient model are directly influenced by the numerical issues observed in the gradient conditional velocity model used in conjunction with the β-PDF.

8.4 Cross-Stream Averaging

The preliminary solution of the CMC equations using the AMC mixing model in two dimensions yielded ignition delays that were in excellent agreement with the corresponding cross-stream averaged results. The corresponding ignition locations were found to be significantly upstream of the cross-stream averaged predictions. A two-dimensional temperature field was calculated through integrating the product of the PDF and the conditional temperature results from the cross-stream averaged CMC solution. Judging ignition to occur when the local temperature exceeded the initial air temperature, the resulting ignition delays were similar to those from the cross-stream and two-dimensional results. The overprediction of ignition delay at low air temperatures and underprediction at high air temperatures was reduced, resulting in better agreement with the experimental data. The ignition locations from the integrated temperature field were further upstream than the cross-stream averaged results for most air temperatures, but downstream of the two-dimensional axial ignition locations. Based on the present findings, the shear flow approximation appears to be applicable to the autoignition conditions examined in this thesis. Further investigation of the two-dimensional solution and ignition criteria would be useful to assess the sensitivity of the axial ignition location in these two-dimensional cases.

8.5 Recommendations

Other parameters within the autoignition problem need to be examined to assess their impact on the autoignition predictions. LES, while more computationally expensive, would provide a detailed prediction of transient turbulent structures in the mixing field due to its

consideration of instantaneous quantities, rather than the averaged quantities considered in RANS models. Based upon the scatter observed in the experimental data, LES may be better suited to represent the unsteady turbulent processes and provide predictions for a number of realizations of the flow. In the context of CMC, higher order closures could be applied, to account for fluctuations about the conditional averages. The performance of the gradient diffusion conditional velocity model, and its impact on the predicitons of scalar dissipation rate using the Inhomogeneous-Gradient mixing model, with alternative forms of the PDF would provide valuable insight. In future work, the role of the conditional scalar dissipation rate is likely to remain significant even in higher order closures or multiple conditioning methods.

Bibliography

[1] U.S. Department of Energy, Energy Information Administration. 2008 Annual Energy Review `http://www.eia.doe.gov/emeu/aer/`, 2009.

[2] Natural Resources Canada. CanmetENERGY - Transportation `http://canmetenergy-canmetenergie.nrcan-rncan.gc.ca/eng/transportation`, 2009.

[3] Environment Canada. Canada's 2007 Greenhouse Gas Inventory `http://www.ec.gc.ca/pdb/ghg/inventory_report/2007/som-sum_eng.cfm`, 2010.

[4] S.R. Turns. *An introduction to combustion*. McGraw-Hill, Boston, USA, second edition, 2000.

[5] N. Wu. *Autoignition and emission characteristics of gaseous fuel direct-injection compression-ignition combustion*. PhD thesis, University of British Columbia, Vancouver, Canada, 2004.

[6] S.B. Pope. *Turbulent Flows*. Cambridge University Press, Cambridge, U.K., first edition, 2000.

[7] H.K. Versteeg and W. Malalasekera. *An Introduction to Computational Fluid Dynamics: The Finite Volume Method*. Pearson Education, Essex, 2007.

[8] B.E. Launder and B.I. Sharma. Application of the energy-dissipation model of turbulence to the calculation of flow near a spinning disc. *Lett. Heat Mass Transf.*, 1:131–138, 1974.

[9] D.C. Wilcox. Reassessment of the scale-determining equation for advanced turbulence models. *AIAA Journal*, 26(11):1299–1310, 1988.

[10] ANSYS, Inc. ANSYS CFX 11.0, `http://www.ansys.com/products/cfx.asp`, 2008.

[11] N. Peters. Laminar diffusion flamelet models in non-premixed turbulent combustion. *Prog. energy Combust. Sci*, 10(3):319–339, 1984.

[12] A.Yu. Klimenko and R.W. Bilger. Conditional moment closure for turbulent combustion. *Prog. Energy Combust. Sci.*, 25(6):595–687, 1999.

[13] P.A. Libby and F.A. Williams. *Turbulent Reacting Flows*. Springer-Verlag, Berlin, 1980.

[14] D.B. Spalding. Mixing and chemical reaction in steady confined turbulent flames. *Symposium (International) on Combustion*, 13(1):649 – 657, 1971.

[15] S.B. Pope. Lagrangian PDF methods for turbulent flows. *Annu. Rev. Fluid Mech.*, 26:23–63, 1994.

[16] S.B. Pope. PDF methods for turbulent reacting flows. *Prog. Energy Combust. Sci.*, 11:119–192, 1985.

[17] A.Yu. Klimenko. Multicomponent diffusion of various admixtures in turbulent flow. *Fluid Dyn.*, 25(3):327–334, 1990.

[18] R.W. Bilger. Conditional moment closure for turbulent reacting flow. *Phys. Fluids A*, 5(2):436–444, 1993.

[19] V. R. Kuznetsov and V. A. Sabel'nikov. *Turbulence and Combustion*. Hemisphere, New York, 1990.

[20] S.B. Pope. PDF methods for turbulent reactive flows. *Prog. Energy Combust. Sci.*, 11(2):119–192, 1985.

[21] C.B. Devaud, R.W. Bilger, and T. Liu. A new method of modeling the conditional scalar dissipation rate. *Phys. Fluids*, 16(6):2004–2011, 2004.

[22] N. Swaminathan and R.W. Bilger. Analyses of conditional moment closure for turbulent premixed flames. *Combust. Theory Modell.*, 5(2):241–260, 2001.

[23] S.M. de Bruyn Kops and M. Mortensen. Conditional mixing statistics in a self-similar scalar mixing layer. *Phys. Fluids*, 17(9):095107, 2005.

[24] M. Mortensen and S.M. de Bruyn Kops. Conditional velocity statistics in the double scalar mixing layer - a mapping closure approach. *Combust. Theory Modell.*, 12(5):929–941, 2008.

[25] M. Mortensen and B. Andersson. Presumed mapping functions of Eulerian modelling of turbulent mixing. *Flow, Turbul., Combust.*, 76:199–219, 2006.

[26] A. El Sayed and C.B. Devaud. Conditional moment closure (CMC) applied to autoignition of high pressure methane jets in a shock tube. *Combust. Theory Modell.*, 12(5):943–972, 2008.

[27] S.H. Kim, K.Y. Huh, and R.A. Fraser. Modeling autoignition of a turbulent methane jet by the Conditional Moment Closure model. *Proc. Combust. Inst.*, 28:185–191, 2000.

[28] W.T. Kim and K.Y. Huh. Numerical simulation of spray autoignition by the first order Conditional Moment Closure model. *Proc. Combust. Inst.*, 29:569–576, 2002.

[29] Y.M. Wright, G. De Paola, K. Boulouchos, and E. Mastorakos. Simulations of spray autoignition and flame establishment with two-dimensional CMC. *Combust. Flame*, 143(4):402–419, 2005.

[30] C.N. Markides, G. De Paola, and E. Mastorakos. Measurements and simulations of mixing and autoignition of an n-heptane plume in a turbulent flow of heated air. *Exp. Therm. Fluid Sci.*, 31(5):393–401, 2007.

[31] G. De Paola, I.S. Kim, and E. Mastorakos. Second-order conditional moment closure simulations of autoignition of an n-heptane plume in a turbulent coflow of heated air. *Flow, Turbul. and Combust.*, 82(4):455–475, 2009.

[32] G. De Paola, E. Mastorakos, Y.M. Wright, and K. Boulouchos. Diesel engine simulations with multi-dimensional conditional moment closure. *Combust. Sc. Tech.*, 180(5):883–899, 2008.

[33] A. Triantafyllidis, E. Mastorakos, and R.L.G.M. Eggels. Large Eddy Simulations of forced ignition of a non-premixed bluff-body methane flame with conditional moment closure. *Combust. Flame*, 156(12):2328–2345, 2009.

[34] J.W. Rogerson, J.H. Kent, and R.W. Bilger. Conditional moment closure in a bagasse-fired boiler. *Proc. Combust. Inst.*, 31:2805–2811, 2007.

[35] S.S. Girimaji. Assumed beta-pdf model for turbulent mixing : validation and extension to multiple scalar mixing. *Combust. Sci. Technol*, 78(4-6):177–196, 1991.

[36] N. Swaminathan and S. Mahalingam. Assessment of conditional moment closure for single and multistep chemistry. *Combust. Sci. Technol.*, 112(1):301–326, 1996.

[37] M. Mortensen and B. Andersson. Presumed mapping functions for eulerian modelling of turbulent mixing. *Flow, Turb. and Comb.*, 76(2):199–219, 2006.

[38] M. Mortensen. Consistent modeling of scalar mixing for presumed, multiple parameter probability density functions. *Phys. Fluids*, 17(018106), 2005.

[39] S.S. Girimaji. On the modeling of scalar diffusion in isotropic turbulence. *Phys. Fluids A*, 4(11):2529–2537, 1992.

[40] E. O'Brien and T.L. Jiang. The conditional dissipation rate of an initially binary scalar in homogeneous turbulence. *Phys. Fluids A*, 3(12):3121–3123, 1991.

[41] A.Yu. Klimenko. Note on the conditional moment closure in turbulent shear flows. *Phys. Fluids*, 7(2):446–448, 1995.

[42] R.M. Woolley, M. Fairweather, and Yunardi. Conditional moment closure modelling of soot formation in turbulent, non-premixed methane and propane flames. *Fuel*, 88(3):393–407, 2009.

[43] A. El Sayed. Ignition delay of non-premixed methane-air mixtures using Conditional Moment Closure (CMC). Master's thesis, University of Waterloo, Waterloo, Ontario, Canada, September 2007.

[44] A. El Sayed, A. Milford, and C.B. Devaud. Modelling of autoignition for methane-based fuel blends using Conditional Moment Closure. *Proc. Combust. Inst.*, 32(1):1621 – 1628, 2009.

[45] W.K. Bushe. *Conditional Moment Closure methods for autoignition problems.* PhD thesis, University of Cambridge, Cambridge, UK, 1995.

[46] W.K. Bushe and H. Steiner. Conditional moment closure for large eddy simulation of nonpremixed turbulent reacting flows. *Phys. Fluids*, 11(7):1896–1906, 1999.

[47] J. Huang and W.K. Bushe. Simulation of an igniting methane jet using Conditional Source-term Estimation with a Trajectory Generated Low-Dimensional Manifold. *Combust. Theory Modell.*, 11(6):977–1008, 2007.

[48] R.W. Grout, W.K. Bushe, and C. Blair. Predicting the ignition delay of turbulent methane jets using Conditional Source-term Estimation. *Combust. Theory Modell.*, 11(6):1009–1028, 2007.

[49] R.W. Bilger. Some aspects of scalar dissipation. *Flow, Turbul. Combust.*, 72:93–114, 2004.

[50] J. Janicka and N. Peters. Prediction of turbulent jet diffusion flame lift-off using a pdf transport equation. *Proc. Combust. Inst.*, 19:367–374, 1982.

[51] S.B. Pope. Consistent modelling of scalar in turbulent flows. *Phys. Fluids*, 26:404–408, 1983.

[52] W.P. Jones and P. Musonge. Closure of the Reynolds stress and scalar flux equations. *Phys. Fluids*, 31:3589–3604, 1988.

[53] M.J. Cleary and J.H. Kent. Modelling of species in hood fires by conditional moment closure. *Combust. Flame*, 143:357–368, 2005.

[54] S. Sreedhara, Y. Lee, Kang Y. Huh, and D.H. Ahn. Comparison of submodels for conditional velocity and scalar dissipation in CMC simulation of piloted jet and bluff-body flames. *Combust. Flame*, 152:282–286, 2007.

[55] F. Gao. An analytical solution for the scalar probability density function in homogeneous turbulence. *Phys. Fluids A*, 3(4):511–513, 1991.

[56] S.B. Pope. An explanation of the turbulent round-jet/plane-jet anomaly. *AIAA Journal*, 16:279–281, 1978.

[57] P.G. Hill and P. Ouellette. Transient turbulent gaseous fuel jets for diesel engine. *J. Fluids Eng.*, 121(1):93–101, 1999.

[58] R. Piessens, E. de Doncker-Kapenga, and C.W. Ueberhuber. *Quadpack: A Subroutine Package for Automatic Integration*. Springer (Springer Series in Computational Mathematics), Berlin, 1983.

[59] W.H. Press, B.P. Flannery, S.A. Teukolsky, and W.T. Vetterling. *Numerical Recipes: the art of scientific computing (FORTRAN version)*. Cambridge University Press, 1989.

[60] R.O. Fox. *Computational models for turbulent reacting flows*. Cambridge University Press, 2003.

[61] P.N. Brown, G.D. Byrne, and A.C. Hindmarsh. VODE, a variable-coefficient ODE solver. *SIAM J. on Sci. and Stat. Computing*, 10:1038–1051, 1989.

[62] G.D. Byrne and A.C. Hindmarsh. A polyalgorithm for the numerical solution of ordinary differential equations. *ACM Trans. on Math. Software*, 1(1):71–96, 1975.

[63] R.J. Kee, F.M. Rupley, and J.A. Miller. CHEMKIN-II: A fortran chemical kinetics package for the analysis of gas-phase chemical kinetics. *Sandia National Labs*, Technical Report, SAND-89-8009, 1989.

[64] J. Huang, P.G. Hill, W.K. Bushe, and S.R. Munshi. Shock-tube study of methane ignition under engine-relevant conditions: experiments and modeling. *Combust. Flame*, 136(1-2):25–42, 2004.

[65] E.L. Petersen, D.F. Davidson, and R.K. Hanson. Kinetics modeling of shock-induced ignition in low-dilution CH4/O2 mixtures at high pressures and intermediate temperatures. *Combust. Flame*, 117(1-2):272 – 290, 1999.

[66] B.L. Sawford. Conditional scalar mixing statistics in homogeneous isotropic turbulence. *New J. Physics*, 6(55):1–30, 2004.

[67] G. Brethouwer and F.T.M Nieuwstadt. DNS of mixing and reaction of two species in a turbulent channel flow: a validation of the conditional moment closure. *Flow, Turbul. and Combust.*, 66:209–239, 2001.

[68] E. Mastorakos. Ignition of turbulent non-premixed flames. *Prog. Energy Combust. Sci.*, 2009.

[69] D.W. Peaceman and H.H Rachford Jr. The numerical solution of parabolic and elliptic differential equations. *J. Soc. Indust. Appl. Math*, 3(1):28–41, 1955.